

Indications for very high metallicity and absence of methane in the eccentric exo-Saturn WASP-117b

Ludmila Carone¹, Paul Mollière,¹ Yifan Zhou,² Jeroen Bouwman,¹ Fei Yan,³ Robin Baeyens,⁴ Dániel Apai,⁵ Nestor Espinoza,⁶ Benjamin V. Rackham,^{7,8} Andrés Jordán,^{9,10} Daniel Angerhausen,^{11,12,13} Leen Decin,⁴ Monika Lendl,¹⁴ Olivia Venot,¹⁵ and Thomas Henning¹

¹ Max-Planck-Institut für Astronomie, Königstuhl 17, 69117 Heidelberg, Germany
e-mail: carone@mpia.de

² Department of Astronomy/McDonald Observatory, The University of Texas, 2515 Speedway, Austin, TX, 78712, USA

³ Institut für Astrophysik, Georg-August-Universität, Friedrich-Hund-Platz 1, 37077 Göttingen, Germany

⁴ Instituut voor Sterrenkunde, KU Leuven, Celestijnenlaan 200D, B-3001 Leuven, Belgium

⁵ Steward Observatory, The University of Arizona, 933 N. Cherry Avenue, Tucson, AZ 85721, USA, and Lunar and Planetary Laboratory, The University of Arizona, 1629 E. Univ. Blvd., Tucson, AZ 85721, USA

⁶ Space Telescope Science Institute, 3700 San Martin Drive, Baltimore, MD, USA

⁷ Department of Earth, Atmospheric and Planetary Sciences, and Kavli Institute for Astrophysics and Space Research, Massachusetts Institute of Technology, Cambridge, MA 02139, USA

⁸ 51 Pegasi b Fellow

⁹ Facultad de Ingeniería y Ciencias, Universidad Adolfo Ibáñez, Av. Diagonal las Torres 2640, Peñalolén, Santiago, Chile

¹⁰ Millennium Institute for Astrophysics, Chile

¹¹ ETH Zürich, Inst. f. Teilchen- und Astrophysik, Zürich, Switzerland

¹² CSH Fellow, Center for Space and Habitability, University of Bern, Switzerland

¹³ Blue Marble Space Institute of Science, Seattle, United States

¹⁴ Observatoire de Genève, chemin des maillettes 51, 1290 Sauverny, Switzerland

¹⁵ Laboratoire Interuniversitaire des Systèmes Atmosphériques (LISA), UMR CNRS 7583, Université Paris-Est-Créteil, Université de Paris, Institut Pierre Simon Laplace, Créteil, France

Received TBD; accepted TBD

ABSTRACT

Aims. We investigate the atmospheric composition of the long period ($P_{\text{orb}} = 10$ days), eccentric exo-Saturn WASP-117b. WASP-117b could be in atmospheric temperature and chemistry similar to WASP-107b. In mass and radius WASP-117b is similar to WASP-39b, which allows a comparative study of these planets.

Methods. We analyze a near-infrared transmission spectrum of WASP-117b taken with Hubble Space Telescope/WFC3 G141, which was reduced with two independent pipelines. High resolution measurements were taken with VLT/ESPRESSO in the optical.

Results. We report the robust (3σ) detection of a water spectral feature. Using a 1D atmosphere model with isothermal temperature, uniform cloud deck and equilibrium chemistry, the Bayesian evidence of a retrieval analysis of the transmission spectrum indicates a preference for a high atmospheric metallicity $[\text{Fe}/\text{H}] = 2.58^{+0.26}_{-0.37}$ and clear skies. The data are also consistent with a lower-metallicity composition $[\text{Fe}/\text{H}] < 1.75$ and a cloud deck between $10^{-2.2} - 10^{-5.1}$ bar, but with weaker Bayesian preference. We retrieve a low CH_4 abundance of $< 10^{-4}$ volume fraction within 1σ and $< 2 \cdot 10^{-1}$ volume fraction within 3σ . We cannot constrain the equilibrium temperature between theoretically imposed limits of 700 and 1000 K. Further observations are needed to confirm quenching of CH_4 with $K_{zz} \geq 10^8$ cm^2/s . We report indications of Na and K in the VLT/ESPRESSO high resolution spectrum with substantial Bayesian evidence in combination with HST data.

Key words. Exoplanet – Observations – Hot Jupiters

1. Introduction

The past years have revealed a large diversity in the atmospheres of transiting extrasolar gas planets colder than 1000 K and smaller than Jupiter as well as a lack in methane in their atmospheres (e.g. Kreidberg 2015; Kreidberg et al. 2018; Wakeford et al. 2017, 2018; Benneke et al. 2019; Chachan et al. 2019). Whereas the atmospheric chemistry of hot Jupiters can be explained mainly with equilibrium chemistry, disequilibrium chemistry is expected to become more important for these cooler planets via vertical quenching, which results in an underabundance of CH_4 compared to predictions from equilibrium

chemistry (Crossfield 2015). In principle, CH_4 is readily detectable along-side H_2O in the near to mid-infrared.

While the quenching of CH_4 has been confirmed first in brown dwarfs and later in directly imaged exoplanets (Barman et al. 2011b,a; Moses et al. 2016; Miles et al. 2018; Janson et al. 2013), observing disequilibrium chemistry in transiting, tidally locked extrasolar gas planets has been more challenging. Quantifying CH_4 quenching reliably in transiting exoplanets to compare these disequilibrium chemistry processes to those occurring in brown dwarfs and directly imaged planets will be very illuminating to explore dynamical differences in different substellar atmospheres.

Disequilibrium chemistry depends on vertical atmospheric mixing (K_{zz}), which provides a link between the observable atmosphere and deeper layers (see e.g. Agúndez et al. 2014). Dynamical processes are further expected to be very different in tidally locked exoplanets compared to brown dwarfs just due to the different rotation and irradiation regime (Showman et al. 2014, 2019). For example, tidal locking slows down the rotation periods of transiting exoplanets to a few days, which is very slow in comparison to e.g. brown dwarfs with rotation periods less than 1 day (see e.g. Apai et al. 2017). Disequilibrium chemistry processes across a whole range of substellar atmospheres could thus shed light on deep atmospheric processes and on to why the detection of methane has been proven to be very difficult so far in transiting exoplanets.

To this date, both methane and water have only been reliably detected for one mature extrasolar gas planet: at the day side of the warm (600–850 K) Jupiter HD 102195b (Guilluy et al. 2019). For HAT-P-11b, the presence of methane is inferred with 1D atmosphere models for retrieval by Chachan et al. (2019), where the authors find that the observed steep rise in transit depth for wavelengths $\geq 1.5\mu\text{m}$ in their HST/WFC3 G141 data is not present when they simulate the spectrum after removing CH_4 opacities from the model. The authors could, however, not constrain CH_4 abundances further (Chachan et al. 2019). For the warm Super-Neptune WASP-107b (Kreidberg et al. 2018), methane quenching is suggested due to the absence of methane (no discernible opacity source that would translate to an increase in transit depth for $\lambda \geq 1.5\mu\text{m}$ in their HST/WFC3 G141 data), while water could be clearly detected. Benneke et al. (2019) also report for the mini-Neptune GJ 3470b methane depletion compared to disequilibrium chemistry models.

Many of the transiting exoplanets, for which disequilibrium chemistry may play a role, were also found to be less massive than Jupiter, ranging from mini-Neptune to Saturn-mass. These objects show a spread in metallicity that ranges from very low, $\leq 4\times$ solar, for the Neptune HAT-P-11b (Chachan et al. 2019) to very high values, $> 100\times$ metallicity, for the exo-Saturn WASP-39b (Wakeford et al. 2018).

In this paper, the transiting exo-Saturn WASP-117b joins the rank of super-Neptune-mass exoplanets with atmospheric composition constraints. WASP-117b is in mass ($0.277M_{Jup}$) and radius ($1.021R_{Jup}$) close to WASP-39b, which was found to be metal-rich (Wakeford et al. 2018). In temperature it could be 900 K or colder and thus similar in atmospheric chemistry to WASP-107b (Kreidberg et al. 2018). Therefore, this planet will aid a comparative analysis of methane content and metallicity from the Neptune to Saturn-mass range.

Furthermore, WASP-117b orbits its quiet F-type main sequence star on an eccentric orbit ($e = 0.3$) with a relatively large orbital period of ≈ 10 days (Lendl et al. 2014; Mallonn et al. 2019). Using the same formalism as Lendl et al. (2014)¹ to calculate atmospheric temperatures during one orbit, the planet would then reside on its eccentric orbit for several days in the hot ($T > 1000$ K) temperature regime, characterized by CO as the main carbon-bearing species at $p = 1$ bar for solar metallicity. The planet would also reside several days in the warm ($T < 1000$ K) regime, for which CH_4 becomes dominant in the observable atmosphere, and for which, depending on the strength of vertical mixing (K_{zz}) and atmospheric metallicity, disequilibrium

¹ Lendl et al. (2014) report equilibrium temperatures of 900 K and 1200 K during apoastron and periastron, respectively, assuming an albedo of $\alpha = 0$ and efficient, uniform redistribution of absorbed stellar energy over the whole planet.

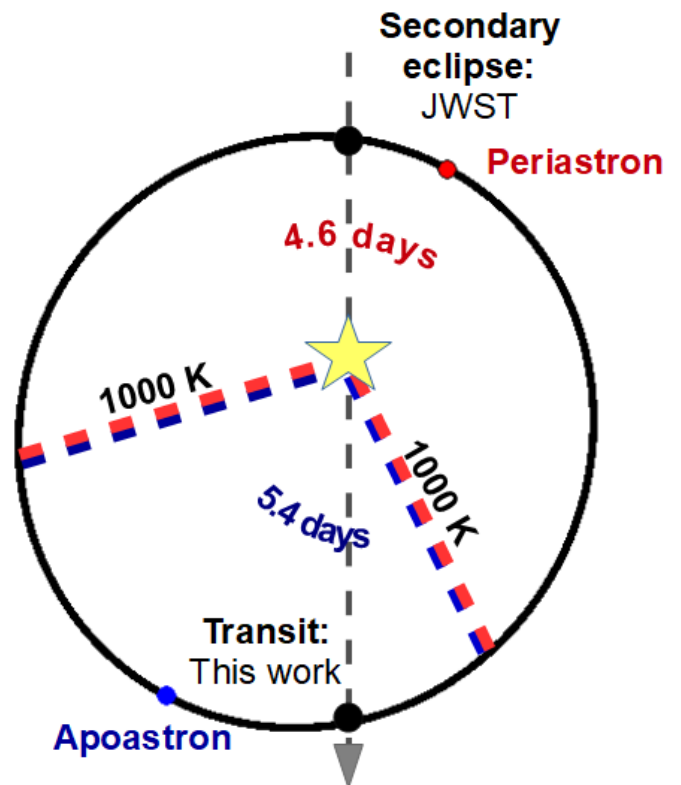


Fig. 1. The orbit orientation of WASP-117b and the expected equilibrium temperature, assuming albedo $\alpha = 0$ and to first order instant adjustment of atmospheric temperature to changes of incoming stellar flux as used in Lendl et al. (2014). Temperatures around 1000 K for solar metallicity denote the transition in equilibrium chemistry between CO (for the hot regime $T_{eq} \geq 1000$ K) and CH_4 (for the warm $T_{eq} \leq 1000$ K) (Crossfield 2015). In the latter case, however, formation of CH_4 is expected to be quenched due to disequilibrium chemistry. The planet is expected to remain 4.6 days in the hot regime and 5.4 days in the colder regime, respectively.

chemistry of methane potentially becomes observable (Figure 1). This is a different situation than compared to WASP-107b and WASP-39b that reside on tighter circular orbits all the time in the same temperature and thus chemistry regime.

The atmospheric properties of WASP-117b will thus shed further light on the diversity in basic atmospheric properties of transiting Super-Neptunes like atmospheric metallicity and CH_4 quenching at pressures deeper than 0.1 bar that can lead to depletion by several orders of magnitude compared to equilibrium chemistry for atmospheric temperatures colder than 1000 K. In addition, due to the relatively long eccentric orbit, this exo-Saturn will also allow us to understand how exoplanets on wider non-circular orbits that are subjected to varying irradiation and atmospheric erosion differ from exoplanets on tighter, circular orbits.

Last but not least, we will show that it is possible and worthwhile to characterize exo-Saturns on orbital periods of 10 days with single-epoch observations from space. Thus, our WASP-117b observations are prototype observations for other transiting exoplanets with orbital periods of 10 days and longer like K2-287 b (Jordán et al. 2019) and similar objects that were discovered after WASP-117b (Brahm et al. 2018; Jordán et al. 2020; Rodriguez et al. 2019).

We report here the first observations to characterize the atmosphere of the exo-Saturn WASP-117b (Section 2) in the near-

infrared with HST/WFC3 (Section 2.1) and in the optical with VLT/ESPRESSO (Section 2.2), respectively. We investigate the significance of the water detection with HST/WFC3 and Na and K with VLT/ESPRESSO in Section 3.1. We perform atmospheric retrieval with an atmospheric model (Section 3.2) mainly on the HST/WFC3 data to constrain basic properties of the atmosphere of the exo-Saturn WASP-117b (Sections 3.3 and 3.4). We then present improved stellar rotation and spin-orbit alignment parameters for WASP-117b via the Rossiter-McLaughlin effect measured with VLT/ESPRESSO (Section 3.5).

We also compared our data with broadband transit observations obtained by the Transiting Exoplanet Survey Satellite (TESS) in the optical (Section 3.6) and discussed influence of stellar activity to explain the discrepancy between TESS transit depth and our WFC3/NIR transmission spectrum, which were obtained at different times (Section 3.6.1). To provide better context for the low CH_4 abundances that we find, we calculated a small set of representative chemical models for different temperatures and metallicities (Section 4). To guide future observations to further characterize the system we also generated synthetic spectra based on our retrieved atmospheric models for wavelength ranges covered by HST/WFC3/UVIS and JWST (Section 5). We investigated the benefit of additional measurements to constrain the presence of a haze layer and to distinguish between high ($[\text{Fe}/\text{H}] > 2.2$) and low ($[\text{Fe}/\text{H}] < 1.75$) metallicity models. We discuss the atmospheric properties of WASP-117b and how they compare to other Super-Neptunes like WASP-39b and WASP-107b in Section 6. We provide a summary of our findings in Section 7 and outline steps for future observations of the eccentric exo-Saturn WASP-117b in Section 8.

2. Observations

We report here a near-infrared transmission spectrum measured with HST (Program GO 15301, PI: L. Carone) and a high resolution optical spectrum measured with VLT/ESPRESSO (PI: F. Yan). In the following, both set of observations and data reduction are described. For the HST/WFC3 raw data, we employed two completely independent data reduction pipelines for a robust retrieval of the atmospheric signal.

The relatively long transit duration of 6 hours required a long and stable observation by both HST and VLT/ESPRESSO, which were successfully carried out with both instruments.

2.1. HST observation and data reduction

We observed one transit of WASP-117 b with HST’s Wide Field Camera 3 (WFC3) instrument on UT 20-21 September 2019. The transit observation consists of eleven consecutive HST orbits. This HST observation benefited from re-observations of the WASP-117b transit in July 2017 with broad band photometry using two small telescopes. One in Chile, the Chilean-Hungarian Automated Telescope 0.7m (CHAT, PI: Jordán) and one in South Africa (1m, Los Cumbres Observatory). The combined observations allowed us to improve the uncertainties in mid-transit time from 2 hours (based on Lendl et al. 2014) to 2 minutes (Mallonn et al. 2019).

For the HST measurement, at the start of each orbit, an image of the target with the F126N filter, using NSAMP=3, rapid readout mode was taken. This image was used to anchor the wavelength calibration for each orbit. Otherwise, we obtained time series spectra with the G141 grism, which covers the wavelength range 1.1–1.7 μm . We used the NSAMP=15, SPARS 10 readout

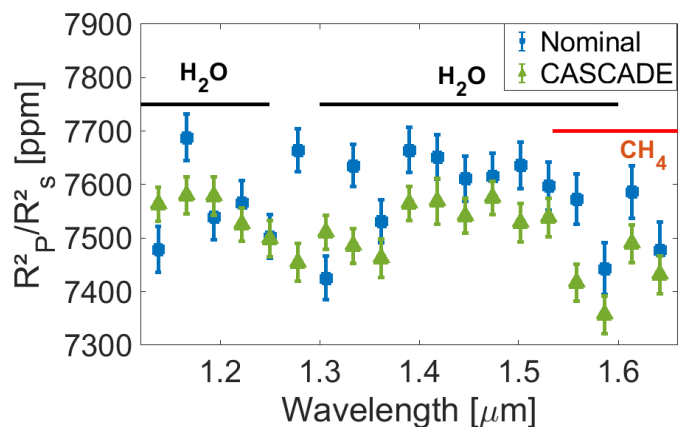


Fig. 2. Final HST/WFC3 transmission spectra from the nominal (blue) and CASCADE (green) pipeline, covering a wavelength range of 1.125 - 1.65 μm . Average transit depth is 7573 ± 43 ppm and 7553 ± 39 ppm, respectively. Black and red lines indicate, respectively, the positions of the H_2O and CH_4 absorption bands in the observed spectral range.

mode for these, in spatial scanning mode with a scan rate of 0.12 arcseconds/sec and scan direction “round trip”.

For raw data reduction, we employed two separate and completely independent pipelines to ensure that the derived atmospheric spectra are robust. We call the two pipelines henceforth nominal pipeline and CASCADE pipeline; their respective data reduction procedures are described in Appendix A.

2.1.1. Final transmission spectra

After data reduction, as described in Sections A.1 and A.2, we derived two transmission spectra (Figure 2). We excluded points outside of the wavelength range 1.125 - 1.65 μm because the instrument transmission has steeper gradients in those regions compared to the centre of the spectrum. Jittering in the wavelength direction together with the strong variation in transmission profile change can introduce large systematic errors. Since a strong methane absorption feature covered by the WFC3/G141 grism is centered at 1.62 μm , where H_2O has no absorption, we can still make judgements about the presence or absence of methane based on a spectrum covering 1.125 - 1.65 μm . This wavelength range was used for our further analysis.

The WASP-117b HST/WFC3 data indicate the presence of a muted water absorption spectrum with a slight drop in transit depth between 1.4 and 1.55 μm , which indicates H_2O absorption centered at 1.45 μm . There is potentially a second peak towards the shorter wavelengths at the edge of the spectral window. There is no strong CH_4 absorption feature towards the longest wavelengths in the observed spectral window. The feature is present in both spectra (nominal and CASCADE), using two independent reduction pipelines for the same data set.

However, it also appears that the nominal spectrum is slightly shifted towards deeper transit depths than the CASCADE spectrum. Further, some data points appear to deviate more than 3σ from each other. We attribute these deviations to differences at the raw light curve extraction as described in the next subsection.

2.1.2. Comparison of employed data pipelines

We find that the transmission spectra from the two pipelines demonstrate discrepancies (Figure 2). First, there is disagree-

ment in the average transit depth. Calculating the standard error of the mean σ/\sqrt{n} (SEM) gives values of $\text{SEM}_{\text{nominal}} = 18.2$ ppm for the nominal and $\text{SEM}_{\text{CASCADE}} = 11.0$ ppm for the CASCADE pipeline, respectively. The deviation between the mean transit depths is thus $1.1 \cdot \text{SEM}_{\text{nominal}}$ or $1.9 \cdot \text{SEM}_{\text{CASCADE}}$, which is a significant but not substantial ($> 3\text{SEM}$) deviation. Second, there are more significant inconsistencies at several wavelength channels. At $1.28 \mu\text{m}$, the difference in transit depths is nearly 3σ .

We discuss further the possible sources of these inconsistencies and the implications for our retrieval results. The uncertainties in our transmission spectra include observational noise (photon noise, readout noise, dark current, etc.) and noise correlated with the detector systematics. The two data reduction pipelines, nominal, and CASCADE, are fully independent in the treatment of these uncertainties. In general, each pipeline consists of two modules: first, the light curve extraction module, which reduces the time series of spectral images into spectral light curves; second, the light curve modeling module, which fits instrument systematic and transit profile models to the light curve and measures transit depths. Both modules can cause discrepancies in the transmission spectrum.

To locate the source of the inconsistencies, we perform the following analysis: We use the light curve modeling module of the nominal pipeline (RECTE) to fit the uncalibrated light curves extracted in the CASCADE pipeline. We label the results as ‘‘CASCADExRECTE’’.

In Figure 3 (top panel), we compare the transmission spectra of nominal, CASCADE, and RECTExCASCADE pipelines without accounting for the different transit depths. In Figure 3 (bottom panel), we scale the three spectra to the same average transit depth. The second comparison, thus, shows more clearly deviations on the shape of the spectra. Furthermore, weighted residual sums of squares (RSS)

$$\text{RSS} = \sum_i^n \frac{(\text{spec}(i)_1 - \text{spec}(i)_2)^2}{(\text{uncertainty}^2(i)_1 + \text{uncertainty}^2(i)_2)}, \quad (1)$$

where we sum over the total number n of wavelength bins i , are derived to evaluate the difference statistically. For non-normalized spectra, the RSS between nominal and CASCADE is 35.2 (degrees of freedom, $\text{DOF}=19$), and the RSS between CASCADExRECTE and CASCADE is 33.4 ($\text{DOF}=19$). After normalization, the RSS between nominal and CASCADE is 32.4 ($\text{DOF}=18$), and the RSS between CASCADExRECTE and CASCADE is 11.6 ($\text{DOF}=19$).

Thus, with the same light curve extraction module and scaling the spectra to the same average depth, the light curve fitting modules in the two pipelines provide fully consistent results. This can also be seen in Figure 3 (bottom panel) by comparing the spectra CASCADExRECTE and CASCADE. All data points, except at $1.58 \mu\text{m}$ agree within 1σ with each other.

From these comparison results, we conclude: 1. difference in light curve extraction introduces random errors and causes the transmission spectra to differ at several wavelength channels; 2. difference in systematic correction causes a slight offset ($< 1\sigma$) in the average transit depths; 3. after scaled to the same average depth, the spectra from the two pipelines agree with each other, i.e., the shape of the spectra are consistent. The random errors and the offset yield apparent 3σ differences in single points in the final spectra (Figure 2).

The largest inconsistency stems from the extracted light curves and is likely a consequence of the relatively strong telescope pointing drift during the WASP-117b observations. In the

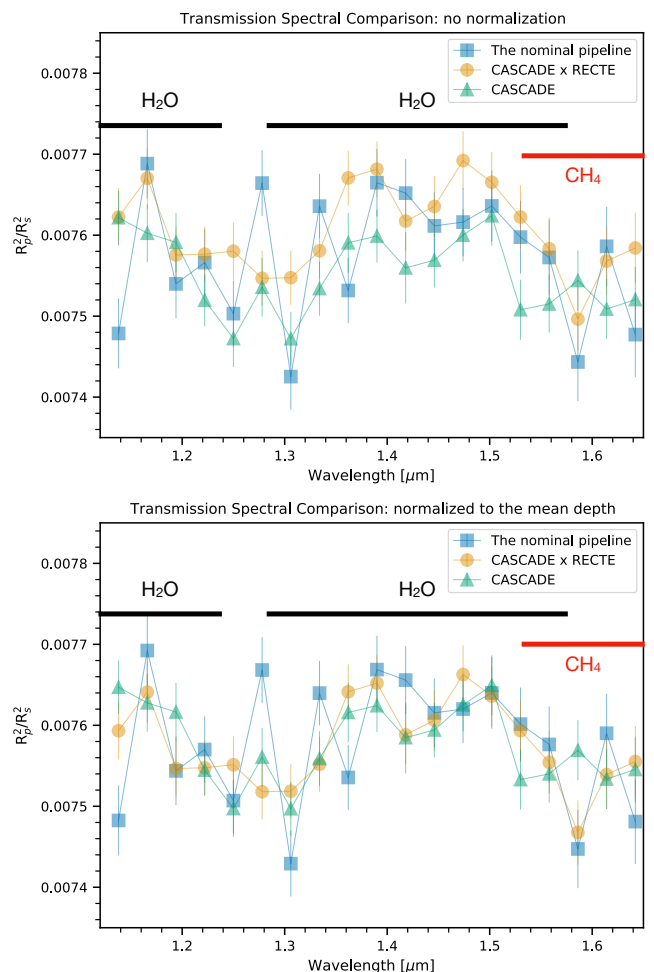


Fig. 3. Comparison of transmission spectra obtained with different pipelines. The upper panel shows the original spectra, and the lower panel shows the spectra scaled to the same average depth. After scaling, the spectra using the same raw data extraction than CASCADE but different systematic treatment (CASCADE and CASCADExRECTE) are consistent with each other.

wavelength dispersion direction, the peak-to-peak drift distance is ~ 0.4 pixels, greater than the sub- 0.1 -pixel level normally seen in HST scanning mode observations (e.g., Kreidberg et al. 2014). Different treatments in aligning the spectra between the two pipelines can lead to the inconsistency of the final transmission spectra. To demonstrate this point, we performed another reduction with a slightly modified nominal pipeline, in which we applied a Gaussian filter to the images before aligning them in the dispersion direction. The kernel of the Gaussian filter was the same as the spectral resolution element of WFC3/G141. This treatment reduced the column-to-column pixel value variations and thus decreased the influence of pointing drift. We derived the transmission spectrum using this pipeline and compared it with the CASCADE one (Figure 4). The two spectra are fully consistent with an RSS value of 15.6 ($\text{DOF}=19$).

Regardless of the treatment of the pointing drift, the shape of the spectra deriving from the nominal and CASCADE pipelines, respectively, are consistent with each other. Thus, we do not expect substantial discrepancies in the outcomes of the atmospheric retrieval for the two spectra.

Our goal is to robustly determine the planet properties, which are not dependent upon the choice of systematics models. We

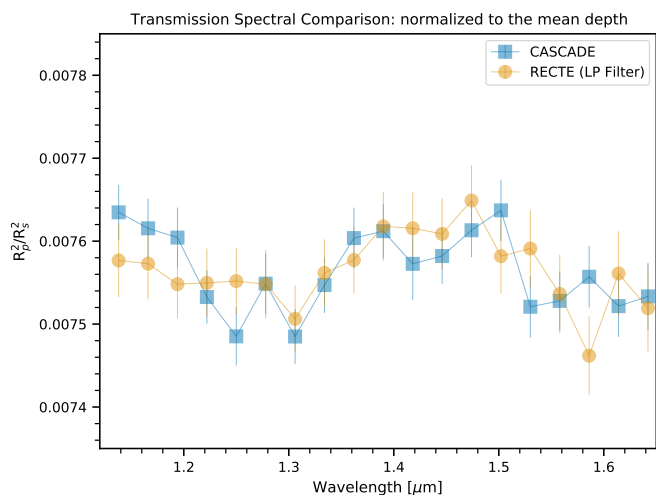


Fig. 4. Comparison of transmission spectra of a slightly modified nominal pipeline and the CASCADE pipeline. In the nominal pipeline, a Gaussian filter was applied to the images before wavelength registration to address the issue of telescope pointing drifts in the wavelength direction. The two spectra are fully consistent, supporting that discrepancies between two pipeline are due to their variations in wavelength registration in the raw light curve extraction stage.

will thus use both data pipelines for a most robust interpretation of the single epoch transit observation with HST/WFC3. In the following, we will use mainly results derived from the nominal pipeline that is well established for further analysis, e.g., with VLT/ESPRESSO (Section 2.2) and TESS data (Section 3.6).

2.2. VLT/ESPRESSO observations

To also probe gas phase absorption of Na and K in the atmosphere of WASP-117b, we observed one transit of the planet on 24/25 October 2018 under the ESO program 0102.C-0347 with the ultra-stable fibre-fed echelle high-resolution spectrograph ESPRESSO (Pepe et al. 2010) mounted on the VLT. The observation was performed with the 1-UT high-resolution and fast read-out mode. We set the exposure time as 300 s and pointed fiber B on sky. We observed the target continuously from 23:56 UT to 09:28 UT and obtained 98 spectra in total. These spectra have a resolution of $R \sim 140\,000$ and a wavelength coverage of 380–788 nm.

2.2.1. Data reduction

We reduced the raw spectral images with the ESPRESSO data reduction pipeline (version 2.0.0). The pipeline produced spectra with sky background corrected by subtracting the sky spectra measured from fiber B from the target spectra measured from fiber A. The pipeline also calculated the radial velocity (RV) of the stellar spectrum with the cross correlation technique. We discarded six spectra that have relatively low signal-to-noise ratios. Among the remaining 92 spectra, 59 spectra were observed during transit and 33 spectra were observed during the out-of-transit phase.

2.2.2. Transmission spectra of sodium and potassium

To obtain the planetary transmission spectra of sodium (Na) and potassium (K), we implemented the following procedures.

(1) Removal of telluric lines

There are telluric Na emission lines around the sodium doublet, and these emission lines were corrected using fiber B spectra. We further corrected the telluric H₂O and O₂ absorption lines by employing the theoretical H₂O and O₂ transmission model described in Yan et al. (2015). The corrections were performed in the Earth’s rest frame.

(2) Removal of stellar lines

In order to remove the stellar lines, we firstly aligned all the spectra into the stellar rest frame by correcting the barycentric Earth radial velocity (BERV) and the stellar systemic velocity. We then generated a master spectrum by averaging all the out-of-transit spectra and divided each observed spectrum with this master spectrum. The residual spectra were then filtered with a Gaussian function ($\sigma \sim 3 \text{ \AA}$) to remove large scale features.

(3) Correction of the CLV and RM effects

During the planet transit, the observed stellar line profile has variations originating from several effects. The Rossiter–McLaughlin effect (Queloz et al. 2000) and the center-to-limb variation (CLV) effect (Yan et al. 2015; Czesla et al. 2015; Yan et al. 2017) are two main effects. We followed the method described in Yan & Henning (2018) and Yan et al. (2019) to model the RM and CLV effects simultaneously. The stellar spectrum was modelled with the Spectroscopy Made Easy tool (Piskunov & Valenti 2017) and the Kurucz ATLAS12 model (Kurucz 1993). We used the stellar parameters from Lendl et al. (2014) except the $v \sin i_*$ and λ values, which are taken from the RM fit of the ESPRESSO RVs. The simulated line profile change due to the CLV and RM effects is weak and below the errors of the observed data. We subsequently corrected the CLV and RM effects for the obtained residual spectra.

(4) Obtaining the transmission spectrum

We shifted all the in-transit residual spectra to the planetary rest frame and added up all these shifted spectra. Because of the high orbital eccentricity, the planetary orbital velocity changes from $+10 \text{ km s}^{-1}$ to $+20 \text{ km s}^{-1}$ during transit. Therefore, in the planetary rest frame, the position of the stellar Na/K line is $\sim +15 \text{ km s}^{-1}$ away from the expected planetary signal.

We investigated the Na D doublet lines (5891.584 Å and 5897.555 Å) and K D₁ line (7701.084 Å). The K D₂ line (7667.009 Å) is heavily affected by the dense O₂ lines and therefore is not used in the analysis. The listed wavelengths are in vacuum. The final transmission spectra are presented in Fig. 5. There are no strong absorption features (dip) at the expected wavelengths of the planetary Na/K lines within 3σ (indicated as dashed lines in the figure).

At the wavelength regions where the stellar Na lines are located (i.e. $\sim 0.3 \text{ \AA}$ away from the expected planetary signal), there are some spectral features. But we attribute these features to the large errors of these points, because the flux inside the deep stellar Na line is significantly lower than the adjacent continuum.

The planetary Na and K lines in the VLT/ESPRESSO data are below 3σ significance. Thus, we decided not to perform atmospheric retrieval on the VLT/ESPRESSO data alone. Instead, we used the statistically significant atmosphere signal in the HST/WFC3 data in conjunction with VLT/ESPRESSO to strengthen the case that planetary Na and K lines are indeed present in the VLT/ESPRESSO data. This analysis will be presented in Section 3.1.

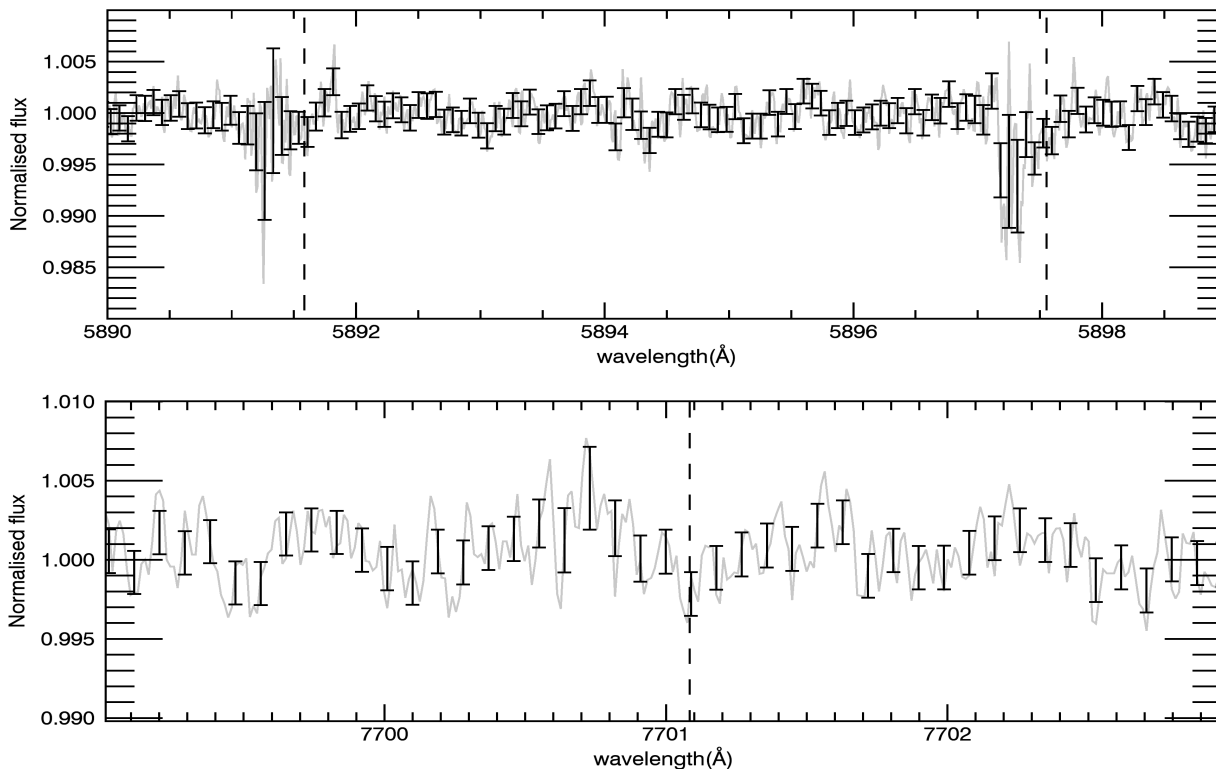


Fig. 5. Top: normalised transmission spectrum around the Na D doublet lines. Bottom: normalised transmission spectrum around the K D₁ line. The center wavelengths of these absorption lines are indicated as dashed lines. The black data points are spectra binned every seven wavelength points and the grey lines are original spectra. The stellar line profile change due to the CLV and RM effects is corrected. It should be noted that here vacuum wavelengths are displayed. In normalized flux, planetary Na and K absorption appear as weak depressions around the dashed line.

3. WASP-117b atmospheric properties and improved planetary parameters

In this section, we first explore the significance of the water detection in the HST/WFC3 and the possible existence of weak Na and K in the VLT/ESPRESSO data. We then perform atmospheric retrieval with different models to interpret the atmospheric properties of the exo-Saturn WASP-117b.

3.1. Significance of water and Na/K detection

To identify the significance of the H₂O detection in the HST/WFC3 spectrum, we follow the approach of (Benneke & Seager 2013) and run a number of forward models of similar complexity against each other, using `petitRADTRANS` (Mollière et al. 2019). In this model, we assume isothermal temperatures and a gray uniform cloud, which is modeled by setting the atmospheric opacity to infinity for $P > P_{\text{cloud}}$. Thus, P_{cloud} can be treated as the pressure at the top of a fully opaque cloud. Furthermore, we included opacities of the following absorbers: H₂O, CH₄, N₂, CO and CO₂. The mass fractions of absorbers are free parameters with priors in log space ranging from -10 to 0. For the remaining atmospheric mass, a mixture of H₂ and He is assumed with a ratio of 3:1. We retrieve the atmospheric reference pressure P_0 to reproduce the apparent size of the planet in the WFC3 wavelength range.

We quantify the significance of the observed molecular absorption features by using the `MultiNest` sampling technique that enables to quantify and compare model parameters and

their significance. `MultiNest` is implemented within the python wrapper `PyMultiNest` (Buchner 2014).

Table 1 lists the (natural) log evidences ($\ln Z$) and the Bayes factor B for different hypotheses. B is calculated via $B = \exp(\ln Z_{\text{base}} - \ln Z)$ from the `MultiNest` output for each model. Figure 6 shows the full model, including H₂O, versus the model without H₂O for data derived with both pipelines.

Following Kass & Raftery (1995), we regard B values of 1–3, 3–20, 20–150, and >150 as ‘weak’², ‘substantial’, ‘strong’, and ‘very strong’ preference for a given hypothesis, respectively. Benneke & Seager (2013, Table 2), adopted from Trotta (2008) allows us further to translate B to lower limits on σ confidence levels³.

Our statistical analysis yields “strong” Bayesian preference ($B > 20$) for the detection of water in the WASP-117b observational data for both pipeline. This corresponds to a 3σ detection.

The same approach is also used for the combined HST/WFC3 (nominal) and VLT/ESPRESSO spectrum and the possible detection of Na and K. Here, the full model is extended to also include K and Na opacities again assuming their combined mass fraction to be a free parameter, but fixing the Na/K abundance ratio to the solar value (Asplund et al. 2009).

Figure 7 shows the full model, including Na and K, versus the model without Na and K for data derived with the nominal pipeline. The combined analysis of the HST/WFC3 and

² Or ‘not worth more than a bare mention’

³ We note that Benneke & Seager (2013) adopt a different scale, where they label $B = 3$ –12 as weak, $B = 12$ –150 as ‘moderate’ and $B > 150$ as ‘strong’.

Table 1. Results of Bayesian model comparison for H₂O in HST/WFC3 and Na/K in VLT/ESPRESSO

Retrieval model	Parameters	Evidence lnZ	Bayes factor B
HST/WFC3 for H ₂ O			
Full hypothesis	$P_0, P_{\text{clouds}}, \text{H}_2\text{O}, \text{CO}_2, \text{CH}_4, \text{CO}, \text{N}_2$	nominal: -32.973 CASCADE: -19.394	nominal: baseline CASCADE: baseline
H ₂ O removed	$P_0, P_{\text{clouds}}, \text{CO}_2, \text{CH}_4, \text{CO}, \text{N}_2$	nominal: -36.042 CASCADE: -22.971	nominal: 21.5 ($3\sigma_{\text{H}_2\text{O}}$) CASCADE: 35.8 ($3\sigma_{\text{H}_2\text{O}}$)
CH ₄ removed	$P_0, P_{\text{clouds}}, \text{H}_2\text{O}, \text{CO}_2, \text{CO}, \text{N}_2$	nominal: -33.093 CASCADE: -19.300	nominal: 1.1 CASCADE: 0.9
no clouds	$P_0, \text{H}_2\text{O}, \text{CO}_2, \text{CH}_4, \text{CO}, \text{N}_2$	nominal: -33.828 CASCADE: -19.271	nominal: 2.35 CASCADE: 0.88
HST/WFC3 & VLT/ESPRESSO for Na and K			
Full hypothesis	$P_0, P_{\text{clouds}}, \text{H}_2\text{O}, \text{CO}_2, \text{CH}_4, \text{CO}, \text{N}_2, \text{Na/K}$	nominal: -174.929 CASCADE: -162.158	nominal: baseline CASCADE: baseline
Na/K removed	$P_0, P_{\text{clouds}}, \text{H}_2\text{O}, \text{CO}_2, \text{CH}_4, \text{CO}, \text{N}_2$	nominal: -176.918 CASCADE: -163.849	nominal: 7.3 ($2.5\sigma_{\text{Na,K}}$) CASCADE: 5.4 ($2.4\sigma_{\text{Na,K}}$)

VLT/ESPRESSO yields still substantial ($B > 3$) evidence for the presence of Na and K in the data, which would correspond to $\approx 2.4\sigma$, using Benneke & Seager (2013, Table 3).

Corner plots of the full set of retrieved parameters for the full retrieval models and those without H₂O and without Na/K ($B > 3$) can be found in the appendix (Figures B.1, B.2, B.3, B.4, B.5, B.6, B.7, and B.8).

3.2. Atmospheric retrieval

To constrain the atmospheric parameters of WASP-117b further, we again ran forward atmospheric models using the open-source code `petitRADTRANS` (Mollière et al. 2019), this time retrieving the planetary metallicity and C/O value directly. Our retrieval setup was applied on only the HST/WFC3 data first, and then on the combination of the HST/WFC3 and ESPRESSO data.

We constructed the retrieval forward model with the following rationale: in principle, retrievals of transmission spectra allow for many properties of the atmosphere to be constrained, such as the average terminator temperature and temperature gradient, abundances of absorbers, as well as the cloud properties such as cloud base position, scale height, average particle sizes and cloudiness fraction of the terminator (e.g., Barstow et al. 2013; Rocchetto et al. 2016; Line & Parmentier 2016; MacDonald & Madhusudhan 2017; Mollière et al. 2019; Barstow 2020). Also differences between morning and evening terminators can likely be constrained or lead to erroneous conclusions, if ignored (MacDonald et al. 2020). The same holds for variations between the day and nightside, probed across the terminator (Caldas et al. 2019; Pluriel et al. 2020). The number of free parameters, that is, the complexity of the retrieval model, needs to be justified by the quality of the data, however. Too complex models should be avoided for observations of low S/N, and in general the number of free parameters should be less than the number of data points. This prevents overfitting of the data. A useful criterion to judge whether one model is better than another, given the data, is the Bayes factor (Kass & Raftery 1995). The Bayes factor analysis will penalize those models which are too complex, given the data. However, a Bayes factor analysis should not be applied blindly. A simple (few parameters) model, that gives a good fit to the data, will always be favored, even if the model assumptions

are highly unphysical. The caveat in using Bayesian factors analysis is that Bayes factors do not know physics.

Given the limited quality of our data, we decided to keep the complexity of the retrieval 1D forward model low, with a limited number of free parameters (see Table 2). More specifically, we assumed an isothermal temperature structure, whereas the absorber abundances are here not kept as free parameters but are modelled with a chemical equilibrium model, using the chemistry code described in the appendix of Mollière et al. (2017). Our abundance treatment for WASP-117b is thus analogous to Kreidberg et al. (2018) for WASP-107b. WASP-107b could be similar in temperature and atmosphere chemistry to WASP-117b during transit.

While `petitRADTRANS` offers a wide range of different cloud parameterizations, we decided to only retrieve a gray cloud deck pressure and, optionally, a scattering-slope opacity to model small-particle hazes. The haze opacity is parameterized as

$$\kappa_{\text{haze}} = \kappa_0 \left(\frac{\lambda}{\lambda_0} \right)^\gamma \quad (2)$$

in the retrieval model, where γ determines the steepness of the scattering slope, which we constrain to $\gamma > -6$ to avoid unphysically steep slopes (Pinhas & Madhusudhan 2017; Barstow 2020). The parameters κ_0 and λ_0 are reference opacities and wavelengths, where the first is freely retrieved and the latter is set to $\lambda_0 = 0.35 \mu\text{m}$. The unit of κ_0 is $\text{cm}^2 \text{g}^{-1}$ and the haze opacity is assumed to be vertically constant.

Assuming a 1D temperature structure for transmission spectroscopy during transit could lead to underestimating the atmospheric temperature at the limbs as indicated by MacDonald et al. (2020). In addition, patchy clouds could mimic situations of high enrichment (Line & Parmentier 2016), which is another possible limitation to keep in mind.

3.3. HST/WFC3 Atmosphere retrieval

In the following, we will discuss constraints on the atmospheric composition of WASP-117b, based on atmospheric retrieval of the HST/WFC3 transmission spectrum using the nominal (Section A.1) and the CASCADE pipeline (Section A.2), respectively.

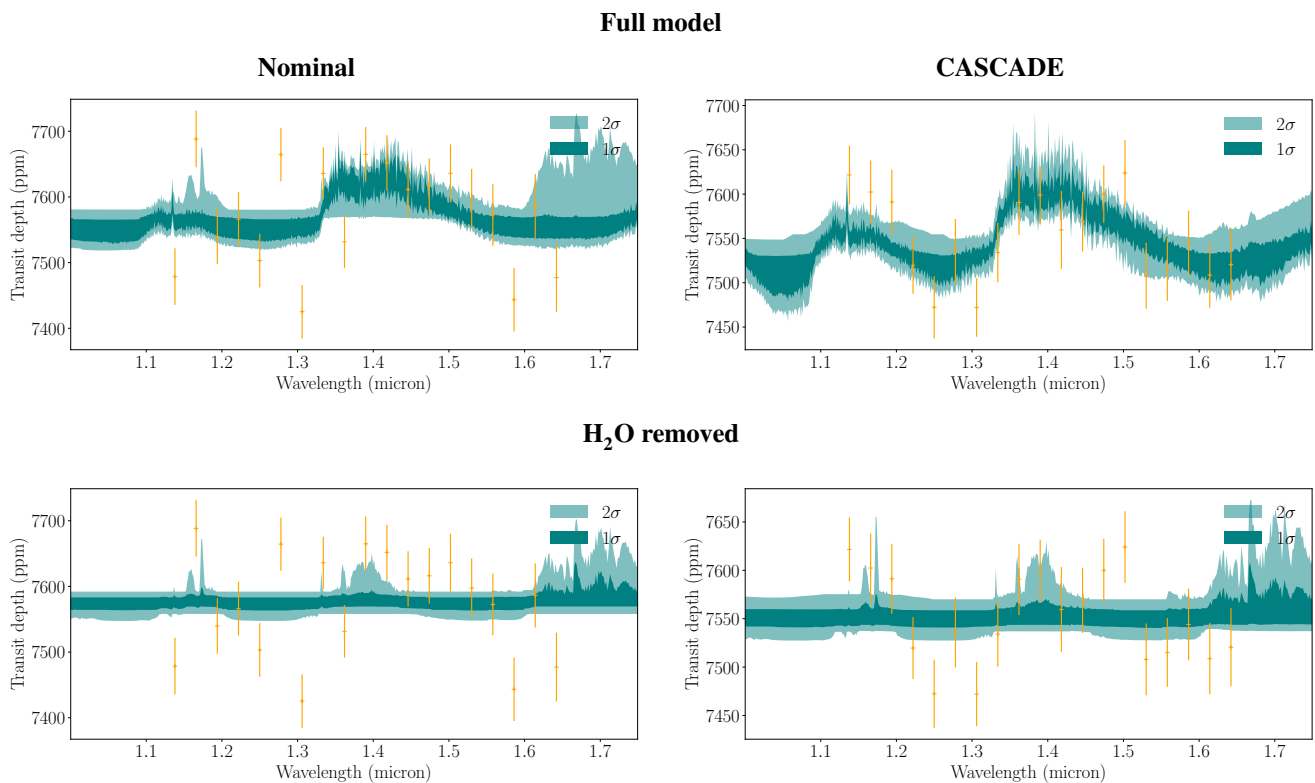


Fig. 6. Top: Full retrieval model is fit to WASP-117b transmission spectrum reduced with the nominal pipeline (left) and CASCADE (right). **Bottom:** Retrieval model with H_2O removed fit to WASP-117b transmission spectrum reduced with the nominal (left) and CASCADE pipeline (right).

For all spectra, retrieved atmosphere models with confidence within 1σ (dark green) and 2σ (light green) are shown.

Table 2. List of models used for WASP-117b atmosphere retrieval

Model name	prior in parameters	short description
<i>Model 1</i>	$T \in [500, 1500] \text{ K}$ $\log(P_0/1\text{bar}) \in [-12, +2]$ $\text{C/O} \in [0.1, 1.6]$ $[\text{Fe}/\text{H}] \in [-1.5, +3]$ $\log(P_{\text{cloud}}) \in [-6, +2]$	high $[\text{Fe}/\text{H}]$ & gray cloud
<i>Model 2</i>	as in Model 1 except $[\text{Fe}/\text{H}] \in [-1.5, +1.75]$	low $[\text{Fe}/\text{H}]$ & gray cloud
<i>Model 3</i>	as in Model 1 except $[\text{Fe}/\text{H}] \in [-1.5, +1.75]$ $\gamma \in [-6, 0]$ $\log(\kappa_0) \in [-10, +10]$	low $[\text{Fe}/\text{H}]$ & gray cloud & haze layer

We employed several models with physically motivated priors to constrain the atmospheric properties of WASP-117b. The models and their priors are listed in Table 2. *Model 1* and *Model 2* represent atmospheric models with isothermal temperature, equilibrium chemistry and a gray cloud deck. *Model 1* sets weak constraints on metallicity within $[-1.5, +3]$, *Model 2* sets constraints to lower metallicity $[\text{Fe}/\text{H}] < 1.75$. *Model 3* assumes the same parameters and priors as *Model 2* and adopts additionally a haze layer.

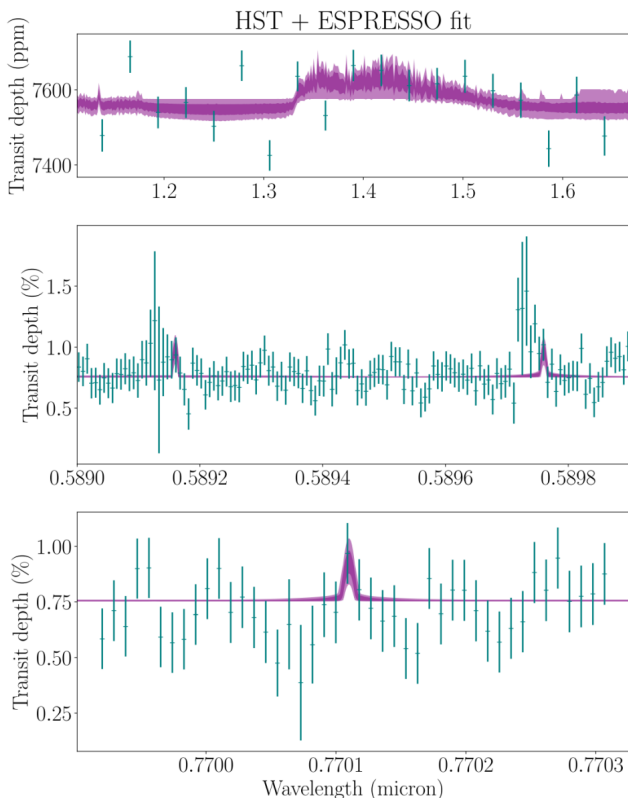
3.3.1. *Model 1* - condensate clouds and weakly constrained $[\text{Fe}/\text{H}]$

Figure 8 displays the 2-98 and 16-84 percentile envelopes of the retrieved transmission spectra of *Model 1*, together with the WASP-117b HST data, reduced with the nominal and CASCADE pipeline, respectively. The corner plots with the retrieved properties based on *Model 1* are displayed in Figures B.9, B.10 and B.15, and the results are listed in Table 3. The retrieval based on the nominal spectrum yields a relatively high temperature of $1129^{+228}_{-289} \text{ K}$, whereas retrieval based on the CASCADE spectrum would indicate a rather low temperature of $821^{+264}_{-226} \text{ K}$. The discrepancy in temperature can be explained by data reduction differences, that lead in the nominal spectrum towards an overall deeper transit depth, that is, a more inflated atmosphere, which can be achieved by attaining higher temperatures compared to the CASCADE spectrum. However, both temperatures are within one sigma of each other, which again indicates that this shift is not substantial. We thus conclude that the atmospheric temperature is not well constrained with our data, at least when using *Model 1*.

Retrieval with *Model 1* further suggests very large metallicities $[\text{Fe}/\text{H}] > 2.2$ based on both spectra. At the same time, a cloud top located relatively deep in the atmosphere ($p > 10^{-4} \text{ bar}$) is inferred and the reference pressure P_0 is set high in the atmosphere ($P_0 < 10^{-5.5}$) to reconcile the relatively large transit depth of this inflated exo-Saturn with the high metallicities. The high metallicity solutions thus indicate relatively clear skies with very small atmospheric scale heights. These results indicate that the water feature is strongly muted and that condensate cloud modelling alone can not properly account for the

Table 3. Median Parameters and 68% Confidence Intervals for *Models 1, 2* and *3* retrieved with HST/WFC3 spectra based on two different data reduction pipelines.

Parameter	<i>Model 1</i>		<i>Model 2</i>		<i>Model 3</i>	
	Nominal	CASCADE	Nominal	CASCADE	Nominal	CASCADE
Temperature [K]	1129 ⁺²²⁸ ₋₂₈₉	821 ⁺²⁶⁴ ₋₂₂₆	1002 ⁺³⁴⁸ ₋₃₅₀	674 ⁺³⁹² ₋₁₃₅	860 ⁺³⁷¹ ₋₂₅₇	738 ⁺³⁶⁰ ₋₁₅₇
Pressure log($P_0/1\text{bar}$)	-6.69 ^{+0.99} _{-1.21}	-7.20 ^{+1.11} _{-1.51}	-4.44 ^{+1.52} _{-0.97}	-4.45 ^{+1.47} _{-1.01}	-4.49 ^{+1.33} _{-1.13}	-4.89 ^{+1.23} _{-1.09}
[Fe/H]	2.58 ^{+0.26} _{-0.37}	2.55 ^{+0.28} _{-0.35}	0.66 ^{+0.85} _{-1.64}	0.54 ^{+0.97} _{-1.62}	0.41 ^{+0.97} _{-1.26}	0.67 ^{+0.81} _{-1.33}
C/O	0.25 ^{+0.17} _{-0.10}	0.27 ^{+0.24} _{-0.11}	0.37 ^{+0.30} _{-0.19}	0.36 ^{+0.41} _{-0.19}	0.40 ^{+0.48} _{-0.20}	0.38 ^{+0.40} _{-0.19}
Cloud top log($P_{\text{cloud}}/1\text{bar}$)	-1.32 ^{+2.24} _{-2.44}	-0.78 ^{+1.77} _{-1.77}	-3.69 ^{+1.42} _{-0.97}	-3.30 ^{+1.29} _{-1.03}	-3.69 ^{+1.27} _{-1.15}	-2.97 ^{+2.32} _{-1.49}
log(κ_0)	-	-	-	-	-4.91 ^{+3.61} _{-3.10}	-1.99 ^{+2.84} _{-5.22}
Scattering slope γ	-	-	-	-	-3.55 ^{+1.89} _{-1.57}	-2.61 ^{+1.59} _{-2.09}
volume fractions within 1σ						
log(H_2O) at 10^{-4} bar	-0.62 ^{+0.26} _{-0.51}	-0.75 ^{+0.34} _{-0.66}	-2.70 ^{+1.15} _{-1.63}	-2.68 ^{+1.17} _{-1.77}	-2.96 ^{+1.21} _{-1.50}	2.66 ^{+1.07} _{-1.66}
log(CH_4) at 10^{-4} bar	-13.19 ^{+3.87} _{-6.66}	-9.34 ^{+5.38} _{-5.92}	-9.89 ^{+5.39} _{-2.88}	-4.75 ^{+1.58} _{-5.43}	-7.55 ^{+3.63} _{-4.41}	-5.28 ^{+2.07} _{-5.05}
3σ upper limits of CH_4 volume fractions						
CH_4 at 10^{-4} bar	$8.6 \cdot 10^{-2}$	$2.0 \cdot 10^{-1}$	$1.6 \cdot 10^{-2}$	$1.9 \cdot 10^{-2}$	$1.6 \cdot 10^{-2}$	$1.7 \cdot 10^{-2}$


Fig. 7. Full retrieval model fit to the WASP-117b transmission spectrum in WFC3 and VLT/ESPRESSO with the nominal pipeline with Na and K. The WFC3 data are shown in the top panel, the middle panel shows the Na doublet and the bottom the K D_1 line. The retrieval model without Na and K (not shown) is a flat line in the optical and indistinguishable from the full model without Na and K in the WFC3 NIR range. For all spectra, retrieved atmosphere models with confidence within 1σ (dark green) and 2σ (light green) are shown.

shape of the water signal. Instead, the model assumes high mean molecular weight with more than $100\times$ solar metallicity, irrespective of which data reduction pipeline is used.

Furthermore, retrieval based on both the nominal and CASCADE spectra tend to yield subsolar C/O values with an upper limit of 0.42 and 0.51 respectively. Due to this, the CH_4 content is retrieved within 1σ to be below 1.1×10^{-4} volume fraction at $p = 10^{-4}$ bar, when using data retrieved with the CASCADE spectrum and even below 5.7×10^{-10} volume fraction when using the nominal pipeline. However, we note that the 3σ range is very large (see Figure B.15) such that we cannot claim strong significance for these low CH_4 abundances.

Similar low C/O values were also found for WASP-107b by Kreidberg et al. (2018). These authors likewise attribute the low C/O values to the absence of CH_4 within the WFC3/G141 wavelength range, which is consistent with our retrieved low abundances of CH_4 . If WASP-117b is colder than 800 K during transit and thus in a similar temperature range to WASP-107b then the very low abundance of CH_4 could indicate disequilibrium chemistry. We explore this possibility in Section 4.

We further note that we find a tail of solutions with lower metallicity and high cloudiness in the retrieved parameters based on *Model 1* fitted to both spectra, the nominal and the CASCADE spectrum (See Figures B.9 and B.10 in the [Fe/H] – P_{cloud} corners, indicated with a black ellipse). We will thus explore lower metallicity solutions more carefully in the next sections.

3.3.2. *Model 2* - condensate clouds and [Fe/H] < 1.75

We designed *Model 2* with a constraint on allowed metallicities as agnostically as possible to select for the tail of cloudy low metallicity solutions of *Model 1*. We adapted again the simplest (uniform) cloud model for retrieval, because the information content in the muted observed water spectrum observed with HST/WFC3 is too limited to warrant a more complex cloud

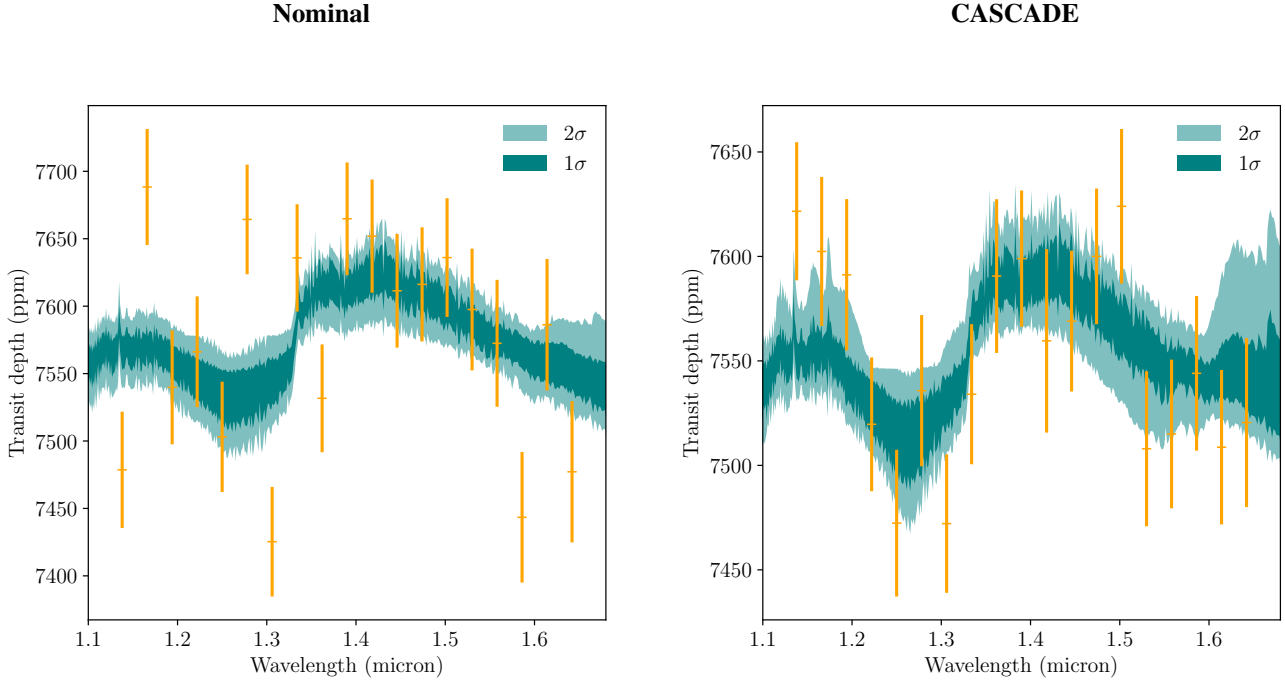
Model 1

Fig. 8. Left: *Model 1* (unconstrained [Fe/H] and grey cloud) fit to WASP-117b transmission spectrum reduced with the nominal data pipeline by Zhou et al. (2017). **Right:** *Model 1* (unconstrained [Fe/H] and grey cloud) fit to WASP-117b transmission spectrum reduced with the data pipeline CASCADE.

For both spectra, retrieved atmosphere models with confidence within 1σ (dark green) and 2σ (light green) are shown. These models were derived with `petitRADTRANS` (Mollière et al. 2019) and indicate a clear atmosphere of high metallicity, where the large mean molecular weight leads to a muted water spectrum.

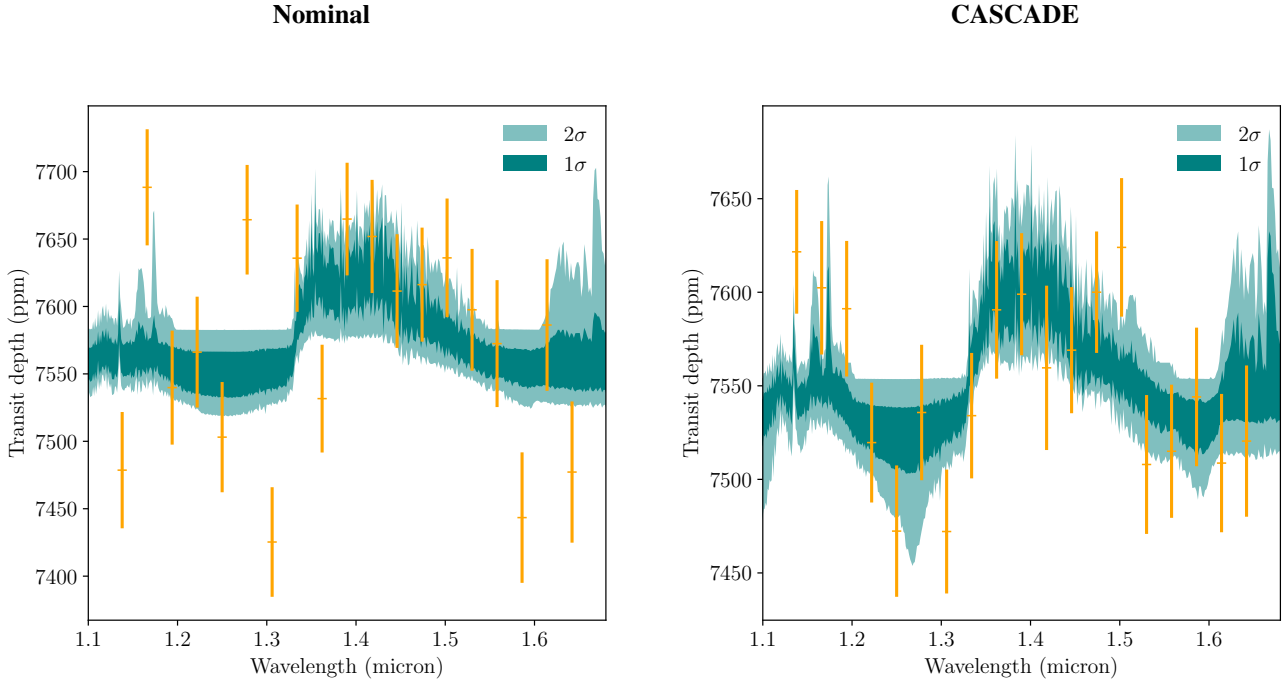
Model 2

Fig. 9. Left: *Model 2* (prior [Fe/H] < 1.75 and grey cloud) fit to WASP-117b transmission spectrum reduced with the data pipeline by Zhou et al. (2017). **Right:** *Model 2* (prior [Fe/H] < 1.75 and grey cloud) fit to WASP-117b transmission spectrum reduced with the data pipeline CASCADE.

For both spectra, retrieved atmosphere models with confidence within 1σ (dark green) and 2σ (light green) are shown. These models were derived with `petitRADTRANS` (Mollière et al. 2019) and indicate a cloudy atmosphere with a muted water feature.

model with e.g. patchy clouds as proposed by Line & Parmentier (2016).

We set an upper limit of $56\times$ solar metallicity, that is, we imposed a prior for $[\text{Fe}/\text{H}] < 1.75$. Figure 9 displays the best fit of *Model 2* to the WASP-117b HST data, reduced with the nominal and CASCADE pipelines, respectively. The detailed corner plots with the retrieved properties based on *Model 2* are displayed in Figures B.11, B.12 and B.16. Table 3 lists concisely the results of the retrieval.

We note that the retrieved atmospheric metallicity for WASP-117b is not well constrained for *Model 2* with a tendency to still favor solutions at the higher end of the imposed prior. On the other hand, no matter which data reduction pipeline is used, nominal or CASCADE, in both cases we retrieve solutions with better constrained cloud deck located higher in the atmosphere compared to *Model 1*. With *Model 2*, the cloud deck is retrieved to lie between $p = 10^{-5.1}$ and $p = 10^{-2.2}$ bar. Since we excluded higher metallicities that reduce the scale height to very low values, the reference pressure P_0 is deeper in the atmosphere compared to *Model 1*. In other words, in *Model 2* cloudy solutions are favored to explain the muted water feature.

Sub-solar C/O values that indicate low abundances of CH_4 are also favored by *Model 2*. However, we report a division between possible solutions within our constrained metallicity range. There is a tail of high C/O > 1 solutions (Figures B.11 and B.12), which are correlated in the posterior of our retrieval with low metallicities ($[\text{Fe}/\text{H}] < -0.5$).

For the C/O > 1 solutions, we further find that the CH_4 volume fraction at $p = 10^{-4}$ bar is greater than that of H_2O . For C/O < 1 solutions, the CH_4 abundances are always lower than the H_2O abundances. A dominance of CH_4 over H_2O is expected for high C/O ratios (Madhusudhan 2012; Mollière et al. 2015). However, we stress that these high C/O solutions only represent a small subset of solutions, associated with low metallicities $[\text{Fe}/\text{H}] < -0.5$, and only occur when we impose a metallicity constraint of $[\text{Fe}/\text{H}] < 1.75$ on retrieval. The majority of the solutions are high metallicity solutions ($[\text{Fe}/\text{H}] > 1$) that still strongly favor solar to sub-solar C/O ratios also in *Model 2*.

The low C/O ratios appear again to correspond to low CH_4 abundances (in any case lower compared to H_2O abundances), where we retrieved within 1σ CH_4 abundances below 6.7×10^{-4} volume fraction at 10^{-4} bar. Also for *Model 2*, the 3σ envelope of CH_4 abundances is very large (Figure B.16).

3.3.3. *Model 3* - condensate clouds, prior $[\text{Fe}/\text{H}] < 1.75$ and haze layer

Another possibility, which may explain the muted observed water spectrum, could be the existence of a haze layer on top of the cloudy atmosphere. This possibility was explored with *Model 3*. Figure 10 displays the best fit of *Model 3* to the WASP-117b HST data, reduced with the nominal and CASCADE pipelines, respectively. The detailed corner plots with the retrieved properties based on *Model 3* are displayed in Figures B.13, B.14, and B.17. A summary of the parameters retrieved with this model is given in Table 3.

For the CASCADE spectrum, *Model 3* yields a bi-modal posterior distribution for the haze opacity. The median value is $\log(\kappa_0) = -1.99^{+2.84}_{-5.22}$, with the high- κ_0 peak occurring at $\log(\kappa_0) = 0.15$ and the low peak occurring at $\log(\kappa_0) = -5.8$. The low peak is consistent with the posterior of *Model 3* for the nominal spectrum while the high peak indicates some of the models are hazy with a moderate scattering slope of $\gamma = -2.61^{+1.59}_{-2.09}$ (Figure 10,

Table 4. Statistical analysis of WASP-117b HST data for different models.

Model	$\ln Z$	Bayes factor B	χ^2
Nominal spectrum			
<i>Model 1</i>	-31.59	baseline	47.9
<i>Model 2</i>	-33.05	4.3	
<i>Model 3</i>	-34.5	18.4	
CASCADE spectrum			
<i>Model 1</i>	-17.83	baseline	19.1
<i>Model 2</i>	-20.46	13.9	
<i>Model 3</i>	-21.28	31.5	

right). High values of κ_0 also correspond to a gray cloud deck that can lie deeper in the atmosphere compared to *Model 2*. The water feature is for some models inside the *Model 3* framework muted by the combined effect of condensed clouds and the haze layer.

For the nominal spectrum, however, *Model 3* is clearly a less good fit (Figure 10, left). Comparison between the corner plots Figure B.13 and Figure B.14 show that the retrieved haze layer properties κ_0 and γ in the nominal spectrum are more uniformly spread across the allowed parameter range compared to the CASCADE spectrum. Generally, the retrieved parameters based on the nominal spectrum are, however, for *Model 3* well within 1σ of the parameters retrieved with the CASCADE spectrum as a basis. The sub-set of hazy solutions identified in the posterior of retrieval with *Model 3* based on the CASCADE spectrum are thus not substantial enough to indicate a strong disagreement between data reduction pipelines that are used in this work.

The metallicity is like in *Model 2* unconstrained in *Model 3* within imposed low metallicity limits of $[\text{Fe}/\text{H}] = [-1.5, 1.75]$, irrespective of which pipeline is used. The temperature is again not well constrained in *Model 3*, as can be seen when comparing Figure B.14 and Figure B.12.

In *Model 3*, we identify again a tail of high C/O ratio solutions as in *Model 2*. Most solutions, especially those with $[\text{Fe}/\text{H}] > 1$, favor, however, subsolar C/O ratios. As noted in previous subsections, low C/O values are indicative of low abundances of methane. This is reflected again by retrieved CH_4 abundances smaller than 10^{-4} volume fraction at $p = 10^{-4}$ bar within 1σ for the nominal reduction pipeline. We note that fitting *Model 3* to the CASCADE spectrum, allows even up to $10^{-3.2}$ volume fraction at $p = 10^{-4}$ bar within 1σ .

The significance of the molecular absorption feature as well as that of a haze layer is investigated in the following.

3.4. Significance of differences in metallicity and haze layer

To quantify the different models that we used for retrieval, we compare now *Model 1*, *2* and *3* with each other, using the same method as in Section 3.1. In Table 4, we list again the (natural) log evidences ($\ln Z$) and the Bayes factor B .

According to this statistical analysis, *Model 1*, a model with high atmospheric metallicity ($[\text{Fe}/\text{H}] \geq 2.2$) and clear skies fits the data best compared to the lower metallicity, cloudy models *Model 2* and *Model 3*, where the latter also assumes a haze layer on top. This is true for both pipelines.

The Bayesian preference is, however, larger for the CASCADE spectrum compared to the nominal spectrum. Based on data reduced with the CASCADE pipeline, the preference is

Model 3

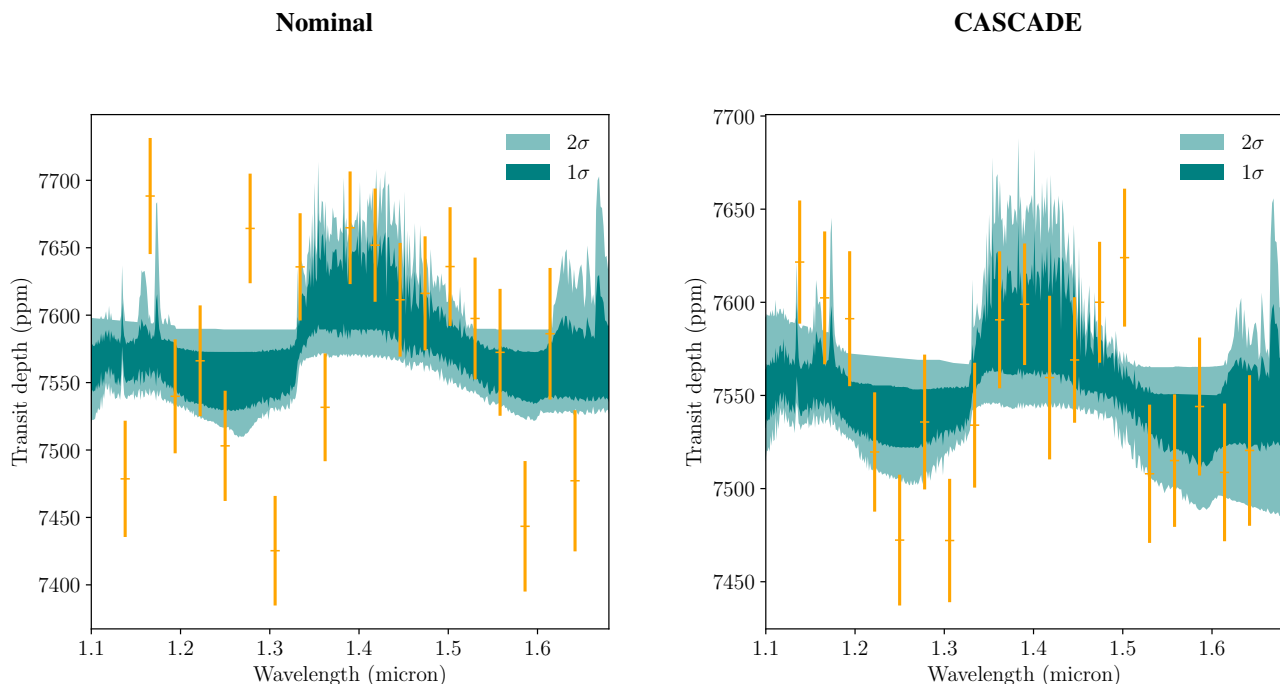


Fig. 10. Left: *Model 3* (grey cloud and haze layer with prior $[\text{Fe}/\text{H}] < 1.75$ and $\gamma > -6$) fit to WASP-117b transmission spectrum reduced with the nominal data pipeline by Zhou et al. (2017). **Right:** *Model 3* (grey cloud and haze layer with prior $[\text{Fe}/\text{H}] < 1.75$ and $\gamma > -6$) fit to WASP-117b transmission spectrum reduced with the data pipeline CASCADE.

For both spectra, retrieved atmosphere models with confidence within 1σ (dark green) and 2σ (light green) are shown. These models were derived with `petitRADTRANS` (Mollière et al. 2019) and indicate a cloudy atmosphere with a muted water feature.

“substantial” to “strong”. Based on data reduced with the nominal spectrum, the preference is still “substantial”, that is, $1 - 2\sigma$.

Theoretical predictions of Thorngren & Fortney (2019) indicate that up to $200\times$ solar metallicity are in principle possible for Saturn-mass exoplanets like WASP-117b. We again point out the possible degeneracy of high metallicity with patchy cloud solutions (Line & Parmentier 2016).

We also added a χ^2 analysis for *Model 1* to quantify yet again agreement of the data derived from different pipelines in comparison with the best fit physical model (Table 4). The χ^2 deviation as well as the scatter in data points below $1.35 \mu\text{m}$ in Figure 1 indicates some problem with the nominal pipeline. We demonstrated in Section 2.1.2 that the discrepancy below $1.35 \mu\text{m}$ is likely caused by the difference in calibrating the telescope’s pointing movement in the dispersion direction. Therefore, we performed retrieval analyses on spectra obtained using both pipelines. Since we found fully consistent results, this confirms the high fidelity of our conclusions.

Our work illustrates that even with the well established nominal pipeline, one has to be aware of instrumental effects that may yield a worse performance as expected. It further highlights the importance of using independent data reduction pipelines to confirm the analysis results. Still, better and additional data e.g. in the optical range are needed for further constraints of cloud and haze coverage of WASP-117b and thus atmospheric metallicity. We already obtained additional observations of WASP-117b with VLT/ESPRESSO (Section 2.2) to support the HST/WFC3 observation. In addition, we can analyze WASP-117b transit data obtained by the TESS satellite (Section 3.6).

3.5. Rossiter–McLaughlin effect measured with VLT/ESPRESSO

From our high resolution ESPRESSO data we could also improve the constraints on the stellar rotation and spin-orbit alignment of WASP-117b, via the Rossiter–McLaughlin (RM) effect. The RM of the system was initially measured by Lendl et al. (2014) using one transit dataset from the HARPS observation. We fitted the RM effect using our ESPRESSO data to update the obliquity parameters. We applied a Markov chain Monte Carlo (MCMC) approach using the `emcee` tool (Foreman-Mackey et al. 2013). The RM effect was modelled with the python code `RmLe11` from the `PyAstronomy` library⁴ (Czesla et al. 2019). The projected stellar rotation velocity ($v \sin i_\star$), projected spin-orbit angle (λ), and systemic velocity (V_{sys}) were set as free parameters and we fixed other parameters to the values in Lendl et al. (2014). The RV curve together with the best-fit model are presented in Fig. 11. The retrieved parameters are listed in Table 5.

We did not use these updated parameters in the analyses for the rest of this work, for which the original data by Lendl et al. (2014) was already sufficient to reduce the HST/WFC3 and TESS data before the updated VLT/ESPRESSO data was available to us. Still, we present the updated RM values here for completeness sake and for inclusion in future work.

3.6. TESS transit data

We further found that the Transiting Exoplanet Survey Satellite (TESS) has acquired four observations of WASP-117 between

⁴ <https://github.com/sczesla/PyAstronomy>

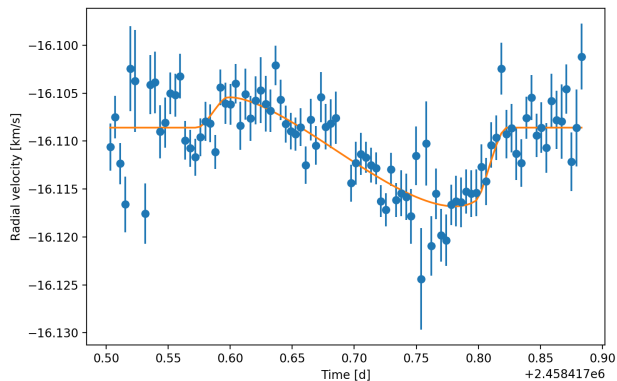


Fig. 11. ESPRESSO RVs obtained on 25 October 2018 during a transit of WASP-117b. The barycentric Earth radial velocity and the stellar orbital velocity are corrected. The orange line shows the best-fit model of the Rossiter-McLaughlin effect.

Table 5. Retrieved parameters from the Rossiter-McLaughlin effect.

This work	
$v \sin i_{\star}$	$1.46 \pm 0.14 \text{ km s}^{-1}$
projected spin-orbit angle λ	$-46.9^{+5.5}_{-4.8} \text{ deg}$
systemic velocity V_{sys}	$-16.1086 \pm 0.0004 \text{ km s}^{-1}$
Lendl et al. (2014)	
$v \sin i_{\star}$	$1.67^{+0.31}_{-0.24} \text{ km s}^{-1}$
projected spin-orbit angle λ	$-44 \pm 11 \text{ deg}$

August 26 2018 and October 13 2018 during Sectors 2 and 3 of TESS’ primary mission, covering four consecutive transits of WASP-117b⁵. These transit data are more accurate than the transit depth measured from the ground as reported in the discovery paper (Lendl et al. 2014) from the WASP South survey and could potentially put further constraints on the cloud properties of WASP-117b.

Interestingly, the reported TESS transit depth of $7200 \pm 150 \text{ ppm}$ was found to be very shallow (albeit within 3σ) compared to the value reported by Lendl et al. (2014) ($8030^{+550}_{-480} \text{ ppm}$) and by our HST/WFC3 nominal transit depth ($7573 \pm 43 \text{ ppm}$). We thus decided to perform an independent analysis on both the published TESS photometry and the target-pixel files (TPFs) of this target, to verify this slight discrepancy. For the former, we used the PDC lightcurve published at MAST⁶, which we fitted using juliet (Espinoza et al. 2019). As priors for this fit, we used the eccentricity and argument of periastron as reported by Lendl et al. (2014) as priors ($e = 0.302 \pm 0.023$, argument of periastron $\omega = 242 \pm 2.7 \text{ deg}$). To account for the systematic trends in the data, we used a Gaussian Process (GP) with a Matérn 3/2 kernel, whose parameters had wide priors — the time-scale of the process had a prior between 10^{-5} and 1000 days, whereas the square-root of the variance of the process had a prior between 10^{-3} to 100 ppm. Independent GPs were used for each sector, which also had an added white-noise component modelled as a added gaussian-noise to the GP with a large prior on the square-root of its variance between 0.01 and 1000 ppm, and independent out-of-transit flux offsets with gaussian priors centered around 0, but with a standard deviation of 10^5 ppm . For the transit depth and impact parameter we used the uninformative

Table 6. WASP-117b transit depths

Survey	transit depth	wavelength range
WASP South	$8030^{+550}_{-480} \text{ ppm}$	0.4 - 0.7
TESS (ExoFOP)	$7200 \pm 150 \text{ ppm}$	0.6 - 1 μm
TESS (JULIET)	$7267 \pm 135 \text{ ppm}$	0.6 - 1 μm
WFC3 (nominal)	$7573 \pm 43 \text{ ppm}$	1.125 - 1.65 μm

sampling scheme proposed in Espinoza (2018), which samples the entire range of physically plausible values for those parameters. A wide log-uniform prior was defined for the stellar density between 100 and 10,000 kg/m^3 , and the efficient sampling scheme of Kipping (2013) was used to model the limb-darkening effect through a quadratic law, where the coefficients were left as free parameters of the fit. Finally, relatively wide priors were defined for the ephemerides of the orbit: a normal distribution centered around 10 with a standard deviation of 0.1 days for the period, and a normal distribution centered around 2458357.6 with a standard deviation of 0.1 days for the time-of-transit center. No dilution contamination was applied in this fit, as this is corrected in the PDC photometry.

Our juliet analysis on the PDC lightcurve reveals a transit depth within 1-sigma with the ExoFOP reported transit depth. Next, we went on to test if the PDC algorithm might be diluting the transit signal due to, e.g., too strong detrending. To this end, we used the TPFs reported in MAST to extract our own photometry for this target. We used apertures consisting of 1, 2 and 3 pixels around the brightest pixel, which accounts for apertures of about 30”, 40” and 50” around the target. To detrend the data we used Pixel-Level Decorrelation (PLD Deming et al. 2015), initially used for Spitzer but which has been successfully applied to photometric data from missions like K2 (Luger et al. 2016). The detrending was performed simultaneously with the transit model defined above, in order to account for all the uncertainties simultaneously on each of the apertures. The results from this fit were in excellent agreement with the transit depths obtained from the PDC algorithm; for example, for our smallest aperture, we obtained a transit depth of $7144 \pm 177 \text{ ppm}$. Given no strong dilution is expected in this smaller aperture (judging from Gaia sources around WASP-117), this analysis gives us confidence in the fact that the relatively shallower TESS transit depths are in fact real and not related to dilution or detrending methods. This result implies that the TESS transit depth is shallow due to a physical mechanism: either spectral contamination due to stellar activity of the host star WASP-117 or due to clouds and hazes in the atmosphere of WASP-117b.

3.6.1. Stellar activity and clouds as a possible explanation for TESS data discrepancy

Stellar activity can add systematic offsets to the measured transit depth of an exoplanet like WASP-117b, which can make it difficult to compare observations at different wavelength ranges and taken at different epochs (Rackham et al. 2019).

In the WASP-117b discovery paper, Lendl et al. (2014) did not detect any variability greater than 1.3 mmag with 95% confidence. We independently investigated the variability of WASP-117 using ASAS-SN Sky Patrol⁷ (Shappee et al. 2014; Kochanek et al. 2017), which includes V-band photometric monitoring of WASP-117 for the 2014–2017 observing seasons taken with two cameras, ‘bf’ and ‘bh’. We considered only the data for the 2014

⁵ <https://exofop.ipac.caltech.edu/tess/target.php?id=166739520>

⁶ <https://archive.stsci.edu/>

⁷ <https://asas-sn.osu.edu/>

and 2015 observing seasons using the ‘bf’ camera. Data collected using the ‘bh’ camera, including some of the 2015 season and all later seasons, appear to suffer from a strong instrumental systematic. The RMS scatter of the data included in this analysis is 11.5 mmag, while the mean measurement uncertainty is 4.5 mmag, suggesting that some variability is present. A Lomb-Scargle periodogram analysis (Lomb 1976; Scargle 1982), implemented in `astropy`⁸, consistently reveals a periodicity with a full amplitude of 9.4 mmag, though the period with the largest power depends on the observing season included. Considering the ASAS-SN data, we conservatively adopt 9.4 mmag or 1% as the reference variability level for WASP-117 in this analysis.

We modeled the variability of WASP-117 using the method detailed by Rackham et al. (2018), including considerations for FGK dwarfs (Rackham et al. 2019). In brief, the approach involves adding spots and faculae to a large set of model photospheres to establish the probabilistic relationship between active region coverage and rotational variability for a set of stellar parameters. The observed variability of a star is then used to estimate its active region coverage and the related stellar contamination of transmission spectra from the system. We set the photosphere temperature to the stellar effective temperature determined by Lendl et al. (2014). We further adopted the surface gravity, stellar surface gravity, and metallicity from that work. We determined spot and facula temperatures from the scaling relations detailed by Rackham et al. (2019). We used the spot size and initial facula-to-spot areal ratio⁹ from the ‘solar-like case’ outlined by Rackham et al. (2018). Table 7 summarizes the adopted parameters.

Figure 12 illustrates the modeled variability of WASP-117 as a function of spot covering fraction. We find that the adopted variability amplitude of WASP-117 corresponds to full-disk spot and facula covering fractions of $F_{\text{spot}} = 4_{-2}^{+6}\%$ and $F_{\text{fac}} = 29_{-9}^{+19}\%$, respectively, at 1σ confidence. If present outside of the transit chord, these active regions could alter the observed transit depths. Figure 13 illustrates the wavelength-dependent stellar contamination factor ϵ_λ , the ratio of the observed transit depth to the true transit depth (see Eq. 2 of Rackham et al. 2018), produced by these active region coverages over the HST/WFC3 G141 bandpass. We find the effect of unocculted spots dominates over that of unocculted faculae, producing a net increase in transit depths ($\epsilon_\lambda > 1$). Over the complete G141 bandpass, we estimate that transit depths can be inflated by $1.4_{-0.6}^{+3.1}\%$ at 1σ confidence. This inflation is relative to a measurement in the same wavelength range that is completely unaffected by stellar activity. No strong spectral features are apparent in the contamination signal besides a slight increase toward shorter wavelengths: at $1.1 \mu\text{m}$, transit depths may be increased by $1.5_{-0.7}^{+3.8}\%$, while at $1.7 \mu\text{m}$ the increase is limited to $1.1_{-0.5}^{+2.3}\%$. We note that while the scale of ϵ_λ is comparable to the precision of our HST/WFC3 G141 spectrum, the lack of strong spectral features in the contamination spectrum provides reassurance against spectral features we see in the near-infrared spectrum actually resulting from stellar contamination.

Figure 14 shows the relative increase of the planetary radius in the near infrared ($1.1 \mu\text{m}$) between 1% and 4%, the TESS transit depths and HST/WFC3 spectrum. If the TESS data (observed

Table 7. Parameters used in stellar heterogeneity analysis.

Parameter	Description	Value
T_{phot}	Photosphere temperature	5460 K
[Fe/H]	Metallicity	0.14
$\log g$	Surface gravity	4.37
T_{spot}	Spot temperature	4780 K
T_{fac}	Facula temperature	5600 K
R_{spot}	Spot radius	2°
α	Initial facula-to-spot areal ratio	10
A_{ref}	V-band variability amplitude	2%

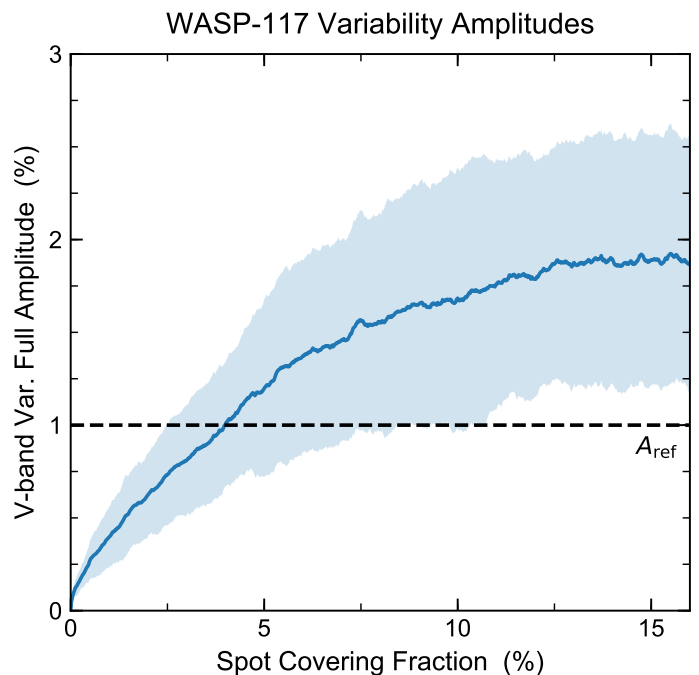


Fig. 12. Modeled rotational variability amplitudes of WASP-117 in V-band as a function of spot covering fraction. The median estimate (blue line) and 1σ confidence interval (blue shaded region) are shown.

Table 8. Stellar contamination factors in the TESS and WFC3/G141 bandpasses for the spots-only models.

	Band pass	Value
ϵ_{WFC3}	1.1 – 1.7 μm	$1.014_{-0.006}^{+0.031}$
ϵ_{TESS}	0.6 – 1.0 μm	$1.03_{-0.01}^{+0.06}$

in 9/2018) would have been taken at a time when the host star showed low activity, that is, very low coverage fraction of active regions compared to the time HST/WFC3 data was taken (observed in 9/2019), then this difference in stellar activity between the two epochs could in principle explain the discrepancy between the optical and the near-infrared spectrum.

We note, however, that the raw HST/WFC3 data (Figure A.2) do not display any obvious signs of stellar activity, e.g., in form of spot-crossing events. Conversely, the VLT/ESPRESSO data (10/2019) taken at a few weeks after the TESS measurements do not show strong activity in the stellar Na and K lines. In other words, with the data at hand, there are no indications that the host star was more active in one epoch compared to the other.

⁸ <http://www.astropy.org>. Astropy is a community-developed core Python package for Astronomy (Astropy Collaboration et al. 2013; Price-Whelan et al. 2018)

⁹ The method we use allows the facula-to-spot areal ratio to drift to smaller values as a star becomes more spotted, as is observed on the Sun (Shapiro et al. 2014). See Rackham et al. (2018) for further details.

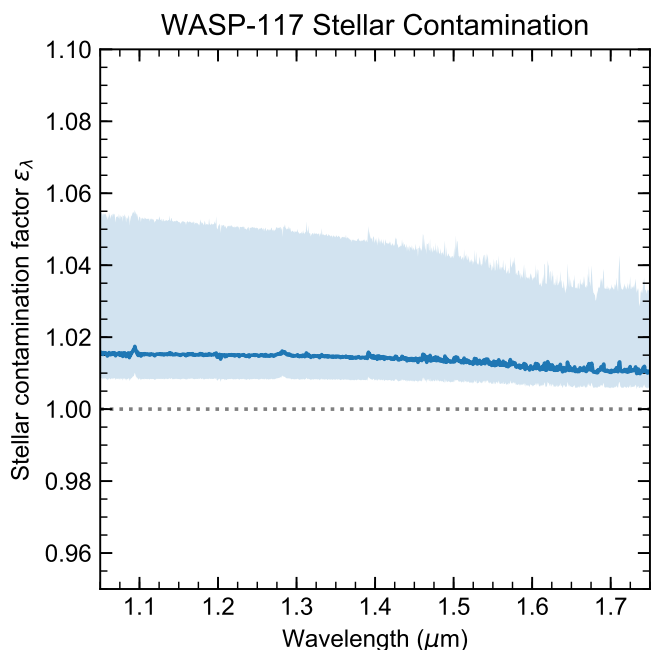


Fig. 13. Spectroscopic stellar contamination signal in the HST/WFC3 G141 bandpass produced by unocculted active regions on WASP-117. The median estimate (blue line) and 1σ confidence interval (blue shaded region) are shown.

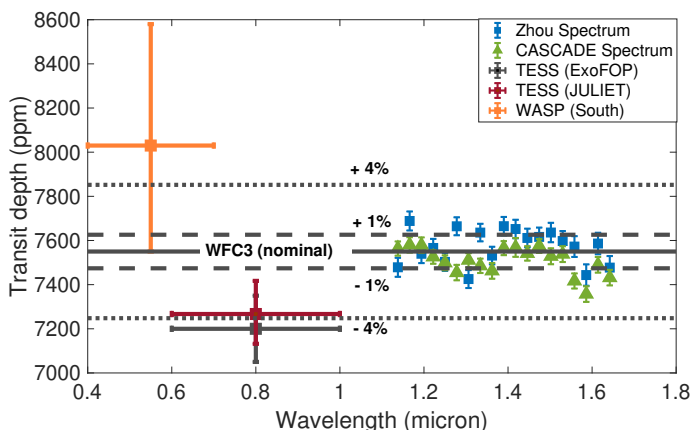


Fig. 14. HST transmission spectra from the nominal and CASCADE pipeline compared with TESS transit depth, reduced by ExoFOP, our independent re-analysis with JULIET and the WASP South transit depth. Solid grey line denotes the nominal transit depth in the WFC3 wavelength range. Dashed line and dotted lines show radius inflation/deflation by 1% and 4% respectively.

Alternatively, if the stellar activity between the two epochs did not differ drastically, unocculted bright regions (faculae) could be invoked to explain decreases in transit depths at visual wavelengths (that is, $\epsilon < 1$). We consider this unlikely, however, because the TESS band pass is redder than the wavelength where we would expect faculae to start dramatically decreasing transit depths, which is typically around $0.5 \mu\text{m}$ (Rackham et al. 2019, Fig. 5). Furthermore, the scale of the decrease is too large between the TESS and WFC3 band. The transit depth is shallower by about 4% in the TESS band (Figure 14). We expect, however, less than 1% decrease in transit depth due to the chro-

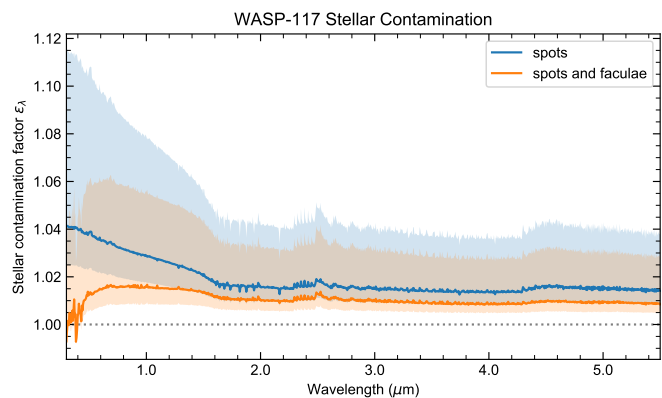


Fig. 15. Spectroscopic stellar contamination signal for $0.3\text{--}5.5 \mu\text{m}$ produced by unocculted active regions on WASP-117. The median estimates (blue line for spots and orange for spots and faculae, respectively) as well as 1σ confidence intervals (shaded regions) are shown.

maticity of bright faculae between the TESS and WFC3 G141 bands (Figure 15).

As we will show in Section 5, no atmospheric model fitted to the HST/WFC3 data yields transit depths shallower than 7400 ppm in the optical wavelength range - including the very cloudy (*Model 2*) and hazy solutions (*Model 3*). Without additional measurements, it is thus for now not possible to determine why the TESS transit depth is shallow (7200 ± 150) compared to the earlier WASP and the most recent HST/WFC3 measurements.

4. WASP-117b temperatures and chemistry composition

We could not use the TESS data to constrain atmospheric properties of WASP-117b. We further could not constrain the atmospheric temperature of WASP-117b during transit based on the muted water feature observed with HST/WFC3 (Table 3).

We still think, however, that it is worthwhile to explore exemplary chemistry models for atmospheric compositions and temperature possible for WASP-117b based on the WFC3 data and theoretical reasoning. These physically based constraints a) act as sanity checks for the simplified 1D retrieval, b) still allow us to draw further conclusions and c) inform us about the benefit of future observations.

We calculated theoretical average planetary equilibrium temperatures $T_{Pl,inst}$, assuming that the planet instantly adjusts to the stellar irradiation, that the planet is in equilibrium with the incoming stellar irradiation and that the planet experiences global heat redistribution. This is the assumption that Lendl et al. (2014) used for their analysis, using albedo $\alpha = 0$. Here, we use equation (2) in Méndez & Rivera-Valentín (2017) with $\beta = 1$ (efficient heat re-distribution over the whole planet) and broadband thermal emissivity $\epsilon = 1$, using stellar and planetary parameters from Lendl et al. (2014) and setting albedos $\alpha = 0, 0.3, 0.6$ within limits of cloud models for hot to warm Jupiters (Parmentier et al. 2016). $T_{Pl,inst}$ gives the possible range of global average temperatures, assuming instant heat adjustment, global heat circulation and different albedos for WASP-117b during one orbit, including at transit (Table 9, temperatures during transit set in bold). These temperatures were compared to the assumption that the planet's temperature is constant and equal the time-averaged planetary temperature $T_{Pl,ave}$, where we used equation (16) of

Méndez & Rivera-Valentín (2017) again with $\alpha = 0, 0.3, 0.6$. We stress that these temperatures are first order assumptions to estimate the maximum possible temperature range during transit. A more comprehensive analysis of temperature variation during one orbit requires the comparison between radiative and dynamical time scales, where the latter has to be estimated from a 3D circulation model (Lewis et al. 2014).

Table 9 shows that depending on albedo and heat adjustment assumptions, WASP-117b could assume globally averaged equilibrium temperatures T_{eq} between 700 K to 1000 K during transit. In the following, we investigated the implications of equilibrium and disequilibrium chemistry within this temperature range for *Model 1* (high metallicity $[\text{Fe}/\text{H}] > 2.2$) and *Model 2* (low metallicity $[\text{Fe}/\text{H}] < 1.75$).

We computed a self-consistent pressure-temperature profile for the exo-Saturn WASP-117b using `petitCODE` (Mollière et al. 2015, 2017) and multiple one-dimensional chemical kinetics models (Venot et al. 2012), incorporating vertical mixing and photo-chemistry. In order to systematically represent the best-fit retrieval models (see Table 3), as well as the parameter space of physically accepted solutions, we performed four base models with varying temperature and metallicity. We adopted values for atmospheric metallicities of 350 times and 5 times solar metallicity, consistent with *Model 1* and *Model 2* respectively. Further, we picked equilibrium temperatures T_{eq} of 1000 K and 700 K to represent the theoretically possible range of temperatures during transit. A C/O ratio of 0.30 is adopted in accordance with the retrievals.

We acknowledge that a C/O ratio of 0.3 may be too low, because we assumed equilibrium chemistry during retrieval. We argue, however, that higher C/O ratios produce even higher CH_4 abundances for the same pressure and temperature range (see e.g. Madhusudhan 2012). Thus, any constraints on CH_4 quenching via vertical mixing (K_{zz}) that we find for such a low C/O ratio of 0.3, will also hold for higher C/O ratios and provide e.g. a lower limit for possible K_{zz} . Therefore, we decided given the lack of other constraints that adopting C/O = 0.3 is the best approach for the time being.

Another possible concern in basing disequilibrium chemistry on retrieved parameters is the difference in planetary atmospheric temperature structure used by both models. The former uses a self-consistent 1D atmospheric temperature profile (Figure C.1, bottom right panel), based on `petitCODE` (Mollière et al. 2015, 2017), the retrieval code `petitRADTRANS` (Mollière et al. 2019) uses isothermal temperatures. However, we note that for $p \leq 10^{-3}$ bar the temperature is approximately isothermal also in the self-consistent 1D exoplanet atmosphere model. Thus, we conclude that these differences in temperature do not play a strong role here.

Furthermore, for the pressure-temperature iteration we assumed a uniform day-side heat redistribution and a moderate intrinsic temperature of 400 K, in agreement with the planet’s irradiation (Thorngren et al. 2019). Other stellar and planetary parameters were derived from Lendl et al. (2014). The pressure-temperature profiles computed with `petitCODE`, which are used in the chemical kinetics calculation, are shown in Figure 16. For the chemical kinetics model we applied a vertically constant eddy diffusion coefficient $K_{zz} = 10^{10}$ cm^2/s . We also applied photochemical reactions. To represent the spectral energy distribution of WASP-117, we have used an ATLAS stellar model ($T = 6000$ K, $\log g = 4.5$) (Castelli & Kurucz 2003) between 168 nm and 80 μm , and a time-averaged solar UV spectrum (Thuillier et al. 2004) between 1 nm and 168 nm.

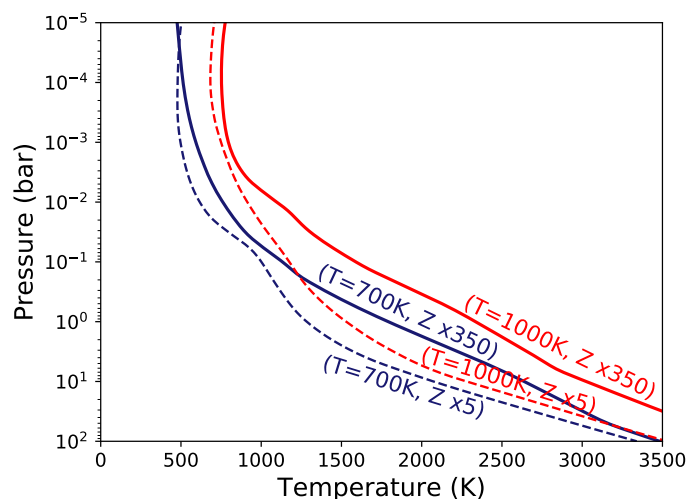


Fig. 16. Pressure-temperature profiles computed with `petitCODE` for four different scenario’s of WASP-117b: temperatures $T_{\text{eff}} = 1000$ K (red), $T_{\text{eff}} = 700$ K (blue), and metallicities $Z = Z_{\odot} \times 350$ (solid), $Z = Z_{\odot} \times 5$ (dashed). For all cases, a C/O ratio of 0.3 and intrinsic temperature of 400 K were adopted. The profiles serve as input for the chemical kinetics calculations of Figure 17.

As can be seen in Figure 17, the hot models with $T_{eq} = 1000$ K naturally have a low methane abundance in chemical equilibrium. This is exacerbated when disequilibrium chemistry is taken into account, as methane gets quenched at even lower abundances. For the warm models with $T_{eq} = 700$ K, methane starts to dominate over CO in chemical equilibrium in the higher atmospheric layers ($p < 1$ mbar for the high metallicity case and $p < 40$ mbar in the lower metallicity case). Also in these models, vertical mixing serves to reduce the methane abundance in the layers above the quenching level ($p < 100$ mbar for the high metallicity case and $p < 1$ mbar in the lower metallicity case).

For low atmospheric temperatures ($T_{eq} = 700$ K), disequilibrium chemistry through vertical mixing is required to keep a low methane abundance ($< 10^{-4}$ volume fraction) in the observable part of the atmosphere ($p < 0.1$ bar in transmission) for both, low and high atmospheric metallicity. Vertical mixing would be even stronger for lower atmospheric metallicity composition compared to high metallicity, because in the former case, more CH_4 is produced at a given pressure level. The reason for this is twofold. First, for a given equilibrium temperature the lower metallicity case results in lower atmospheric temperatures (Figure 16), leading to a higher methane abundance. Second, the lower metallicity increases the temperature of transition between CO / CH_4 (Lodders & Fegley 2002), resulting again in a higher methane abundance. Provided WASP-117b has indeed an equilibrium temperature of 700 K during transit, we could potentially further constrain $K_{zz} \geq 10^8$ cm^2/s (see Figure C.1 and Section C, where we present an abundance study for this case, as a function of K_{zz}). We note that this assessment is based on the median abundances that we retrieve for CH_4 , with 1- σ uncertainties on the upper limit of the CH_4 abundances as large as 2 orders of magnitude, see figures B.15, B.16, B.17.

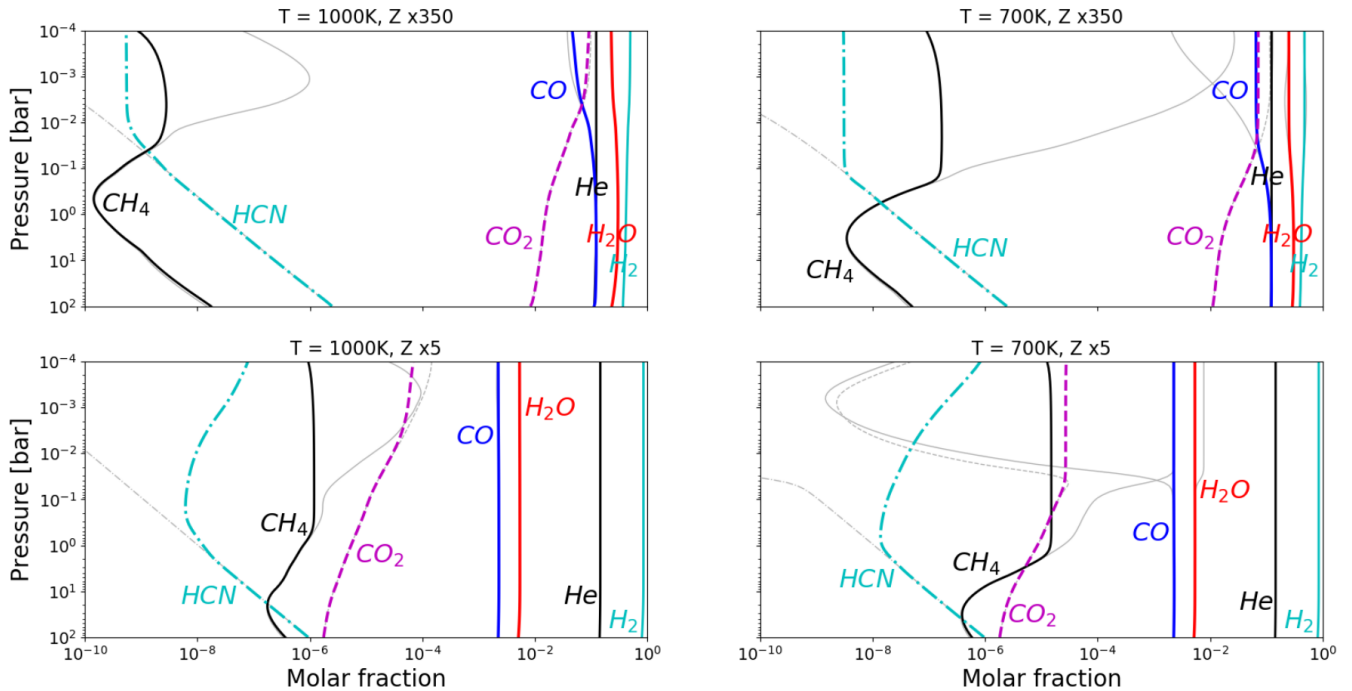
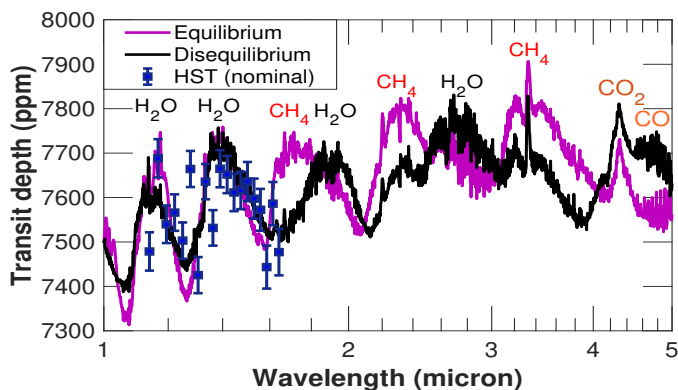
A first disequilibrium versus equilibrium model comparison in the 1–5 μm range shows that JWST data can in principle distinguish between these two scenarios (Figure 18): The absence of strong CH_4 bands, but also the presence of CO in the near infrared indicate disequilibrium chemistry.

We will investigate in the next section in more detail the prospect of JWST data to yield a tighter constraint on the

Table 9. Theoretical temperature constraints of WASP-117b during one orbit.

Time	distance ^a a [AU]	$T_{Pl,inst}$			$T_{Pl,ave}$		
		$\alpha = 0$	$\alpha = 0.3$	$\alpha = 0.6$	$\alpha = 0$	$\alpha = 0.3$	$\alpha = 0.6$
apoastron	0.1230	899	822	715			
transit	0.1168	922	844	734	1019	932	810
periastron	0.0663	1224	1120	974			
secondary eclipse	0.682	1207	1104	960			

^a based on Lendl et al. (2014)


Fig. 17. Molecular abundances computed for hot ($T_{eq} = 1000$ K) or warm ($T_{eq} = 700$ K), and very ($Z_{\odot} \times 350$) or moderately ($Z_{\odot} \times 5$) enriched atmospheres, using the chemical kinetics code of Venot et al. (2012). The colored lines denote the disequilibrium abundances for the main molecules in the planetary atmosphere. The gray lines indicate the chemical equilibrium state. A constant $K_{zz} = 10^{10}$ cm²/s and C/O = 0.3 were adopted.

Fig. 18. Prediction of molecular features in the 1 - 5 μ m wavelength range based on equilibrium (purple) and disequilibrium chemistry (black) cloud-free self-consistent forward models with methane quenching (black) for WASP-117b, assuming $T_{eq} = 700$ K and $K_{zz} = 10^8$ cm²/s and $Z = Z_{\odot} \times 5$.

CH_4 abundances, atmospheric temperatures and disequilibrium chemistry in WASP-117b.

5. Prospects for future investigations with HST and JWST

We investigated to what extent future observations with HST in the UV and optical, and JWST in the near to mid-infrared could constrain the properties of WASP-117b.

Synthetic spectra based on the results of *Model 1* (high metallicity), *Model 2* (low metallicity & cloudy) and *Model 3* (hazy) (see Section 3.3, Table 3) are shown in Figure 19.

The possible atmospheric compositions retrieved for WASP-117b produce large differences in wavelength ranges between 0.3 – 0.5 μ m (Figure 19, top panels). An accuracy of 200 ppm could already be sufficient to distinguish between very hazy (extreme hazy solutions of *Model 3*, based on the CASCADE spectrum) and clear sky, heavy metal atmospheric composition (*Model 1*), based on the HST/WFC3 G141 grism spectrum reduced with the CASCADE pipeline (Figure 19, top right). Accuracy of 100 ppm and better would be needed between 0.3 and 0.5 μ m to distinguish between the medians of the clear sky, heavy metal, the grey cloudy solutions with lower metal-content and the hazy solutions, irrespective of data pipeline used (Figure 19, top panels).

Wakeford et al. (2020) recently showed that it is, in principle, possible to accurately measure a transmission spectrum of a

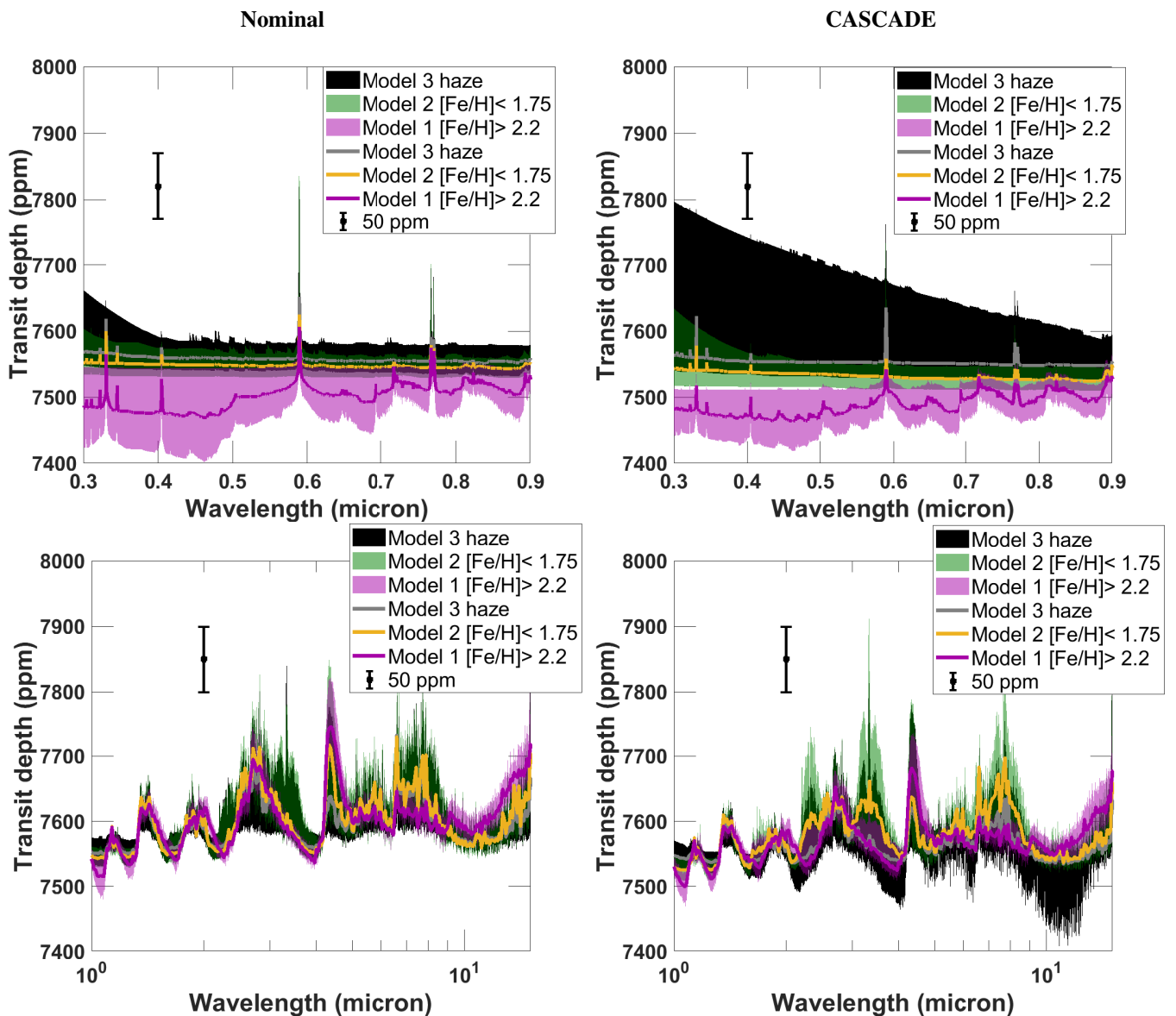


Fig. 19. Synthetic spectra based on *Model 1* (high metallicity, purple), *Model 2* (low metallicity & cloudy, green) and *Model 3* (haze, black) based on the WASP-117b spectrum reduced with the nominal pipeline (left panels), and the CASCADE pipeline (right panels). Colored areas give the 1σ envelope for the solutions for each model. Solid lines in grey, yellow and light-pink give the best fit for *Model 1*, *Model 2* and *Model 3*, respectively. The spectra are shown for the wavelength range: 0.3 - 0.9 μm (upper panels) and 1 - 15 μm (lower panels). In addition, a hypothetical data point with 50 ppm accuracy is shown for guidance.

transiting exoplanet in this wavelength range using WFC3/UVIS G280 grism. The authors report an accuracy of 29 to 33 ppm for the broad band depth between 0.3 to 0.8 μm and 200 ppm in 10 nm spectroscopic bins. Wakeford et al. (2020) observed two transits of the hot Jupiter HAT-P-41b around a quiet F star with magnitude $m_V = 11.08$. Our target WASP-117b likewise orbits a quiet F star that is even brighter than the host star of HAT-P-42b. WASP-117 has a magnitude of $m_V = 10.15$.

Thus, we estimate that two transit observations of WASP-117b could be sufficient to constrain a haze layer and potentially also the atmospheric metallicity using WFC3/UVIS. We did not consider here the optical transits in particular the TESS transit depth 7200 ± 150 ppm. All synthetic spectra have transit depths larger than 7400 ppm in the 0.8-1 μm range and do not fit within 1σ the TESS data (see Section 3.6).

In the JWST wavelength range with a single transit in each instrument, we expect clear H_2O features for the exo-Saturn

WASP-117b in the JWST wavelength range (Figure 19, bottom panels). Furthermore, some models with low metallicity solutions (*Model 2* and *Model 3* framework) yield ~ 100 ppm strong CH_4 features at 3.4 μm . For example, the best fit model for *Model 2* based on the CASCADE spectrum predicts a clear CH_4 signal at 3.4 μm (Figure 19, bottom, left panel). This would correspond to a CH_4 abundance of 1.8×10^{-5} volume fraction (Table 3).

Observing WASP-117b with JWST/NIRSpec should thus at the very least impose constraints on the CH_4 and H_2O content in the atmosphere. Observations of relatively high CH_4 abundances of 10^{-5} volume fraction could also disprove high metallicity via chemistry constraints as shown in Section 4 (Figure 17). Non-observations of CH_4 could, on the other hand, indicate either high metallicity, high atmospheric equilibrium temperatures ($T_{eq} \gtrsim 1000$ K) during transit, or disequilibrium chemistry. In the latter case, we could also constrain vertical mixing (K_{zz}). It is

also evident from Figure 19 that CO₂ is a useful probe of metallicity, with the high metallicity cases showing increased CO₂ absorption at 4.3 μm and at the red edge of the spectra, towards 15 μm.

Taking into account the expected instrument performance confirms our statement that NIRSpec should be capable, even with one single transit observation of WASP-117b, to resolve differences in CO₂ at 4.3 μm (NIRSpec/G385M) that are due to different metallicity assumptions in between atmospheric models (Figure 20) as well as constrain CH₄ at both, 2.3 and 3.4 μm (NIRSpec/G235M). This is readily apparent in Figure 20, right panel for CASCADE Model 2 (green) with enhanced CH₄ content compared to other retrieved models (see Table 3).

The comparison between spectra derived from the nominal and CASCADE pipelines (Figure 20 left and right panel, respectively) also shows that the nominal H₂O features in the NIRSpec/G235M wavelength range are in the former case significantly enhanced compared to the latter, regardless of which underlying model is used. The differences in depth of the water absorption is mainly due to the differences in atmospheric temperatures assumed in the model medians. Models retrieved from the nominal HST/WFC3 spectrum are unconstrained in temperature within the prior range of 500–1500 K, so that the median model assumes 1000 K, whereas models retrieving the CASCADE HST/WFC3 spectrum retrieve lower median temperature of 800 K and cooler (Table 3).

The simultaneous measurement of H₂O, CH₄, CO and CO₂ with JWST thus promises to improve the constraint of the C/O ratio of the planetary atmosphere and thus either confirm or disprove the sub-solar C/O ratio that we tend to find for WASP-117b. JWST will further be extremely important to constrain temperature, metallicity, CH₄ content and thus methane chemistry in the exo-Saturn WASP-117b during transit. HST/UVIS observations will be more important to constrain hazes and cloudiness, which could also constrain atmospheric metallicity if an accuracy of 100 ppm or better is reached between 0.3 and 0.6 μm.

6. Discussion

This work shows that it is possible but also very challenging to investigate the atmospheric properties of a warm gas planet with an orbital period of 10 days and longer. The longer the orbital period, the longer the transit duration that needs to be captured in its entirety to perform accurate transmission spectroscopy. For WASP-117b, the total transit duration was six hours, and a further 1–2 hours of out-of-transit observations before and after transit were needed for calibration. Thus, a relatively large time investment was needed to obtain accurate transit spectroscopy with one single transit with HST (11 consecutive orbits) and VLT/ESPRESSO (10 hour continuous observation), respectively. We also note that, in 2018, there were only two occasions to capture the full transit with VLT in its entirety from the ground. Otherwise, only partial transits were observable at night.

Atmosphere retrieval for WASP-117b favors, based on Bayesian analysis alone, a high metallicity ([Fe/H] > 2.2), clear atmospheric composition (*Model 1*) “substantially” ($B > 4$) over the cloudy, lower metallicity solution (*Model 2*) as fit to the detected 3σ water spectrum. See Section 3.4 for an overview of the statistical evidence for the different models. We caution, however, against using Bayesian analysis of the HST/WFC3 data alone to rule out cloudy, lower metallicity solutions, completely. We also caution that patchy clouds could mimick a high

metallicity composition (Line & Parmentier 2016). We also note that Anisman et al. (2020) retrieved atmospheric properties of WASP-117b based on the same HST data with their own pipeline. While these authors confirm the H₂O detection, they can not place constraints on atmospheric metallicity or CH₄ abundances.

VLT/ESPRESSO observations of WASP-117b in the optical could not be used to constrain the atmospheric properties of WASP-117b further. The planetary Na and K signal is too small (2.4σ). Thus, we conclude that exoplanets with long orbital periods should only be observed with ground based telescopes, after space based observations have yielded first constraints on the cloud coverage and thus the feasibility of obtaining a strong enough planetary signal in the optical.

TESS data could also not be used for atmospheric constraints, because the TESS transit depth is abnormally shallow. We find that the TESS data is inconsistent with all atmospheric models that we explored, including cloudy and haze atmosphere models (Section 5). Stellar activity is also unlikely to cause a 4% transit depth differences between the TESS and the WFC3/NIR wavelength range (Figure 14). This example shows, however, how difficult it can be to combine measurements taken at two different epochs in two different wavelengths, even when the respective atmospheric measurements are precise and the host star is quiet (Rackham et al. 2019).

We maintain that a better constraint of the metallicity in the atmosphere of the eccentric WASP-117b is warranted as its properties would be complementary to other exoplanets on circular orbits in the same mass range: A clear sky, high metallicity atmospheric composition would place WASP-117b significantly outside of the mass-metallicity relation inferred from the Solar System¹⁰

Further, it is unclear in how far erosion processes have influenced the atmospheric metallicity of extrasolar Neptune and Saturn-mass exoplanets (see e.g. Owen & Lai 2018; dos Santos et al. 2019; Armstrong et al. 2020). Also, here the atmospheric properties of the eccentric WASP-117b could be illuminating. Figure 21, right panel, shows that WASP-39b and WASP-107b lie in the Neptune¹¹ desert (Mazeh et al. 2016), which is thought to reflect significant mass loss in this planetary mass and orbital period regime. The Super-Neptune WASP-107b was indeed found to experience loss of helium (Spake et al. 2018; Kirk et al. 2020) that could modify atmospheric metallicity over time. The exo-Saturn WASP-117b, on the other hand, should lie at 0.1168 AU at least during transit well outside of the Neptune desert. The large distance during transit also explains the absence of deep Na and K features in the VLT/ESPRESSO data during transit. The atmospheric metallicity of WASP-117b could thus

¹⁰ The values for the Solar System bodies come with the caveat that even there the inferred metallicity depend on uncertainties like core size and H₂O content (Thorngren & Fortney 2019). (Figure 21, left panel). The exo-Saturn WASP-117b would thus join ranks with planets like WASP-39b with comparatively high metallicity (Wakeford et al. 2018), and HAT-P-11b (Chachan et al. 2019), which also do not follow the Solar System mass-metallicity relation. In fact, a high atmospheric metallicity and its mass and radius would make WASP-117b very similar to WASP-39b. A cloudy, lower atmospheric metallicity composition (*Model 2*), on the other hand, would make WASP-117b more comparable to WASP-107b, WASP-43b and WASP-12b that all follow the inferred Solar System mass-metallicity correlation (see also Thorngren & Fortney 2019).

¹¹ One could also call it the sub-Jovian desert (Owen & Lai 2018) as the mass range of planets affected by photoevaporation is not strictly constrained to Neptune mass.

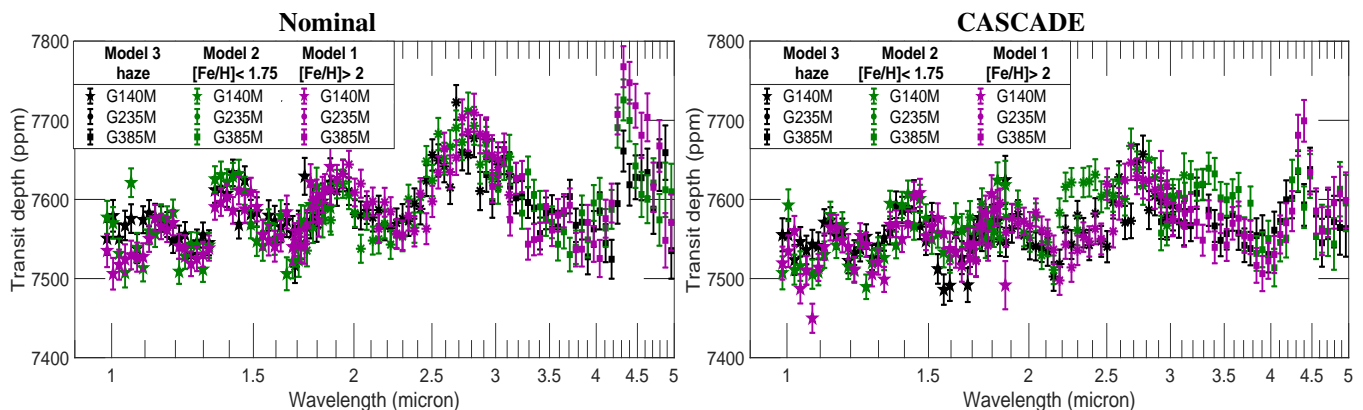


Fig. 20. Predicted JWST/NIRSpec observations in the 0.8 - 5 μm wavelength range based on the median of *Model 1* (high metallicity, black), *Model 2* (low metallicity & cloudy, green) and *Model 3* (haze, purple) based on the WASP-117b spectrum reduced with the nominal pipeline (left panel), and the CASCADE pipeline (right panel). The model with estimated instrument performance was generated by *PandExo* (Batalha et al. 2017), assuming observation of a single transit with resolution $R \sim 30$. Hexagons, stars and squares denote simulated NIRSpec G140M, G235M and G385M data, respectively.

shed light on if a high metallicity atmospheric composition (if confirmed) is a sign of atmospheric erosion processes or instead of formation processes different from the Solar System.

The atmosphere of WASP-117b could also be illustrative for the study of disequilibrium processes. We found consistently low CH_4 abundances ($< 10^{-4}$ volume fraction), expressed by our retrievals finding sub-solar C/O ratios. Interpreting the atmospheric chemistry in more detail requires, however, the additional knowledge of the atmospheric temperature, which we could not constrain within prescribed limits of 500 to 1500 K based on the WFC3 data alone.

We maintain, however, based on simple equilibrium temperatures calculations using Méndez & Rivera-Valentín (2017) that temperatures between 700 and 1000 K are physical during the transit of the eccentric exo-Saturn WASP-117b (Section 4, Table 9). Chemical modelling for 700 K and 1000 K for high ($350\times$ solar) and low metallicities ($5\times$ solar) further confirm that very low CH_4 abundances in WASP-117b during transit are physically plausible. The 700 K models require disequilibrium chemistry to keep atmospheric CH_4 abundances below 10^{-4} volume fraction at $p = 10^{-4}$ bar, which we identified to first order as the main region that is probed during transmission. For the colder temperature models, we thus infer a vertical eddy diffusion coefficient of $K_{zz} \geq 10^8 \text{ cm}^2/\text{s}$ to explain absence of methane via CH_4 quenching.

The eddy diffusion coefficient K_{zz} is not trivially constrained for irradiated exoplanet atmospheres. Since these atmospheres tend to have deep, stably stratified radiative zones, the quenching point of most species typically does not lie within the (deeper) convective zone, and the traditional mixing-length theory breaks down. Instead, vertical mixing in irradiated exoplanets is described as being caused by medium- to large-scale atmospheric circulation, which – when globally averaged – may or may not act as a diffusive process (see e.g. recent discussions in Zhang 2020; Showman et al. 2020). It is possible to study these atmospheric motions in 3D using general circulation models, and from these, derive order-of-magnitude parametrizations for the 1D eddy diffusion coefficient K_{zz} . For instance, for the hot Jupiter HD 209458b $K_{zz} = 5 \cdot 10^8 \text{ cm}^2/\text{s} - 10^9 \text{ cm}^2/\text{s}$ is derived at 1 bar (Parmentier et al. 2013; Menou 2019). We note that WASP-117b is cooler than HD 209458b, and K_{zz} should decrease with decreasing equilibrium temperature (Komacek et al. 2019). However, atmospheres with higher metallicities, as we in-

fer for WASP-117b, are also expected to have more vertical mixing than lower-metallicity atmospheres (Charnay et al. 2015). Our tentative inference of $K_{zz} \geq 10^8 \text{ cm}^2/\text{s}$ for the ($T_{\text{eq}} = 700 \text{ K}$)-model thus shows reasonable agreement with theoretically motivated expectations. However, a more sophisticated 3D model would be needed to further strengthen the agreement.

We argue that additional transit measurements of WASP-117b with HST/UVIS and the G280 grism could yield the necessary accuracy (200-100 ppm, (Wakeford et al. 2020)) to constrain a haze and cloud layer in WASP-117b. A low resolution transmission spectrum in that range would reveal cloud properties due to the different scattering slopes between 0.3 and 0.5 μm for a clear atmosphere with high metallicity, a grey cloudy and hazy atmosphere with low metallicity (Figure 5, upper panels). HST/UVIS measurements would thus already constrain atmospheric metallicity, which is degenerate with cloud properties in the HST/WFC3 range. In addition, HST/UVIS data could also potentially shed light on the origin of the shallow TESS transit depth. Such data would also warrant the use of a patchy cloud model (Line & Parmentier 2016).

Additional measurements with JWST/NIRSpec observations in the 0.8-5 micron region could further constrain CH_4 to at least $\leq 1.8 \times 10^{-5}$ volume fraction by observing in the 3.4 μm CH_4 band. A further constraint on CH_4 but also on CO at 4.7 μm would improve our understanding of atmosphere chemistry in WASP-117b, in particular, in conjunction with secondary eclipse observations to constrain temperature variations of WASP-117b during one orbit. The presence and absence of CH_4 , or CO_2 at 4.3 micron would also constrain atmospheric metallicity and together with H_2O features confirm if WASP-117b indeed has a subsolar C/O ratio. See also Guzmán Mesa et al. (2020) for the capabilities to use JWST/NIRSpec to characterize the atmospheric chemistry of warm Neptunes.

7. Conclusions

We detected a 3σ water spectrum in the HST/WFC3 near-infrared transmission spectrum of WASP-117b. Comparison to one-dimensional atmospheric models assuming vertical isothermal temperatures, a uniform grey cloud coverage and equilibrium chemistry (*petitRADTRANS*) shows that the water absorption is less pronounced than expected with a solar-type metallicity composition. Based on the preferences derived from the

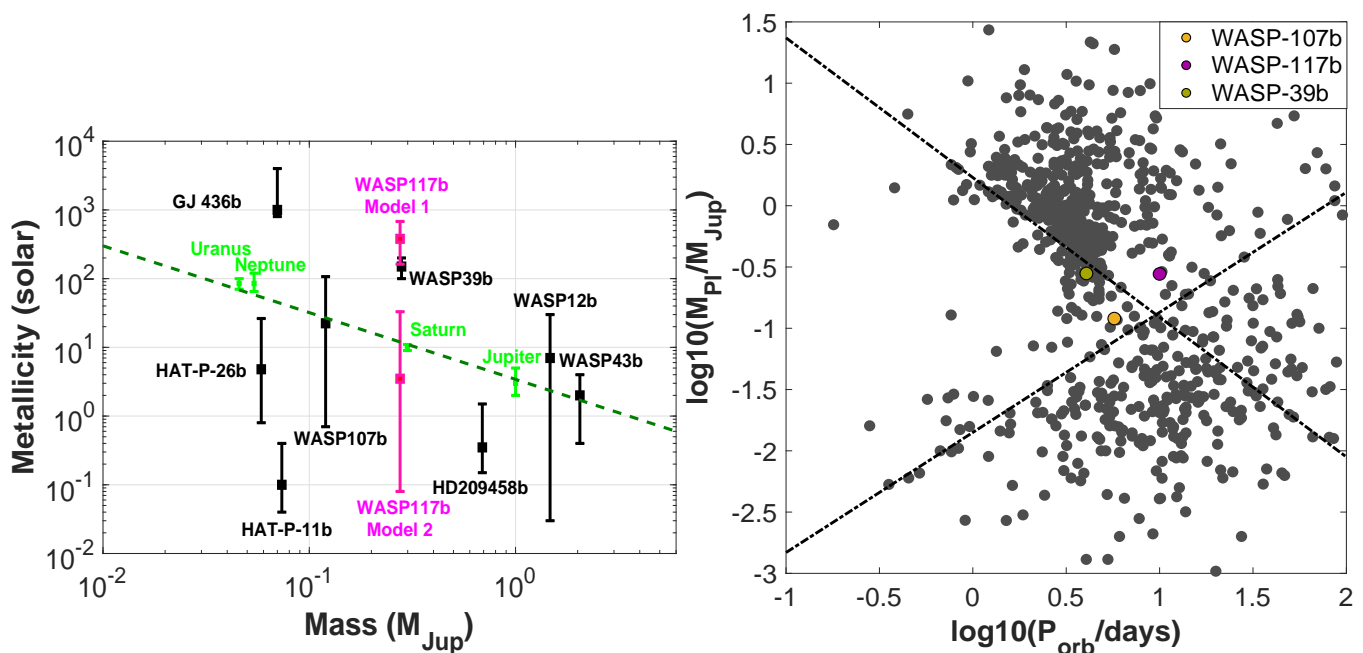


Fig. 21. Left: Metallicity content derived for several exoplanets, adapted from Chachan et al. (2019). WASP-117b is mainly comparable in mass and metallicity to WASP-107b (Kreidberg et al. 2018) and WASP-39b (Wakeford et al. 2018). Solar System values are from Wong et al. (e.g. 2004); Helled & Guillot (e.g. 2018); Chachan et al. (e.g. 2019); Movshovitz et al. (e.g. 2020)

Right: All transiting planets with orbital periods shorter than 100 days and the Neptune desert limits as proposed by Mazeh et al. (2016). WASP-39b and WASP-107b lie clearly inside the Neptune desert and are thus probably subject to erosion processes. WASP-117b lies outside the Neptune desert. (Derived from exoplanets.eu on 30.3.2020)

Bayes factor analysis alone, WASP-117b appears to have a high atmospheric metallicity ($[\text{Fe}/\text{H}] = 2.58_{-0.37}^{+0.26}$ or 380_{-217}^{+311} solar, based on the nominal pipeline) with relatively clear skies. We cannot rule, however, lower atmospheric metallicity ($[\text{Fe}/\text{H}] < 1.75$) with clouds and potentially an additional haze layer. However, we conclude that the data quality is too limited to warrant the application of a hazy atmosphere layer. The high metallicities that are strongly preferred by a Bayesian factor analysis are comparable to similarly high atmospheric metallicities (151_{-48}^{+46} solar) found in WASP-39b, an exo-Saturn on a circular 4 days orbit around a cooler G type star (Wakeford et al. 2018).

While the basic atmospheric composition could be constrained, the temperature of WASP-117b during transit is unconstrained between 500–1500 K. Thus, we can not identify if the planet changes temperature during its eccentric 10 days orbit. Based on basic energy balance equations and realistic range of heat redistribution scenarios, we estimate that the planet could theoretically adopt equilibrium temperatures between 700 K and 1000 K, depending on albedo and heat adjustment.

Because the temperature of WASP-117b during transit is not constrained, we cannot further test multiple possible hypotheses that may explain the low abundance of CH_4 in the atmosphere of WASP-117b during transit. If the atmospheric temperature is above 1000 K, then CH_4 can not form and we do not expect to detect measurable levels of CH_4 . If the temperature of WASP-117b is during transit 700 K, then higher CH_4 abundances than 10^{-4} volume fraction would form in the atmospheric levels that we probe ($p < 10^{-4}$ bar), assuming equilibrium chemistry. Thus, in the latter case, we would need to invoke CH_4 quenching and we could constrain the eddy diffusion coefficient to $K_{zz} \geq 10^8 \text{ cm}^2/\text{s}$. If WASP-117b is cool, it would thus show methane-quenching like indicated for the super-Neptune WASP-107b (Kreidberg et al. 2018).

Using VLT/ESPRESSO data alone, we do not find strong indications for Na and K within 3σ . In combination with HST/WFC3 data, however, we still find “substantial” (2.4σ) preference for the presence of Na and K.

We also compared our WFC3 spectrum to TESS broad band observations of WASP-117b and found that the TESS transit depth is 4% shallower than the HST/WFC3 transit depth. We can not explain this difference with either systematic noise, stellar activity or clouds.

Furthermore, with the new VLT/ESPRESSO data, we improved via the Rossiter-MacLaughlin effect measurements of the $v \sin i$ of the star and the projected spin-orbit angle to $1.46 \pm 0.14 \text{ km/s}$ and $-46.9_{-4.8}^{+5.5} \text{ deg}$, respectively.

8. Outlook

WASP-117b is one of the first warm eccentric exo-Saturns with a long orbital period (10 days), the atmosphere of which was characterized. While the observations proved to be challenging, they indicate that WASP-117b could have interesting properties such that further observations with JWST and HST in the optical range would be warranted.

WASP-117b could be an ideal target to investigate how (disequilibrium) chemistry processes are controlled by precisely known, varying heating conditions on a 10 days orbit around a quiet F main sequence star. This studies would complement studies of eccentric exoplanets on tighter orbits (e.g. Lewis et al. 2013, 2014; Agúndez et al. 2014). WASP-117b is also a complementary observation target to the super-Neptunes WASP-107b and WASP-39b on circular, tighter orbits to aid our understanding on how erosion processes shape atmospheric properties such as metallicities in the Neptune-to-Saturn mass range.

As of now, several promising extrasolar exo-Saturns on eccentric orbits with $P_{\text{orb}} \geq 10$ days around bright stars suitable for

in-depth atmospheric characterization are known (Brahm et al. 2016, 2018; Jordán et al. 2019; Brahm et al. 2019; Rodriguez et al. 2019). One such planet, K2-287 b, orbits a G-type star with a time-averaged equilibrium temperature of 800 K (Jordán et al. 2019), that is, it is at least 200 K cooler than WASP-117b would thus be even more ideal to study disequilibrium chemistry in warm eccentric gas planets on relatively wide orbits.

Acknowledgements. L.C. acknowledges support by the DLR grant 50OR1804 and DFG grant CA 1795/3. F. Y. acknowledges the support of the DFG priority program SPP 1992 "Exploring the Diversity of Extrasolar Planets (RE 1664/16-1)". RB is a Ph.D. fellow of the Research Foundation–Flanders (FWO). P.M. and Th.H. acknowledge support from the European Research Council under the European Union's Horizon 2020 research and innovation program under grant agreement No. 832428. B.V.R. thanks the Heising-Simons Foundation for support. A.J. acknowledges support from FONDECYT project 1171208 and by the Ministry for the Economy, Development, and Tourism's Programa Iniciativa Científica Milenio through grant IC 120009, awarded to the Millennium Institute of Astrophysics (MAS). Support for Programs number GO-15301 and AR-15060 were provided by NASA through a grant from the Space Telescope Science Institute, which is operated by the Association of Universities for Research in Astronomy, Incorporated, under NASA contract NAS5-26555. O.V. thanks the CNRS/INSU Programme National de Planétologie (PNP) and CNES for funding support. J.B. acknowledges support from the European Research Council under the European Union's Horizon 2020 research and innovation program Exoplanets-A under grant agreement No. 776403. We would also like to thank the reviewer Bruno Bézard for his thoughtful and thorough review which greatly improved this paper.

References

- Agúndez, M., Venot, O., Selsis, F., & Iro, N. 2014, *ApJ*, 781, 68
- Anisman, L. O., Edwards, B., Changeat, Q., et al. 2020, arXiv e-prints, arXiv:2009.08916
- Apai, D., Karalidi, T., Marley, M. S., et al. 2017, *Science*, 357, 683
- Armstrong, D. J., Lopez, T. A., Adibekyan, V., et al. 2020, arXiv e-prints, arXiv:2003.10314
- Asplund, M., Grevesse, N., Sauval, A. J., & Scott, P. 2009, *ARA&A*, 47, 481
- Astropy Collaboration, Robitaille, T. P., Tollerud, E. J., et al. 2013, *A&A*, 558, A33
- Barman, T. S., Macintosh, B., Konopacky, Q. M., & Marois, C. 2011a, *ApJ*, 733, 65
- Barman, T. S., Macintosh, B., Konopacky, Q. M., & Marois, C. 2011b, *ApJ*, 735, L39
- Barstow, J. K. 2020, arXiv e-prints, arXiv:2002.02945
- Barstow, J. K., Aigrain, S., Irwin, P. G. J., et al. 2013, *MNRAS*, 430, 1188
- Batalha, N. E., Mandell, A., Pontoppidan, K., et al. 2017, *PASP*, 129, 064501
- Benneke, B., Knutson, H. A., Lothringer, J., et al. 2019, *Nature Astronomy*, 3, 813
- Benneke, B. & Seager, S. 2013, *ApJ*, 778, 153
- Brahm, R., Espinoza, N., Jordán, A., et al. 2019, *AJ*, 158, 45
- Brahm, R., Espinoza, N., Jordán, A., et al. 2018, *MNRAS*, 477, 2572
- Brahm, R., Jordán, A., Bakos, G. Á., et al. 2016, *AJ*, 151, 89
- Brammer, G., Ryan, R., & Pirzkal, N. 2015, Source-dependent master sky images for the WFC3/IR grisms, Space Telescope WFC Instrument Science Report
- Buchner, J. 2014, arXiv e-prints, arXiv:1407.5459
- Caldas, A., Leconte, J., Selsis, F., et al. 2019, *A&A*, 623, A161
- Carnall, A. C. 2017, arXiv e-prints, arXiv:1705.05165
- Castelli, F. & Kurucz, R. L. 2003, in *IAU Symposium*, Vol. 210, Modelling of Stellar Atmospheres, ed. N. Piskunov, W. W. Weiss, & D. F. Gray, A20
- Chachan, Y., Knutson, H. A., Gao, P., et al. 2019, *AJ*, 158, 244
- Charnay, B., Meadows, V., & Leconte, J. 2015, *ApJ*, 813, 15
- Crossfield, I. J. M. 2015, *PASP*, 127, 941
- Czesla, S., Klocová, T., Khalafinejad, S., Wolter, U., & Schmitt, J. H. M. M. 2015, *A&A*, 582, A51
- Czesla, S., Schröter, S., Schneider, C. P., et al. 2019, PyA: Python astronomy-related packages
- Deming, D., Knutson, H., Kammer, J., et al. 2015, *ApJ*, 805, 132
- Deming, D., Wilkins, A., McCullough, P., et al. 2013, *ApJ*, 774, 95
- dos Santos, L. A., Ehrenreich, D., Bourrier, V., et al. 2019, *A&A*, 629, A47
- Espinoza, N. 2018, *Research Notes of the American Astronomical Society*, 2, 209
- Espinoza, N., Kossakowski, D., & Brahm, R. 2019, *MNRAS*, 490, 2262
- Foreman-Mackey, D., Hogg, D. W., Lang, D., & Goodman, J. 2013, *PASP*, 125, 306
- Golub, G. H., Heath, M., & Wahba, G. 1979, *Technometrics*, 21, 215
- Guilluy, G., Sozzetti, A., Brogi, M., et al. 2019, *A&A*, 625, A107
- Guzmán Mesa, A., Kitzmann, D., Fisher, C., et al. 2020, arXiv e-prints, arXiv:2004.10106
- Helled, R. & Guillot, T. 2018, Internal Structure of Giant and Icy Planets: Importance of Heavy Elements and Mixing, 44
- Hoerl, A. E. & Kennard, R. W. 1970, *Technometrics*, 12, 55
- Horne, K. 1986, *PASP*, 98, 609
- Janson, M., Brandt, T. D., Kuzuhara, M., et al. 2013, *ApJ*, 778, L4
- Jordán, A., Brahm, R., Espinoza, N., et al. 2019, *AJ*, 157, 100
- Jordán, A., Brahm, R., Espinoza, N., et al. 2020, *AJ*, 159, 145
- Kass, R. E. & Raftery, A. E. 1995, *Journal of the American Statistical Association*, 90, 773
- Kipping, D. M. 2013, *MNRAS*, 435, 2152
- Kirk, J., Alam, M. K., López-Morales, M., & Zeng, L. 2020, *AJ*, 159, 115
- Kochanek, C. S., Shappee, B. J., Stanek, K. Z., et al. 2017, *PASP*, 129, 104502
- Komacek, T. D., Showman, A. P., & Parmentier, V. 2019, *ApJ*, 881, 152
- Kreidberg, L. 2015, *PASP*, 127, 1161
- Kreidberg, L., Bean, J. L., Désert, J.-M., et al. 2014, *ApJ*, 793, L27
- Kreidberg, L., Line, M. R., Thorngren, D., Morley, C. V., & Stevenson, K. B. 2018, *ApJ*, 858, L6
- Kurucz, R. L. 1993, *Astronomical Society of the Pacific Conference Series*, Vol. 44, A New Opacity-Sampling Model Atmosphere Program for Arbitrary Abundances, ed. M. M. Dworetsky, F. Castelli, & R. Faraggiana, 87
- Lendl, M., Triaud, A. H. M. J., Anderson, D. R., et al. 2014, *A&A*, 568, A81
- Lewis, N. K., Knutson, H. A., Showman, A. P., et al. 2013, *ApJ*, 766, 95
- Lewis, N. K., Showman, A. P., Fortney, J. J., Knutson, H. A., & Marley, M. S. 2014, *ApJ*, 795, 150
- Line, M. R. & Parmentier, V. 2016, *ApJ*, 820, 78
- Lodders, K. & Fegley, B. 2002, *Icarus*, 155, 393
- Lomb, N. R. 1976, *Ap&SS*, 39, 447
- Luger, R., Agol, E., Kruse, E., et al. 2016, *AJ*, 152, 100
- MacDonald, R. J., Goyal, J. M., & Lewis, N. K. 2020, arXiv e-prints, arXiv:2003.11548
- MacDonald, R. J. & Madhusudhan, N. 2017, *MNRAS*, 469, 1979
- Madhusudhan, N. 2012, *ApJ*, 758, 36
- Mallonn, M., von Essen, C., Herrero, E., et al. 2019, *A&A*, 622, A81
- Mazeh, T., Holczer, T., & Faigler, S. 2016, *A&A*, 589, A75
- Méndez, A. & Rivera-Valentín, E. G. 2017, *ApJ*, 837, L1
- Menou, K. 2019, *MNRAS*, 485, L98
- Miles, B. E., Skemer, A. J., Barman, T. S., Allers, K. N., & Stone, J. M. 2018, *ApJ*, 869, 18
- Mollière, P., van Boekel, R., Bouwman, J., et al. 2017, *A&A*, 600, A10
- Mollière, P., van Boekel, R., Dullemond, C., Henning, T., & Mordasini, C. 2015, *ApJ*, 813, 47
- Mollière, P., Wardenier, J. P., van Boekel, R., et al. 2019, *A&A*, 627, A67
- Moses, J. I., Marley, M. S., Zahnle, K., et al. 2016, *ApJ*, 829, 66
- Movshovitz, N., Fortney, J. J., Mankovich, C., Thorngren, D., & Helled, R. 2020, *ApJ*, 891, 109
- Nagao, M. & Matsuyama, T. 1979, *Computer Graphics and Image Processing*, 9, 394
- Owen, J. E. & Lai, D. 2018, *MNRAS*, 479, 5012
- Parmentier, V., Fortney, J. J., Showman, A. P., Morley, C., & Marley, M. S. 2016, *ApJ*, 828, 22
- Parmentier, V., Showman, A. P., & Lian, Y. 2013, *A&A*, 558, A91
- Pepe, F. A., Cristiani, S., Rebolo Lopez, R., et al. 2010, *Society of Photo-Optical Instrumentation Engineers (SPIE) Conference Series*, Vol. 7735, ESPRESSO: the Echelle spectrograph for rocky exoplanets and stable spectroscopic observations, 77350F
- Pinhas, A. & Madhusudhan, N. 2017, *MNRAS*, 471, 4355
- Pirzkal, N., Ryan, R., & Brammer, G. 2016, Trace and Wavelength Calibrations of the WFC3 G102 and G141 IR Grisms, Space Telescope WFC Instrument Science Report
- Piskunov, N. & Valenti, J. A. 2017, *A&A*, 597, A16
- Pluriel, W., Zingales, T., Leconte, J., & Parmentier, V. 2020, arXiv e-prints, arXiv:2003.05943
- Price-Whelan, A. M., Sipőcz, B. M., Günther, H. M., et al. 2018, *AJ*, 156, 123
- Queloz, D., Eggenberger, A., Mayor, M., et al. 2000, *A&A*, 359, L13
- Rackham, B. V., Apai, D., & Giampapa, M. S. 2018, *ApJ*, 853, 122
- Rackham, B. V., Apai, D., & Giampapa, M. S. 2019, *AJ*, 157, 96
- Rocchetto, M., Waldmann, I. P., Venot, O., Lagage, P. O., & Tinetti, G. 2016, *ApJ*, 833, 120
- Rodriguez, J. E., Quinn, S. N., Huang, C. X., et al. 2019, *AJ*, 157, 191
- Samland, M., Bouwman, J., Hogg, D. W., Brandner, W., & Henning, T. 2020, *A&A*
- Scargle, J. D. 1982, *ApJ*, 263, 835
- Schölkopf, B., Hogg, D. W., Wang, D., et al. 2016, *Proceedings of the National Academy of Sciences*, 113, 7391
- Shapiro, A. I., Solanki, S. K., Krivova, N. A., et al. 2014, *A&A*, 569, A38
- Shappee, B. J., Prieto, J. L., Grupe, D., et al. 2014, *ApJ*, 788, 48

- Showman, A. P., Lewis, N. K., & Fortney, J. J. 2014, arXiv e-prints, arXiv:1411.4731
- Showman, A. P., Tan, X., & Parmentier, V. 2020, arXiv e-prints, arXiv:2007.15363
- Showman, A. P., Tan, X., & Zhang, X. 2019, ApJ, 883, 4
- Spake, J. J., Sing, D. K., Evans, T. M., et al. 2018, Nature, 557, 68
- Thorngren, D. & Fortney, J. J. 2019, ApJ, 874, L31
- Thorngren, D., Gao, P., & Fortney, J. J. 2019, ApJ, 884, L6
- Thuillier, G., Floyd, L., Woods, T. N., et al. 2004, Advances in Space Research, 34, 256
- Trotta, R. 2008, Contemporary Physics, 49, 71
- van der Walt, S., Schönberger, J. L., Nunez-Iglesias, J., et al. 2014, PeerJ, 2, e453
- Venot, O., Hébrard, E., Agúndez, M., et al. 2012, A&A, 546, A43
- Wakeford, H. R., Sing, D. K., Deming, D., et al. 2018, AJ, 155, 29
- Wakeford, H. R., Sing, D. K., Kataria, T., et al. 2017, Science, 356, 628
- Wakeford, H. R., Sing, D. K., Stevenson, K. B., et al. 2020, arXiv e-prints, arXiv:2003.00536
- Wang, D., Hogg, D. W., Foreman-Mackey, D., & Schölkopf, B. 2016, PASP, 128, 094503
- Wong, M. H., Mahaffy, P. R., Atreya, S. K., Niemann, H. B., & Owen, T. C. 2004, Icarus, 171, 153
- Yan, F., Casasayas-Barris, N., Molaverdikhani, K., et al. 2019, A&A, 632, A69
- Yan, F., Fosbury, R. A. E., Petr-Gotzens, M. G., Zhao, G., & Pallé, E. 2015, A&A, 574, A94
- Yan, F., Fosbury, R. A. E., Petr-Gotzens, M. G., et al. 2015, International Journal of Astrobiology, 14, 255
- Yan, F. & Henning, T. 2018, Nature Astronomy, 2, 714
- Yan, F., Pallé, E., Fosbury, R. A. E., Petr-Gotzens, M. G., & Henning, T. 2017, A&A, 603, A73
- Zhang, X. 2020, Research in Astronomy and Astrophysics, 20, 099
- Zhou, Y., Apai, D., Lew, B. W. P., & Schneider, G. 2017, AJ, 153, 243

Appendix A: HST data reduction pipeline description

In the following, the two data reduction pipelines used in this work are described in more details.

Appendix A.1: Nominal pipeline

We started our data reduction with the *ima* files, which were produced by the CALWFC3 data reduction pipeline. The *ima* files contain all calibrated non-destructive reads. Before extracting the light curves, we first measure the sub-pixel-level telescope pointing drifts using the cross-correlation method and correct the drift-induced wavelength calibration error by aligning images in the *x*-direction (dispersion direction) using linear interpolation shift. We then followed the standard procedures (Deming et al. 2013) to extract light curves from the *ima* files. First, differential images, which represent the spectrum collected in each non-destructive read, were obtained by subtracting each *ima* frame from its previous read. Second, we identified and corrected bad pixels and cosmic rays. We first marked pixels with data quality flags of 4, 16, 32, 256 as bad pixels. We then searched for spurious pixels caused by cosmic ray hits by comparing the differential images with their median-filtered images and selected the 5σ outliers as cosmic ray pixels. Pixels identified as either bad or cosmic rays were replaced by linear interpolations of their neighboring pixels. Third, we subtracted the sky background from each differential image. The sky background was estimated by taking the median values of pixels that were neither illuminated by any astrophysical sources or bad pixels. To select the background region, we manually constructed pixel masks to exclude all visible spectral traces. Besides, we applied 5σ , 10-iteration sigma-clipping on the unmasked images to remove remaining bright pixels from background estimation. Finally, we measured the raw light curve of each column by taking a $R = 45$ pixels aperture photometry. We integrated spectroscopic light curves using a 5-pixel wide bin. The raw light curves are presented in Figure A.1.

The raw light curves demonstrate systematic trends that are typical to WFC3/IR observations (the “ramp effect”). Zhou et al. (2017) introduced a physically-motivated model for this effect (RECTE) by assuming that the rise of the light curve at the beginning of each orbit is introduced by stimuli gradually filling charge traps that are caused by detector defects. In the RECTE model, there are two populations of charge traps differing in their trapping efficiencies and sustaining lifetime. We corrected the systematics and fit the transit profile simultaneously. We used RECTE to model the systematics. For the transit profile, we adopted the *batman* (Kreidberg 2015) code and assumed the linear limb-darkening formula. The parameters related to the properties of the charge trap, including the numbers, trapping efficiencies, and trapping lifetimes were pre-determined. There were four free parameters in the RECTE model. They were the initially trapped charges and the amounts of trapped charges added during earth occultations for both trap populations. We also included linear trends (two free parameters) for light curves in both forward and backward scanning directions as part of the systematic model. We noted that the light curves demonstrated correlated changes with the telescope pointing variations in the *y*-direction (cross-dispersion direction), which could be adequately modeled by a linear function of Δy . We added this Δy linear term as part of the systematics model as well.

We first conducted the joint transit+systematics fit on the 1.10 to 1.70 μm broadband light curve. In addition to the param-

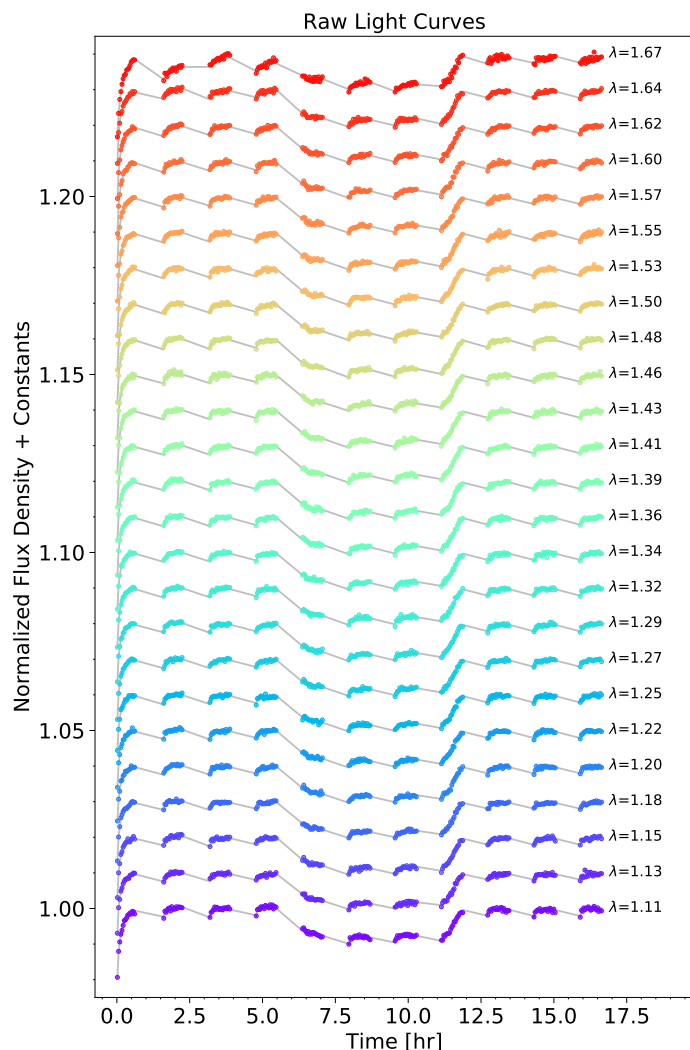


Fig. A.1. The raw light curves extracted from HST/WFC3 observations of WASP-117b. Each light curve is constructed by the integration of a 5-pixel-wide wavelength bin. Colors of the light curve represent their central wavelengths (using a rainbow color scheme, from red for longest wavelength (1.67 μm) to blue for the shortest (1.11 μm)). Light curve systematics are clearly visible, particularly at the first orbit of the observations. The gray curves show the best-fitting RECTE+transit profile models.

eters for the systematics model described above, parameters of the transit mid-time, the transit depth, and the limb-darkening coefficient were optimized using the *emcee* code (Foreman-Mackey et al. 2013). The other planetary-system related parameters, including the orbital period, system semi-major axis, eccentricity, inclination, and the longitude of periastron, were fixed using values from the literature (Lendl et al. 2014; Mallonn et al. 2019), which were already good enough for the fit. We then conducted the fit to spectroscopic light curves using the same method except fixing the transit mid-time using the best-fitting value from the broadband fit. The corrected light curves and their best-fitting transit profile models are presented in Figure A.2.

Appendix A.2: CASCADE

In addition to the nominal pipeline we also used the Calibration of trAnsit Spectroscopy using CAusal Data (CASCADE¹²) data

¹² <https://jbouwman.gitlab.io/CASCADE/>

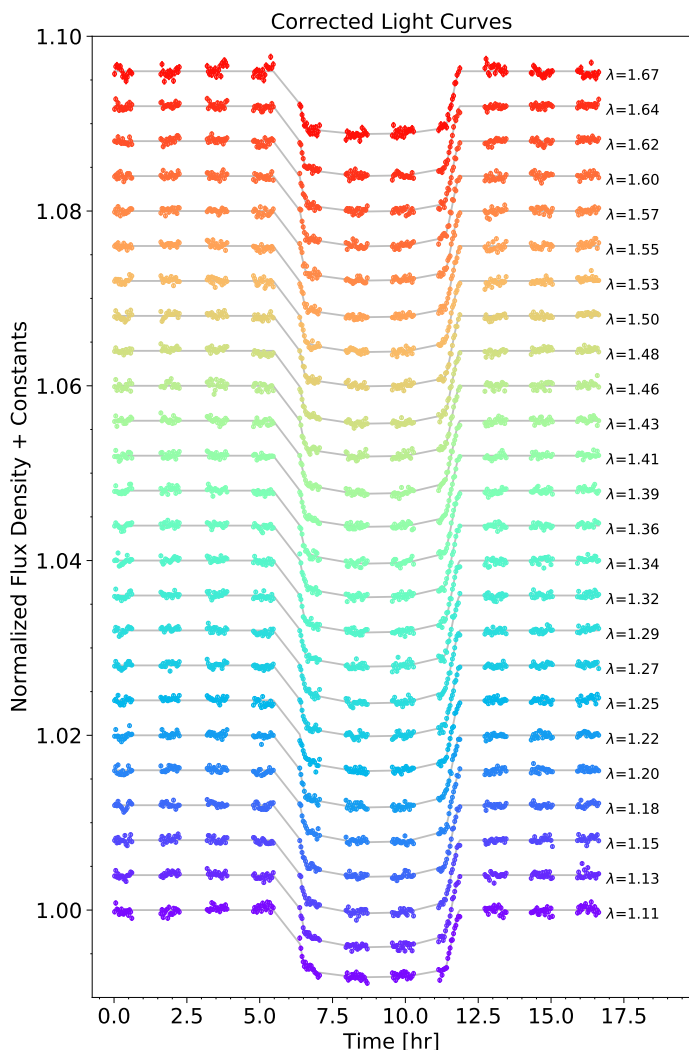


Fig. A.2. Systematics-corrected light curves of WASP-117b. Compared to the ones shown in Figure A.1, the systematics are divided-out of the light curves. The light curves are color-coded identically to Figure A.1. The gray curves represent the best-fitting transit profile models.

reduction package developed with the *Exoplanet Atmosphere New Emission Transmission Spectra Analysis* (ExoPLANETS-A¹³) Horizon-2020 programme. The CASCADE pipeline also starts the data reduction with the *ima* intermediate data product, which were produced by the CALWFC3 data reduction pipeline. As the data was observed using the SPARS10 readout mode with NSAMP = 15, the first non-destructive readout of the 16 samples of the detector ramp stored in the *ima* data product was removed as it has a much shorter readout time than the other readouts. For the remaining readouts, we constructed pairwise differences between consecutive readouts resulting in 14 signal measurements per detector ramp.

To subtract the background signal from our target signal we used the background subtraction procedure outlined in Brammer et al. (2015). This entails fitting and subtracting “master sky” images for the zodiacal light and a 1.083 μm emission line from the Earth’s upper atmosphere appearing in exposures outside of the Earth’s shadow. For details on the exact procedure we refer to section 6 of (Brammer et al. 2015).

¹³ <https://cordis.europa.eu/project/rcn/212911/factsheet/en>

To identify and clean bad pixels we first masked all pixels with quality flag other than zero. We then employed an edge-preserving filtering technique similar to Nagao & Matsuyama (1979). We refer to this paper for details on the method. This procedure ensures that the spatial profile of the dispersed light is preserved. As directional filters we use a kernel defined by a two dimensional Gaussian kernel whose width is defined by the two standard deviations σ_x and σ_y of 0.1, respectively 3 pixels which we rotated to obtain a series of different orientations. We flag all pixels deviating more than 4 sigma from the mean determined by the filter profile. After the filtering, we have three data products: one where all bad pixels are masked; a cleaned data set where all bad pixels are replaced by a mean value determined by the optimal filter for those pixels, which we will use to determine the relative telescope movements; and a smoothed data product on which we base our spectral extraction profile.

We use the image of the target with the F126N filter taken at the start of the first orbit to determine the initial wavelength solution and position of the time-series of spectral images taken with the G141 grism. We implemented the method outlined in Pirzkal et al. (2016) to determine wavelength calibration and spectral trace from the acquisition image, using the *G141.F126N.V4.32.conf* configuration file for the correct polynomial solution. The initial wavelength and trace solution is expected to have an 0.1 pixel accuracy for the trace description and better than 0.5 pixel (~ 20 nanometers) accuracy for the overall wavelength solution. As our observations are performed using the spatial-scan mode, and thus move back and forth around the initial detector position of the target system, we determined the center-of-light position of the first signal measurement to determine the absolute offset to the initial trace position. We then employ a cross-correlation technique in Fourier space, using the *register_translation* and *warp_polar* functions in the *scikit-image* package (van der Walt et al. 2014) version 16.2, to determine the relative positional shifts ($\Delta x, \Delta y$), rotation ($\Delta \Omega$) and scale changes of all subsequent exposures. The average change per scan can be seen in Figure A.3. We use these relative movements and rotations to update our wavelength solution for the spectral images at each time step.

We then optimally extract (see Horne 1986) the 1 dimensional spectra from the spectral images using as an extraction profile for each time step the normalized filtered and smoothed spectral images. After the spectral extraction step we rebin the spectra to a uniform wavelength grid using the method outlined in Carnall (2017) to determine the corresponding flux values and error estimates, after which we create an average spectra per spectral scan. The resulting white light curve of the uncalibrated time series data can be seen in the top panel of Figure A.4.

To calibrate the extracted spectral timeseries data and to extract the transmission spectrum of WASP 117b we make use of the *half-sibling-regression* methodology developed by Schölkopf et al. (2016) using causal connections within the dataset to model both transit signal and any systematics, and which has been successfully applied to transit observations from the Kepler mission (Wang et al. 2016) and field-stabilized imaging data (Samland et al. 2020). For a detailed discussion and the mathematical proof of this method we refer to the Schölkopf et al. (2016) paper. Here we briefly discuss the main concepts and our implementation of the method for the HST spectroscopic data.

Let’s assume we have a time series of (spectral) image data $D_{i,k} \in \mathbb{R}^{M \times T}$, where M is the number of detector pixels and T the number of discrete measurement times in the time series. The main idea is that all data $D_{i,k}$ as a function of detector position x_i

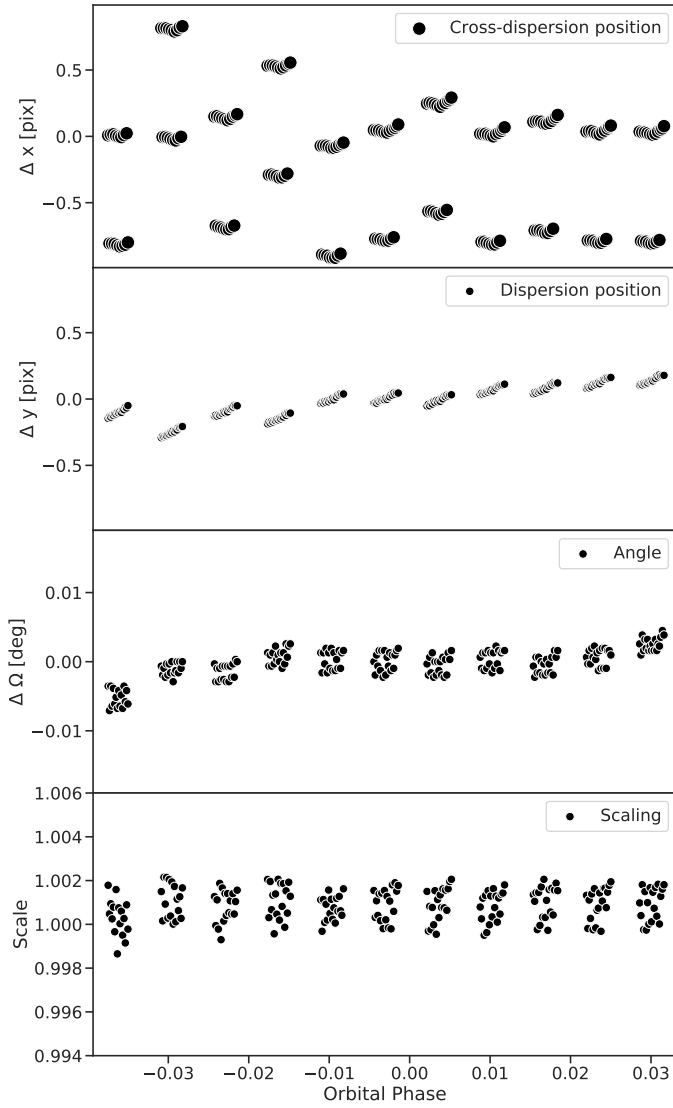


Fig. A.3. Derived pointing jitter and image distortion during the transit observation. The top panel shows the relative pointing movement in pixels for each spatial scan in the cross-dispersion direction. The second panel shows the relative pointing variations in the dispersion direction. The third panel shows the relative change in the rotation angle and the bottom panel the change in size.

at time t_k can be described by an additive noise model:

$$D(x_i, t_k | N) = S(x_i, t_k) + g(x_i, t_k | N) + \epsilon(x_i, t_k) \\ \forall i \in \{1, 2, \dots, M\} \quad \forall k \in \{1, 2, \dots, T\} \quad (\text{A.1})$$

where S (transit) signal contribution we which to measure, g denotes the functional form of the systematics affecting this measurement, and ϵ is the stochastic noise (e.g., photon noise). N here is a stand-in for all hidden parameters that may be responsible for causing the systematics. We can now split the dataset into two subsets:

$$\mathcal{P}_s = \{x_i | S(x_i, t_k) > 0\}, \quad \forall k \in \{1, 2, \dots, T\}, \quad i \in \{1, 2, \dots, N\} \\ \mathcal{P}_c = \{x_i | S(x_i, t_k) = 0\} \quad (\text{A.2})$$

where the set \mathcal{P}_s consists of all detector data which "see" the signal S and \mathcal{P}_c all other detector data. In practice one assigns those detector data to \mathcal{P}_c which is far enough removed from the

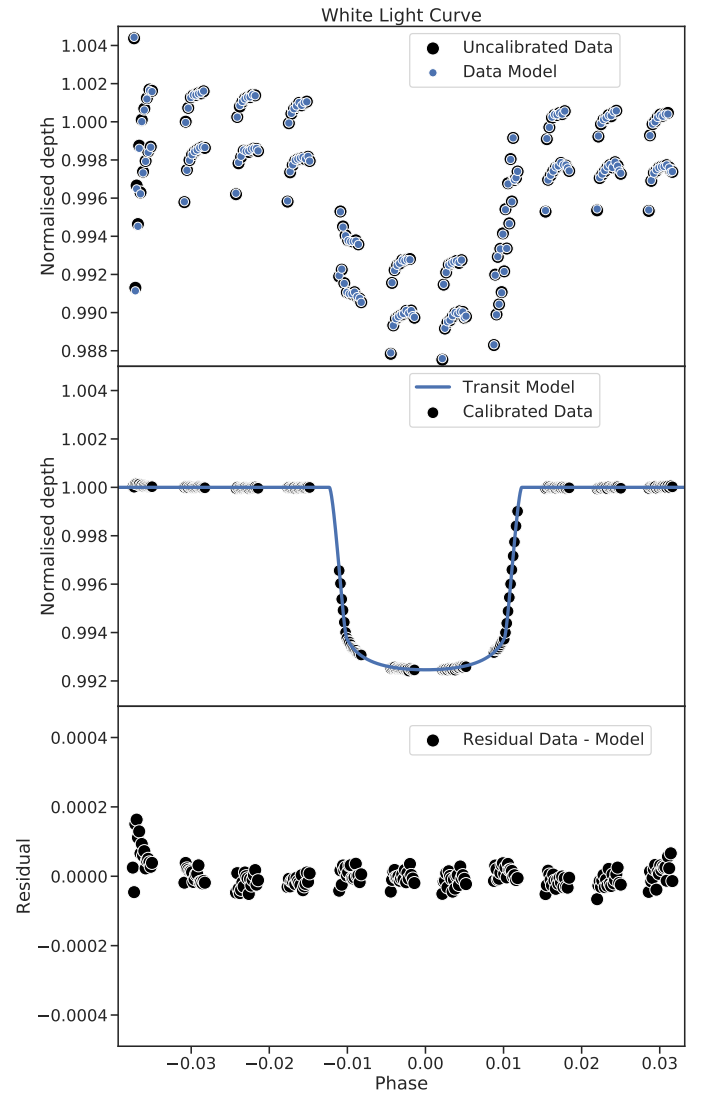


Fig. A.4. Calibration results of the spectral lightcurves with CASCADE. The top panel shows the wavelength averaged uncalibrated lightcurves for each spatial scan and the wavelength averaged fitted regression model. The bottom panel shows the fit residuals. The middle panel shows the derived calibrated lightcurve and transit model.

position of the source S on the detector such that the calibrator signal is independent of the signal of interest. This is typically a few times the full width half max of the point spread function. Further, as some of the systematics are unique to point sources (e.g. intra-pixel sensitivity variations) one limits \mathcal{P}_c to those pixels seeing other point sources in case of multi object observations (see also Wang et al. 2016). An estimate of the signal S can be made as follows:

$$\hat{S}(x_i, t_k) = D(x_i, t_k | N) - \mathbb{E}[D(x_i, t_k) | D(x_j, t_k), \Theta(t_k)], \\ \forall x_i \in \mathcal{P}_s, \quad \forall x_j \in \mathcal{P}_c, \quad \forall k \in \{1, 2, \dots, T\} \quad (\text{A.3})$$

where \mathbb{E} is the expectation value i.e. regression model for the dataset $D_{i,k}$ given the other data $D_{j,k}$ and any auxiliary data Θ_k , such as derived telescope movement as seen in Figure A.3 correlated with the systematics present in the data.

In the case of single object spectra, in contrast to the multi-object photometry like the Kepler data, rather than using the subset of data which contain the signals of other stars as regressors, we make use of the dispersed light, calibrating the observed sig-

nal at a particular wavelength with the data at other wavelengths. For the extracted HST spectra, we can rewrite Equation A.1 as:

$$D(\lambda_i, t_k | N) = S(\lambda_i, t_k) + g(\lambda_i, t_k | N) + \epsilon(\lambda_i, t_k) \\ \forall i \in \{1, 2, \dots, M\} \quad \forall k \in \{1, 2, \dots, T\} \quad (\text{A.4})$$

where the data becomes a function of the wavelength λ_i . The subsets of detector positions defining the data containing the signal of interest and the dataset used as calibrator described by Equation A.2 now becomes:

$$\mathcal{P}_s = \{\lambda_i\}, \quad i \in \{1, 2, \dots, N\} \\ \mathcal{P}_c = \left\{ \left\{ \lambda_j \mid |\lambda_1 - \lambda_j| > \Delta\lambda \right\}, \dots, \left\{ \lambda_j \mid |\lambda_N - \lambda_j| > \Delta\lambda \right\} \right\} \quad (\text{A.5})$$

where we used $\Delta\lambda = 0.07\mu\text{m}$, or about 3 resolution elements. Note that for each λ_i in \mathcal{P}_s we have a separate subset $\mathcal{P}_{c,i}$ of wavelengths which will be used to calibrate the timeseries data at λ_i . In practice a linear regression model is sufficient to simultaneously model the transit signal and systematics. As the regressors can be co-linear, we use the *ridge regression* estimator proposed by (Hoerl & Kennard 1970). The strength of the regularization is determined by Generalized cross validation (Golub et al. 1979). The regression model for the transit signal and systematics thus becomes:

$$\underset{\omega_i, \alpha_{i,j}}{\text{argmin}} \left\| \underbrace{D(\lambda_i, t_k)}_{\text{data}} - \underbrace{\left(\omega_i \hat{S}(\lambda_i, t_k) + \sum_{\lambda_j \in \mathcal{P}_{c,i}} \alpha_{i,j} D(\lambda_j, t_k) \right)}_{\text{planet + systematics model}} \right\|^2 + \underbrace{\kappa_i \left\| (\omega_i, \alpha_i) \right\|^2}_{\text{Regularization}}, \quad \forall \lambda_i \in \mathcal{P}_s. \quad (\text{A.6})$$

where \hat{S} is the model for the transit signal S and κ the regularization parameter. The parameters ω and α are the fitted parameters for the transit depth and the contributions of the timeseries data from the calibration subset, respectively. We estimate the regularization parameter for each wavelength using a generalized cross validation. Apart from the data-derived regressors, other linear terms can be added to Equation A.6 such as a constant value, time t or $\Delta X(t_k)$ the relative cross-dispersion position as shown in Figure A.3. For our final solution we added a constant term and the relative cross-dispersion position as adding these terms gave the highest signal-to-noise on the derived transit spectrum.

As we do not need to know the absolute transit depth but only the relative transit depth we use the regression estimate as defined by Equation A.6 as follows:

$$\frac{D(\lambda_i, t_k)}{\mathbb{E}[D(\lambda_i, t_k) | D(\lambda_j, t_k)] - \omega_i \hat{S}(\lambda_i, t_k)} \quad (\text{A.7})$$

to estimate the relative transit depth as a function of wavelength. The resulting combined regression model for the transit signal and systematics for the white light-curve can be seen in the top panel of Figure A.4. The residuals of the data minus the CASCADE regression model are shown in the lower panel of the same Figure. The derived calibrated normalized light curve and transit model is shown in the middle panel of Figure A.4. The final resulting transit spectrum for WASP 117b with CASCADE is shown in Figure 2.

Appendix B: Corner plots for retrieval of models used for atmosphere analysis of WASP-117b

In the following, the full corner plots as used in Sections 3.1 and 3.2 are shown for the fitted parameters and for each model used to constrain the atmospheric properties of WASP-117b during transit based on HST/WFC3 data.

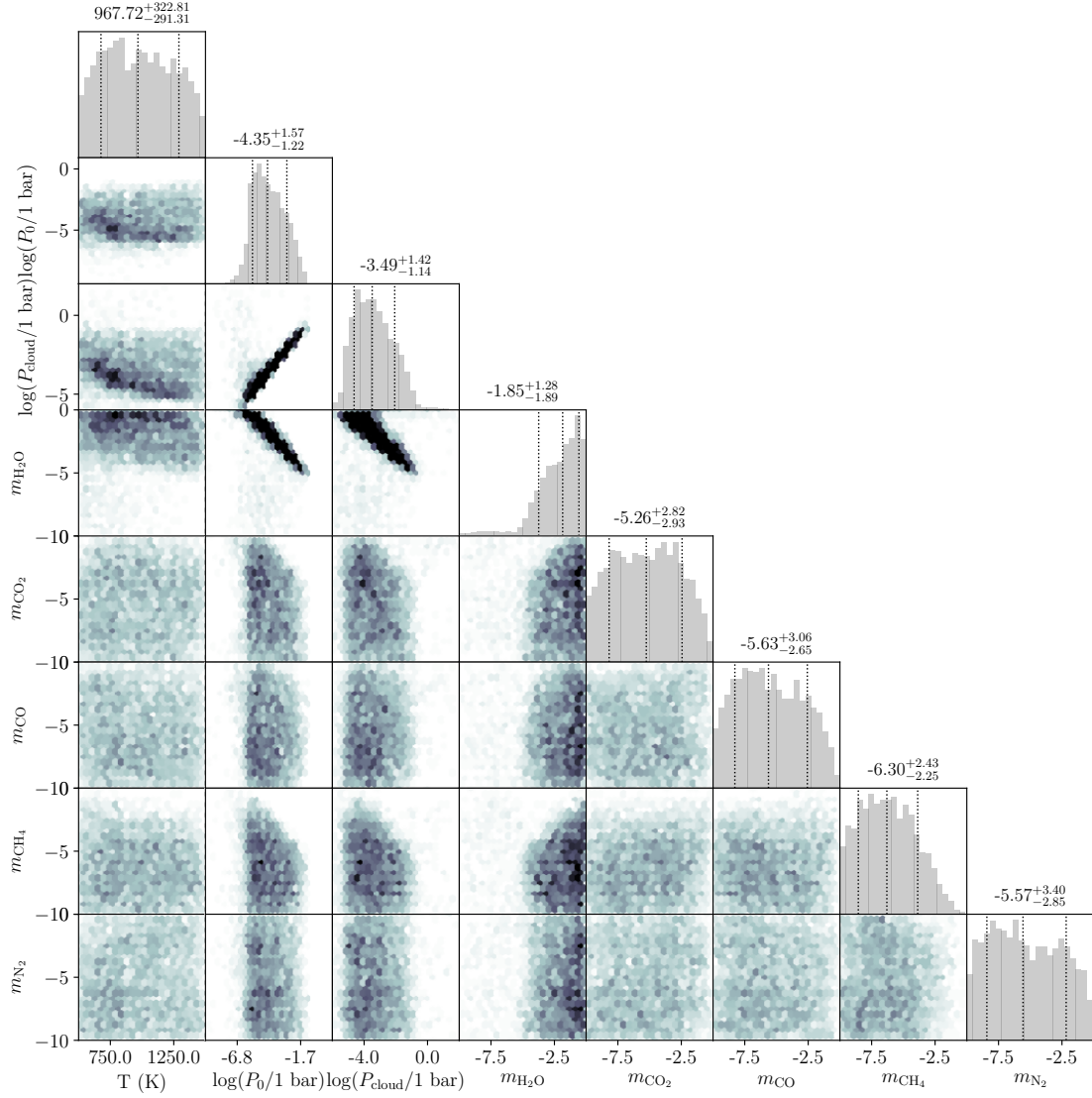
Full retrieval with H₂O - Nominal spectrum


Fig. B.1. Posterior probability distributions of the retrieval on HST/WFC3 dataset for WASP-117b, reduced with the nominal pipeline. Here, the full retrieval including H₂O was applied (see Section 3.1). Median parameter values and 68% confidence intervals for the marginalized 1D posterior probability distributions are indicated with horizontal error bars.

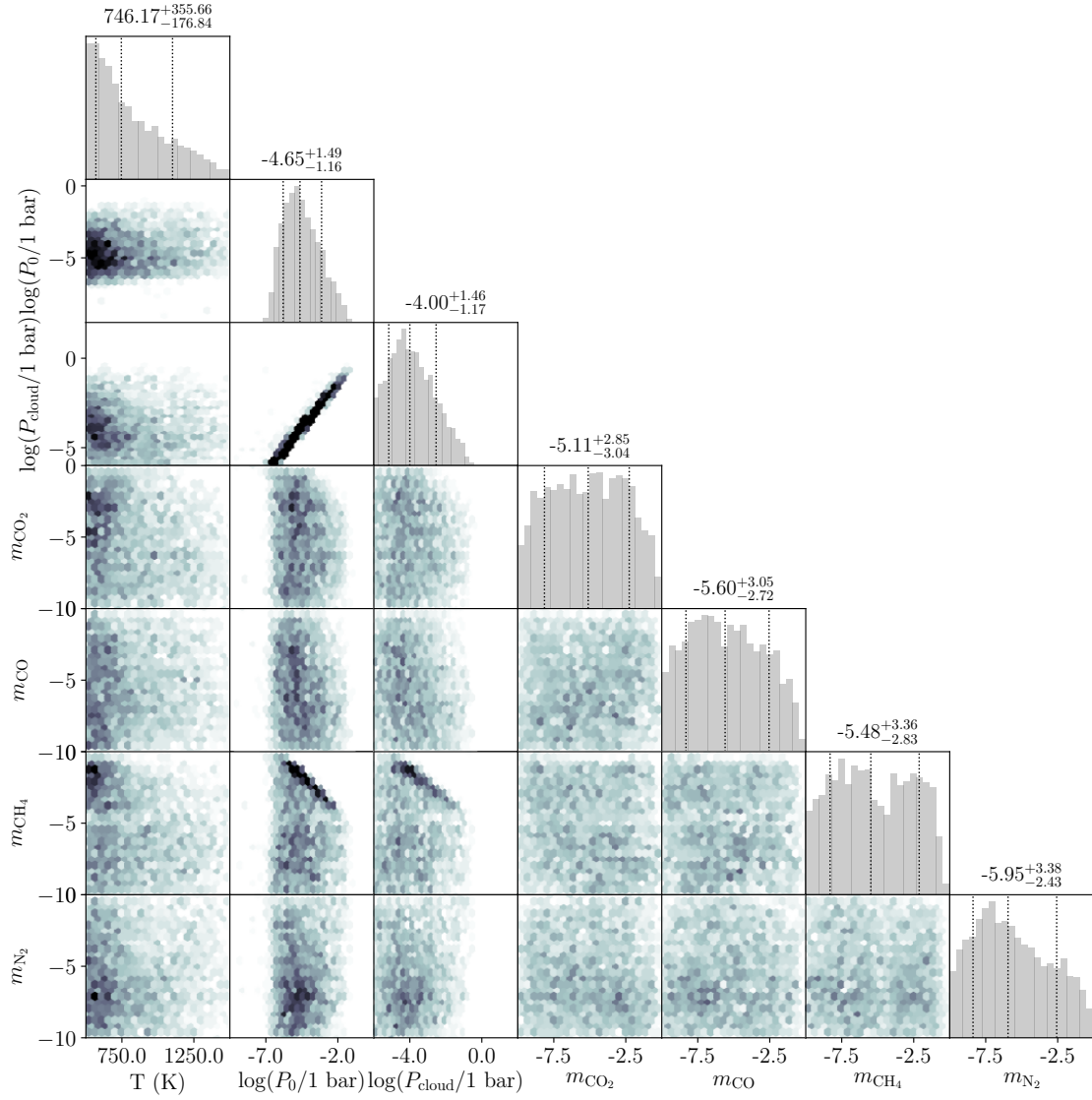
Retrieval without H₂O - Nominal spectrum

Fig. B.2. Posterior probability distributions of the retrieval on HST/WFC3 dataset for WASP-117b, reduced with the nominal pipeline. Here, the retrieval without H₂O was applied (see Section 3.1). Median parameter values and 68% confidence intervals for the marginalized 1D posterior probability distributions are indicated with horizontal error bars.

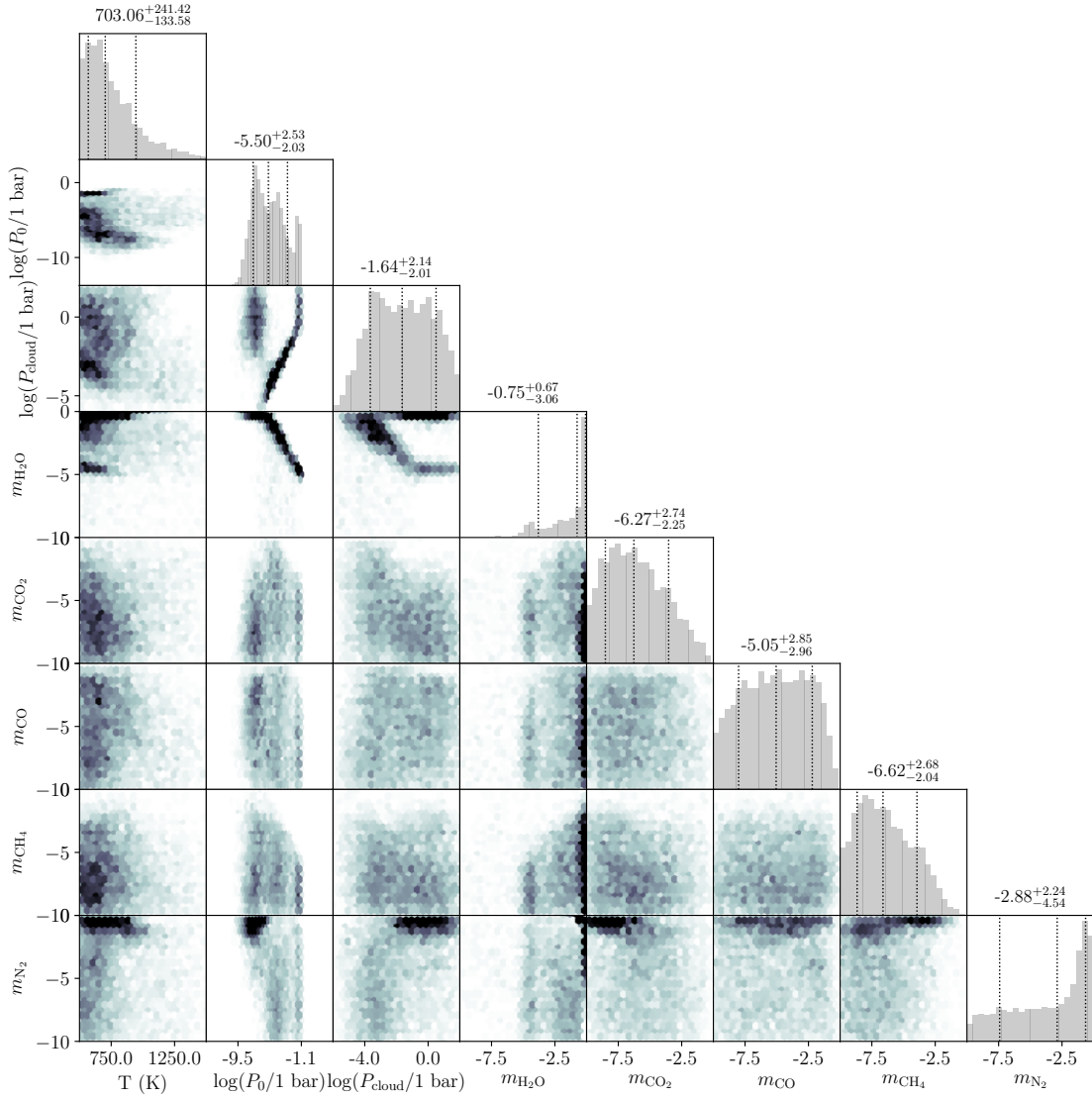
Full retrieval with H₂O - CASCADE spectrum

Fig. B.3. Posterior probability distributions of the retrieval on HST/WFC3 dataset for WASP-117b, reduced with the CASCADE pipeline. Here, the full retrieval including H₂O was applied (see Section 3.1). Median parameter values and 68% confidence intervals for the marginalized 1D posterior probability distributions are indicated with horizontal error bars.

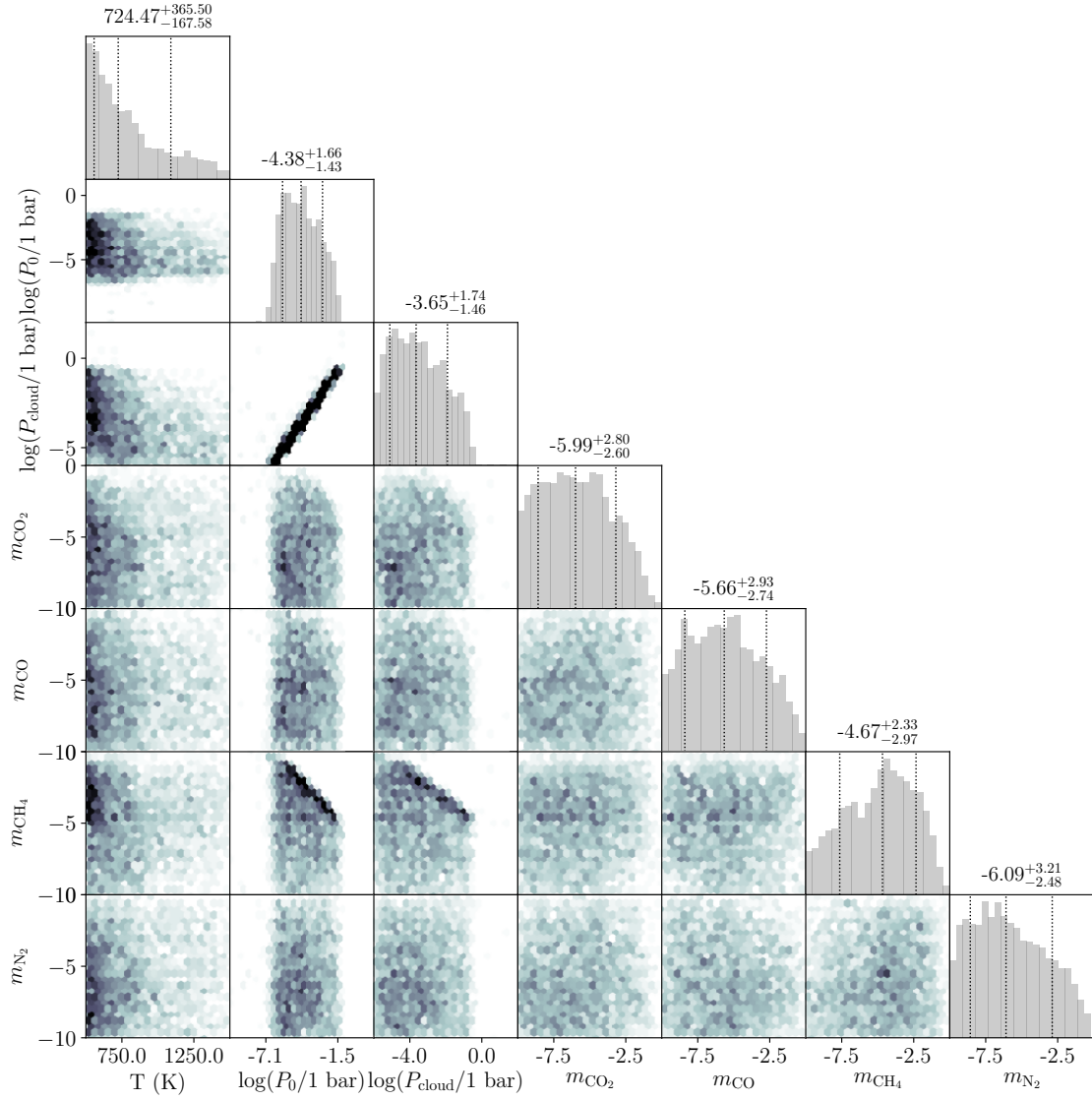
Retrieval without H₂O - CASCADE spectrum

Fig. B.4. Posterior probability distributions of the retrieval on HST/WFC3 dataset for WASP-117b, reduced with the nominal pipeline. Here, the retrieval without H₂O was applied (see Section 3.1). Median parameter values and 68% confidence intervals for the marginalized 1D posterior probability distributions are indicated with horizontal error bars.

Full retrieval with Na/K - Nominal spectrum + VLT/ESPRESSO

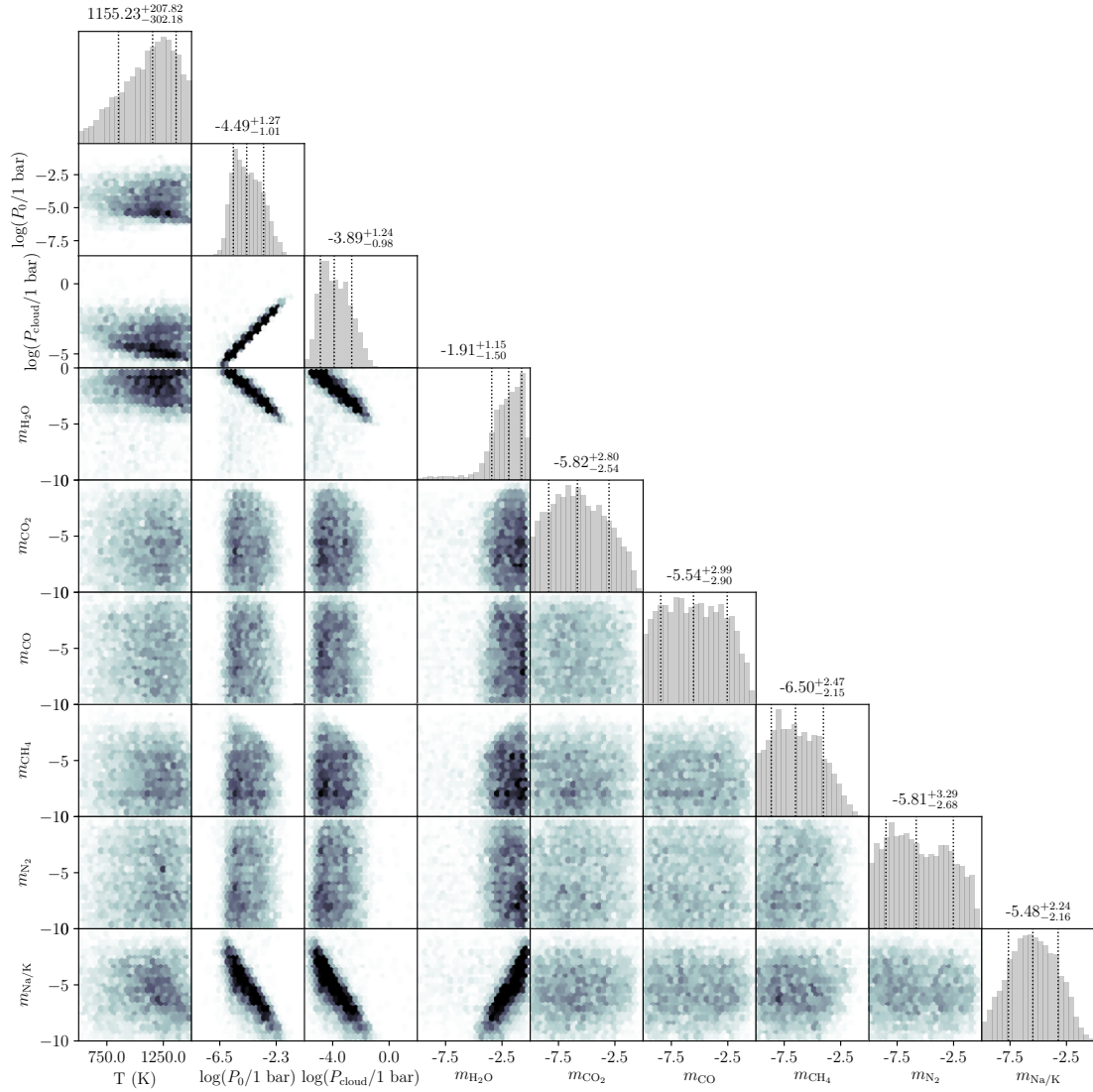


Fig. B.5. Posterior probability distributions of the joint analysis of the HST and VLT ESPRESSO dataset for WASP-117b, reduced with the nominal pipeline. Here, the full retrieval with Na and K was applied (see Section 3.1). Median parameter values and 68% confidence intervals for the marginalized 1D posterior probability distributions are indicated with horizontal error bars.

Retrieval without Na/K - Nominal spectrum + VLT/ESPRESSO

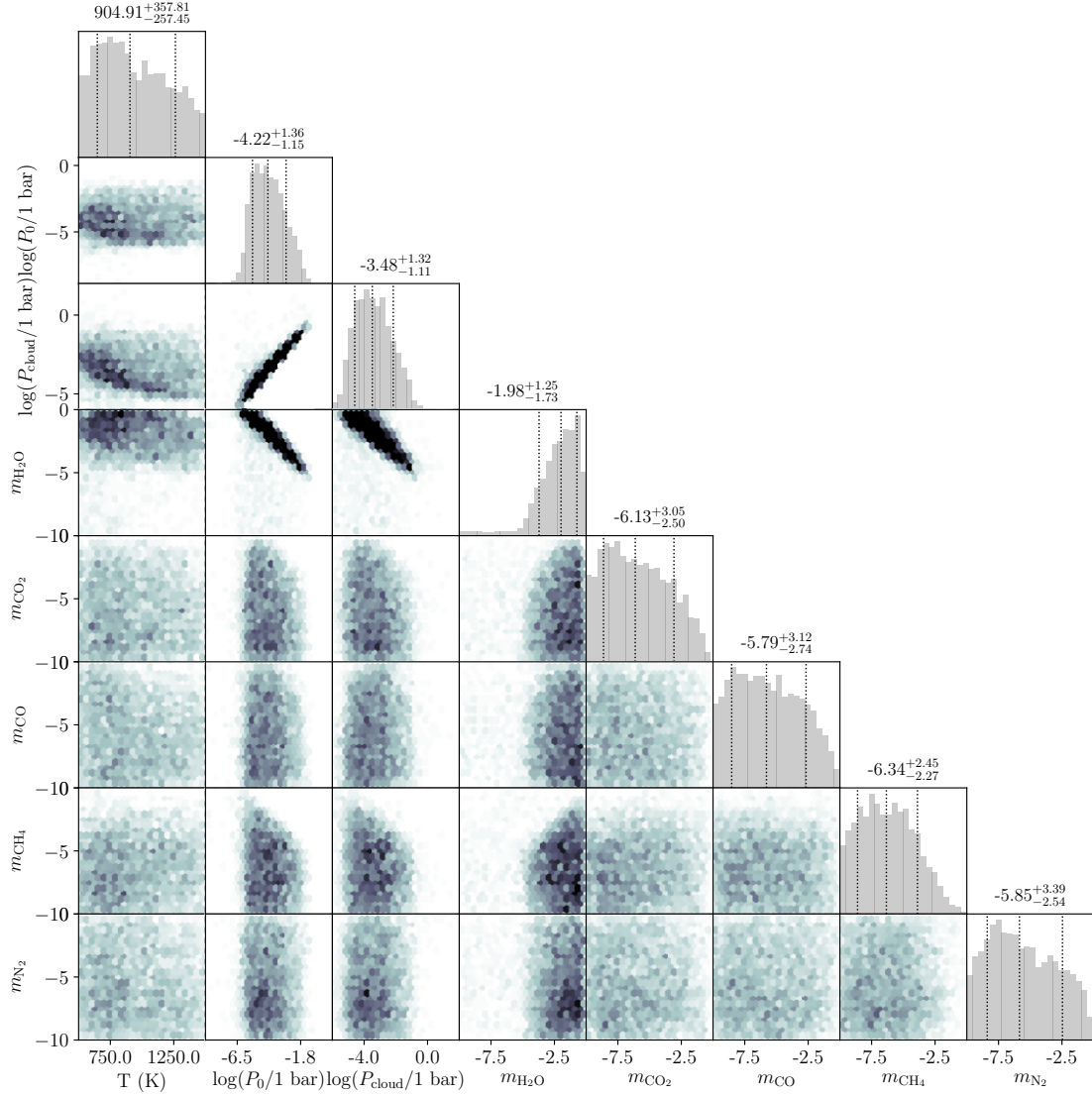


Fig. B.6. Posterior probability distributions of the joint analysis of the HST and VLT ESPRESSO dataset for WASP-117b, reduced with the nominal pipeline. Here, the retrieval without Na and K was applied (see Section 3.1). Median parameter values and 68% confidence intervals for the marginalized 1D posterior probability distributions are indicated with horizontal error bars.

Full retrieval with Na/K - CASCADE spectrum + VLT/ESPRESSO

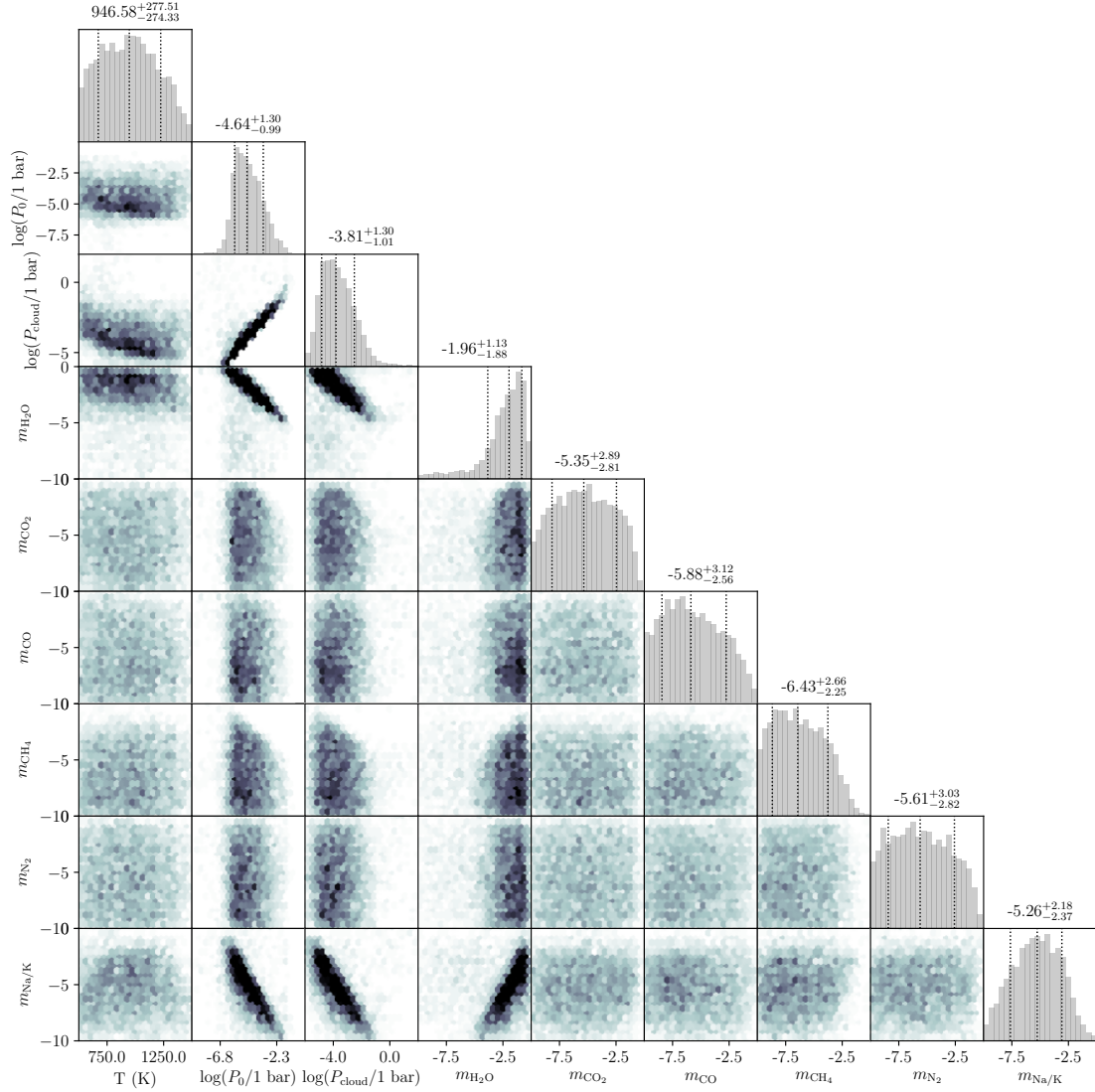


Fig. B.7. Posterior probability distributions of the joint analysis of the HST and VLT ESPRESSO dataset for WASP-117b, reduced with the CASCADE pipeline. Here, the full retrieval with Na and K was applied (see Section 3.1). Median parameter values and 68% confidence intervals for the marginalized 1D posterior probability distributions are indicated with horizontal error bars.

Retrieval without Na/K - CASCADE spectrum + VLT/ESPRESSO

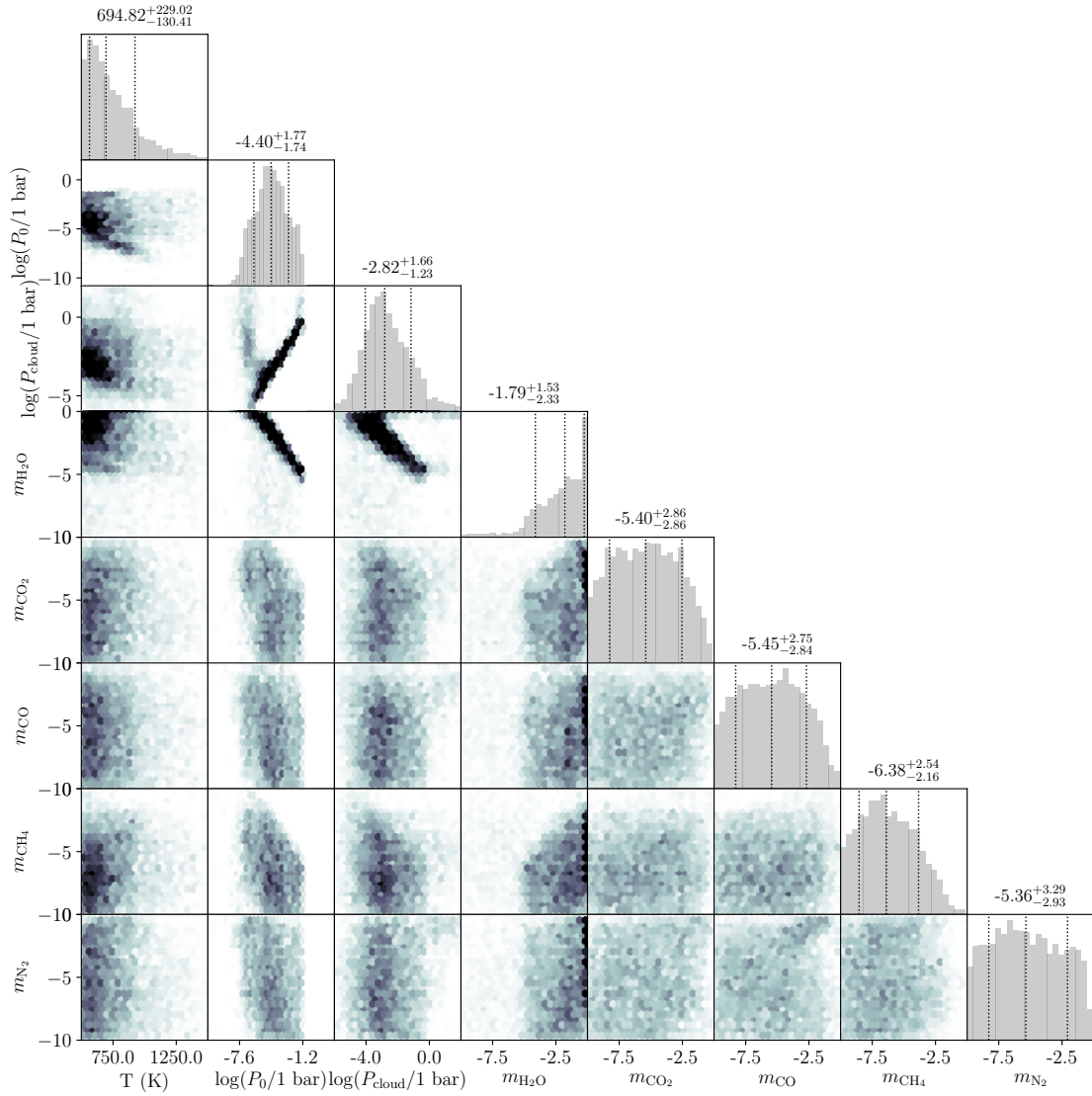


Fig. B.8. Posterior probability distributions of the joint analysis of the HST and VLT ESPRESSO dataset for WASP-117b, reduced with the CASCADE pipeline. Here, the retrieval without Na and K was applied (see Section 3.1). Median parameter values and 68% confidence intervals for the marginalized 1D posterior probability distributions are indicated with horizontal error bars.

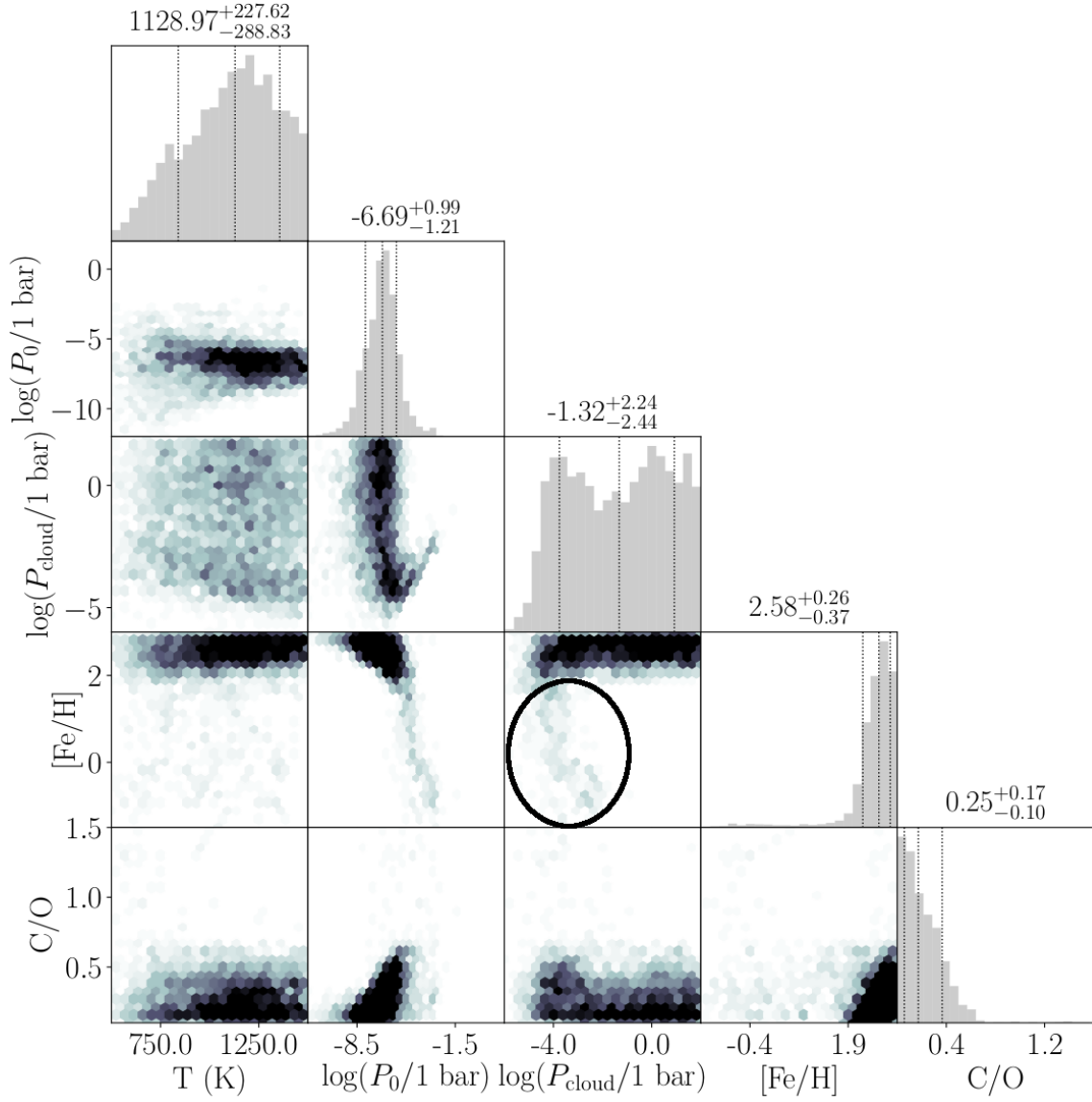
Model 1 - Nominal spectrum

Fig. B.9. Posterior probability distributions for the HST dataset, reduced with the nominal pipeline. Here, *Model 1* was applied with unconstrained $[\text{Fe}/\text{H}]$ and condensate clouds. Median parameter values and 68% confidence intervals for the marginalized 1D posterior probability distributions are indicated with horizontal error bars. The black ellipse highlights the subset of cloudy low metallicity solutions, which are explored with *Model 2* and *Model 3* further.

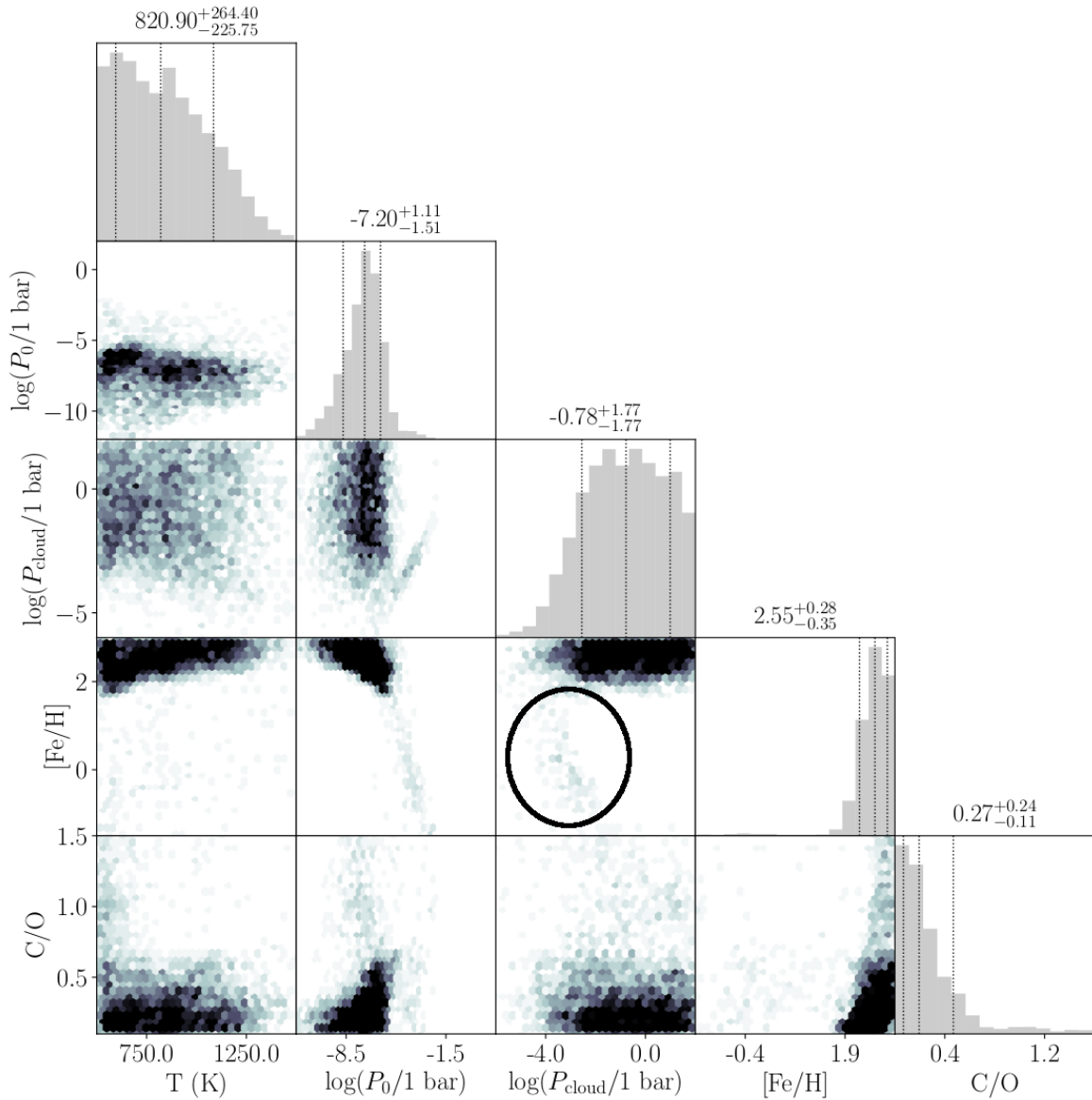
Model 1 - CASCADE spectrum

Fig. B.10. Posterior probability distributions for the HST data set, reduced with the CASCADE pipeline. Here, *Model 1* was applied with unconstrained $[\text{Fe}/\text{H}]$ and condensate clouds. Median parameter values and 68% confidence intervals for the marginalized 1D posterior probability distributions are indicated with horizontal error bars. The black ellipse highlights the subset of cloudy low metallicity solutions, which are explored with *Model 2* and *Model 3* further.

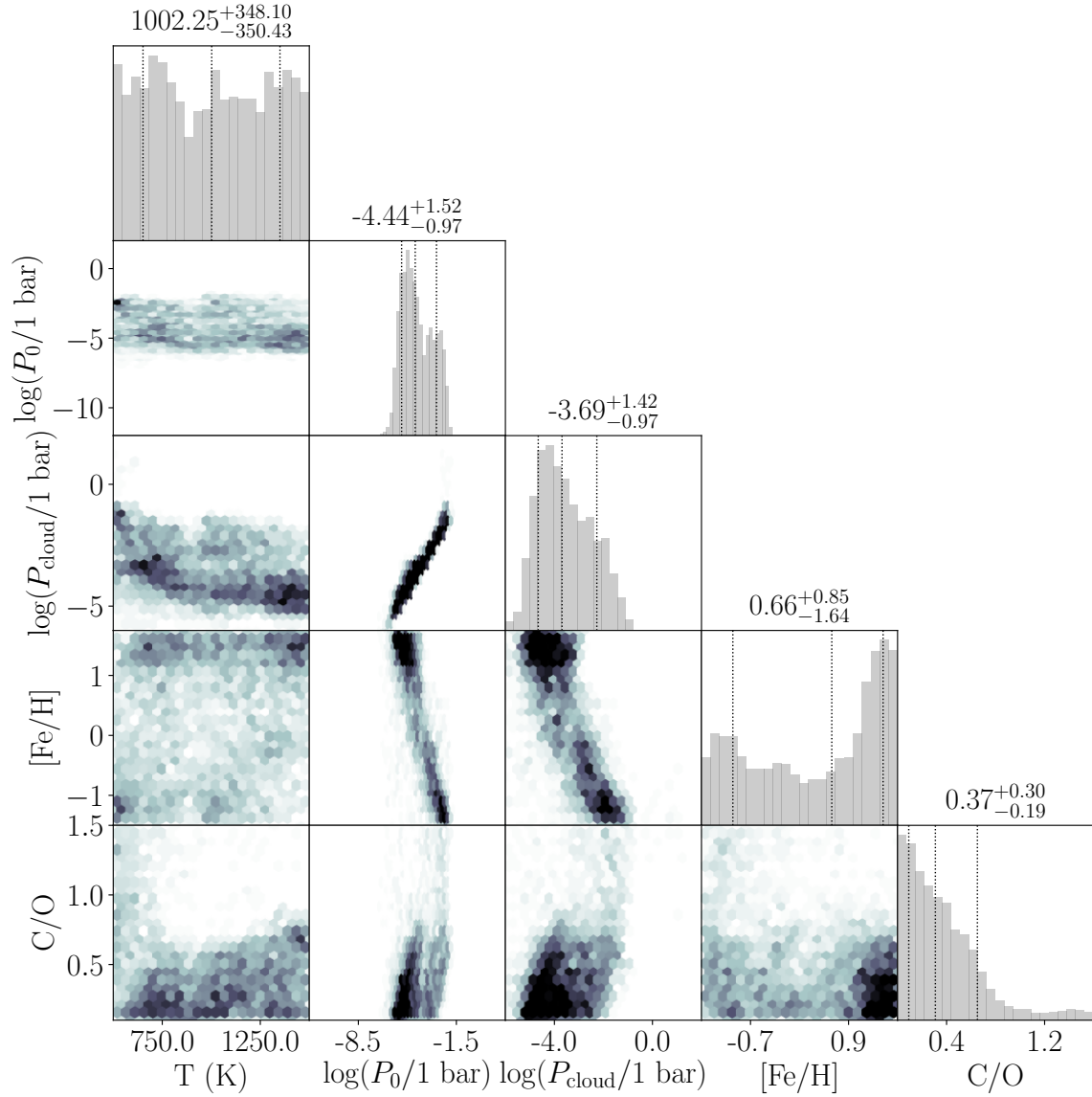
Model 2 - Nominal spectrum

Fig. B.11. Posterior probability distributions for the HST dataset, reduced with the nominal pipeline. Here, *Model 2* was applied with prior $[\text{Fe}/\text{H}] < 1.75$ and condensate clouds. Median parameter values and 68% confidence intervals for the marginalized 1D posterior probability distributions are indicated with horizontal error bars.

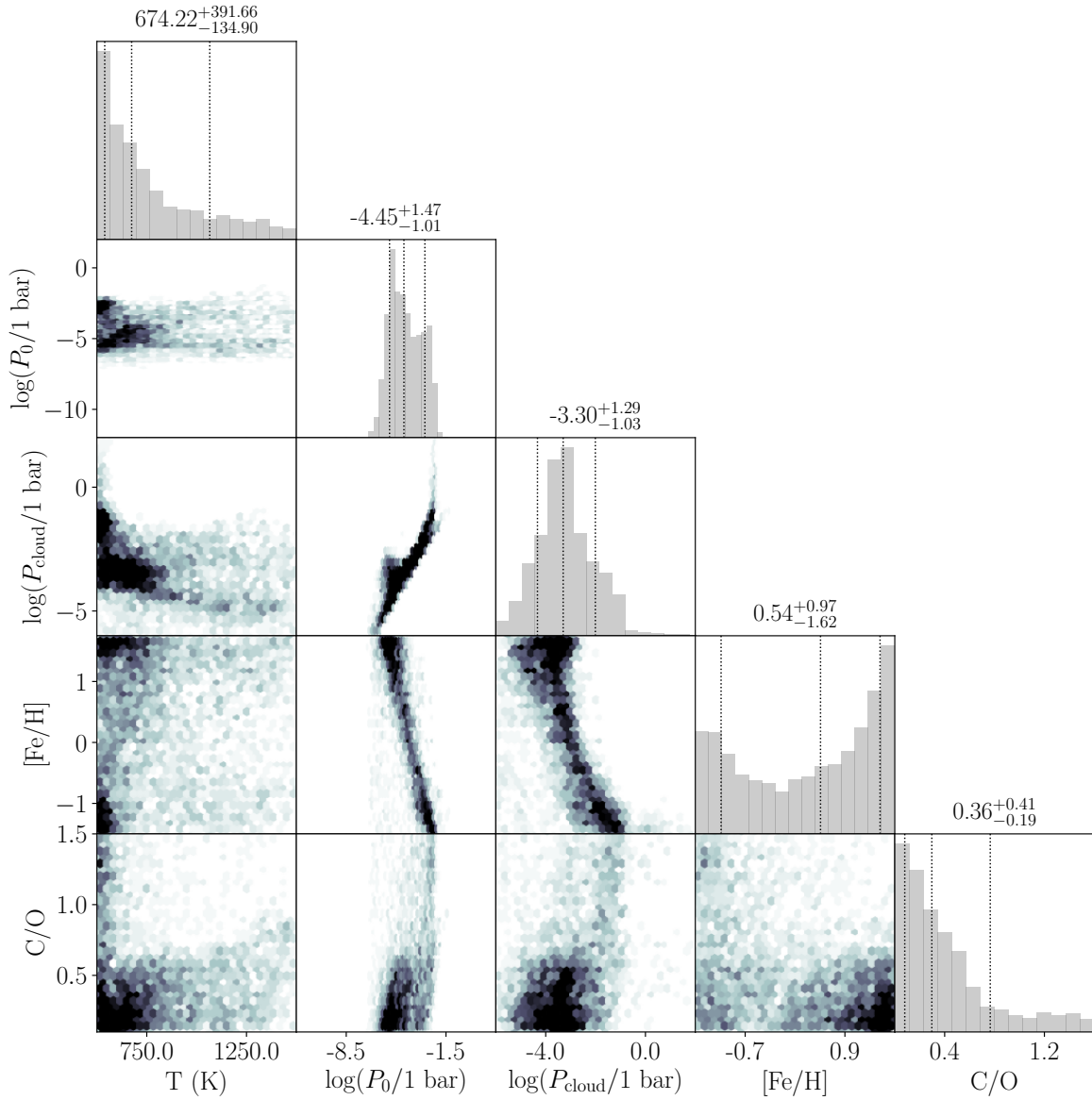
Model 2 - CASCADE spectrum

Fig. B.12. Posterior probability distributions for the HST dataset, reduced with the CASCADE pipeline. Here, *Model 2* was applied with prior $[\text{Fe}/\text{H}] < 1.75$ and condensate clouds. Median parameter values and 68% confidence intervals for the marginalized 1D posterior probability distributions are indicated with horizontal error bars.

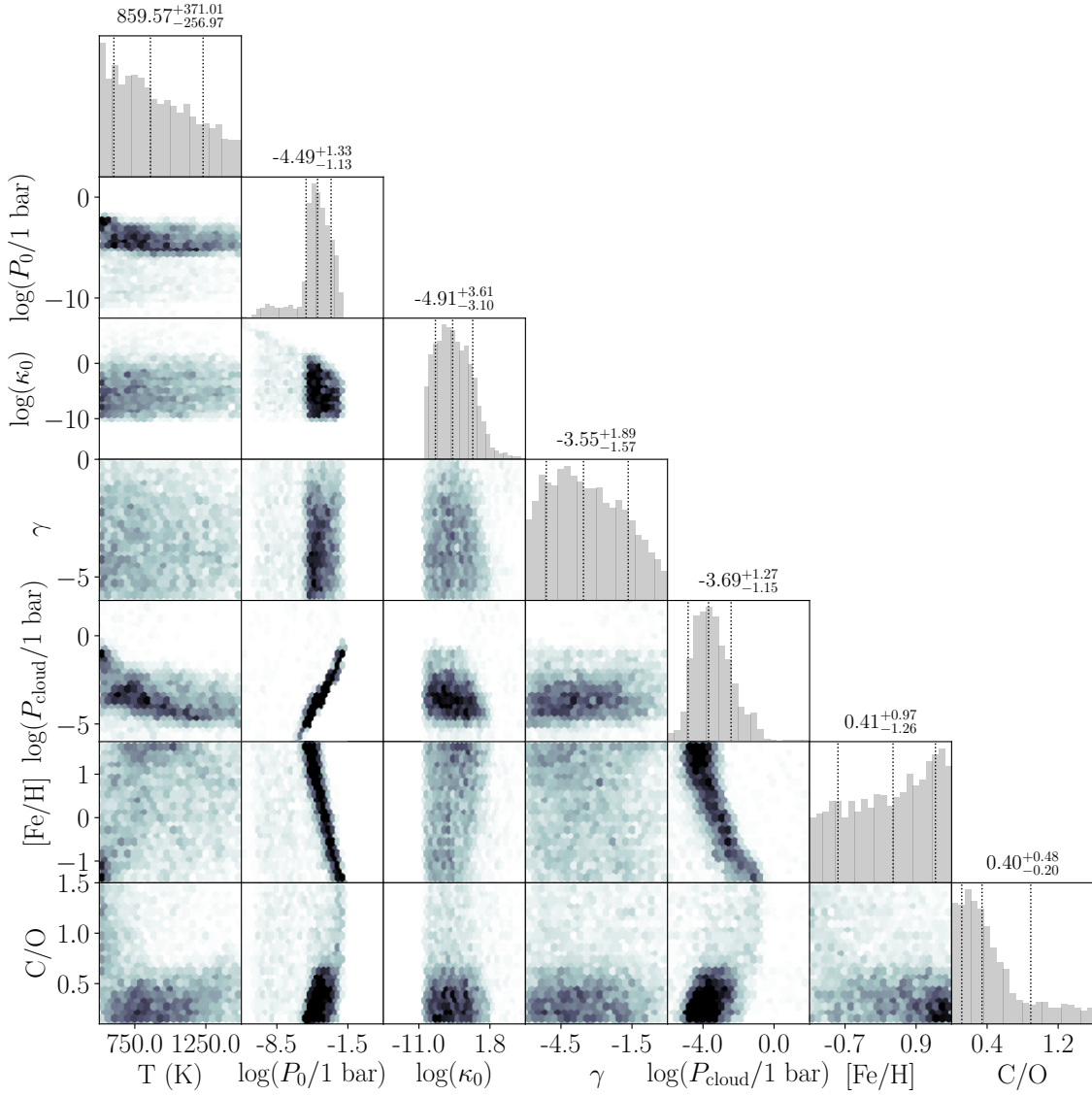
Model 3 - Nominal spectrum


Fig. B.13. Posterior probability distributions for the HST dataset, reduced with the nominal pipeline. Here, *Model 3* was applied with prior $[\text{Fe}/\text{H}] < 1.75$, condensate clouds a haze layer with a prior of $\gamma > -6$ on the scattering slope. Median parameter values and 68% confidence intervals for the marginalized 1D posterior probability distributions are indicated with horizontal error bars.

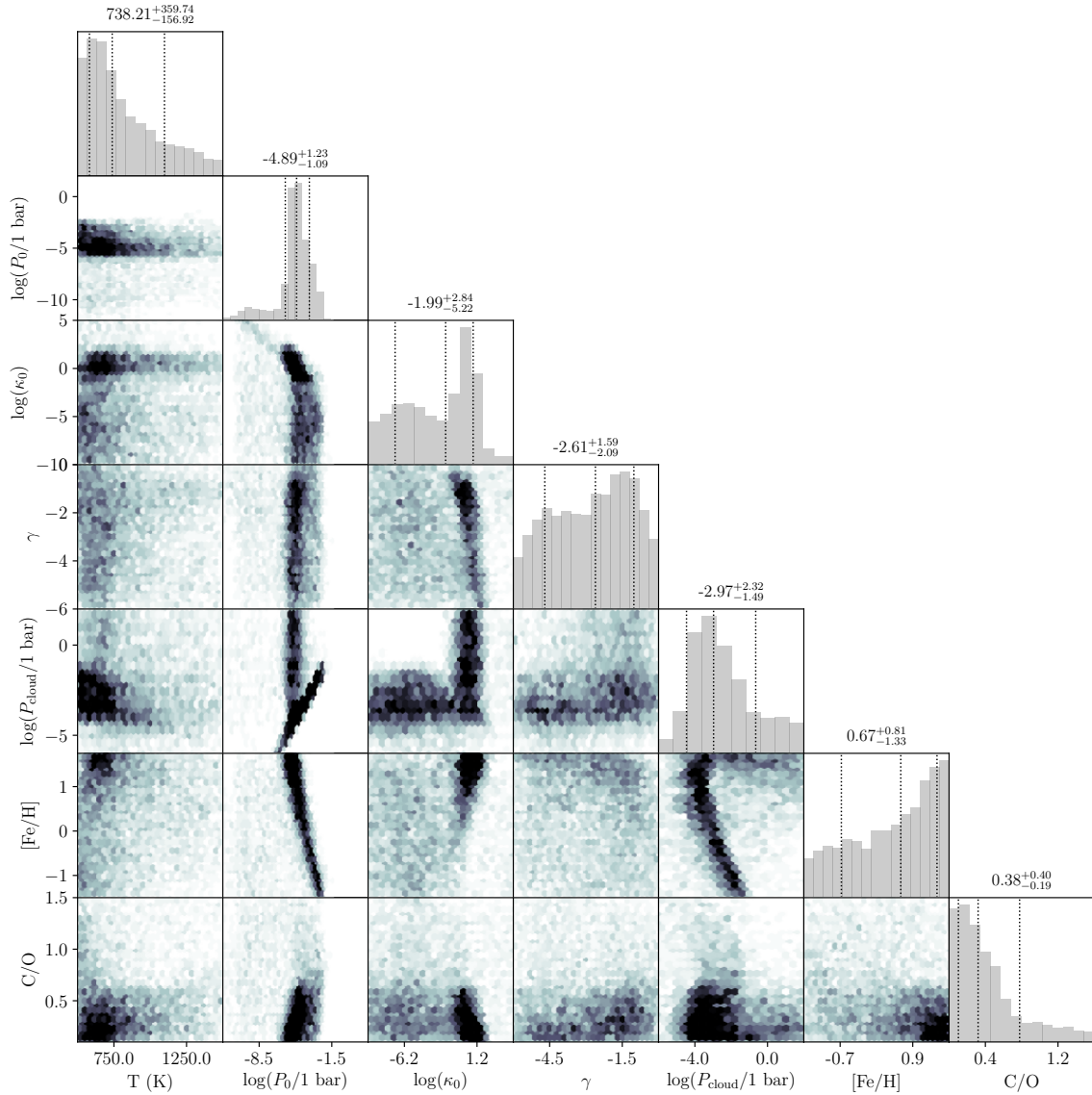
Model 3 - CASCADE spectrum

Fig. B.14. Posterior probability distributions of atmosphere properties of WASP-117b derived from WASP-117b HST observations. Raw data was reduced with the CASCADE pipeline. Here, *Model 3* was applied with prior $[\text{Fe}/\text{H}] < 1.75$, condensate clouds a haze layer with a prior of $\gamma > -6$ on the scattering slope. Median parameter values and 68% confidence intervals for the marginalized 1D posterior probability distributions are indicated with horizontal error bars.

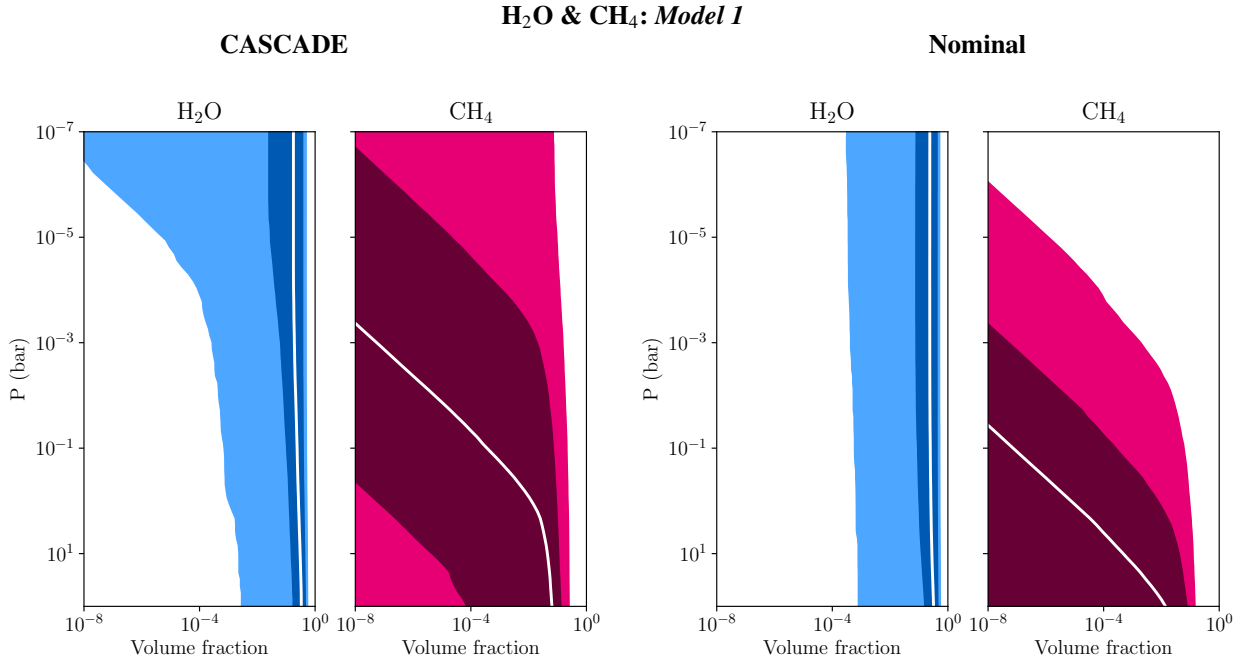


Fig. B.15. Posterior probability distributions of H₂O and CH₄ content in the atmosphere of WASP-117b based on HST observations, reduced with the CASCADE (left) and nominal pipeline (right). Here, *Model 1* was applied, with condensate clouds. Median parameter values and 99.7% (light blue and red) and 68% (dark blue and red) confidence intervals are given .

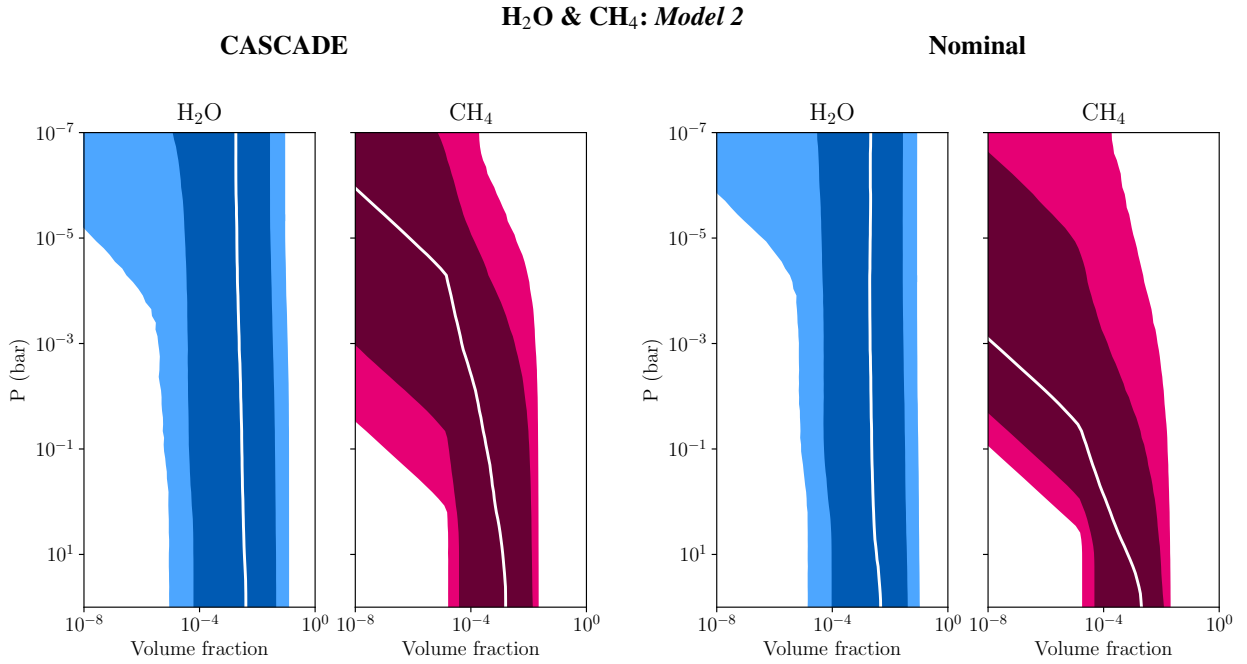


Fig. B.16. Posterior probability distributions of H₂O and CH₄ content in the atmosphere of WASP-117b based on HST observations, reduced with the CASCADE (left) and nominal pipeline (right). Here, *Model 2* was applied, with condensate clouds and $[Fe/H] < 1.75$. Median parameter values and 99.7% (light blue and red) and 68% (dark blue and red) confidence intervals are given .

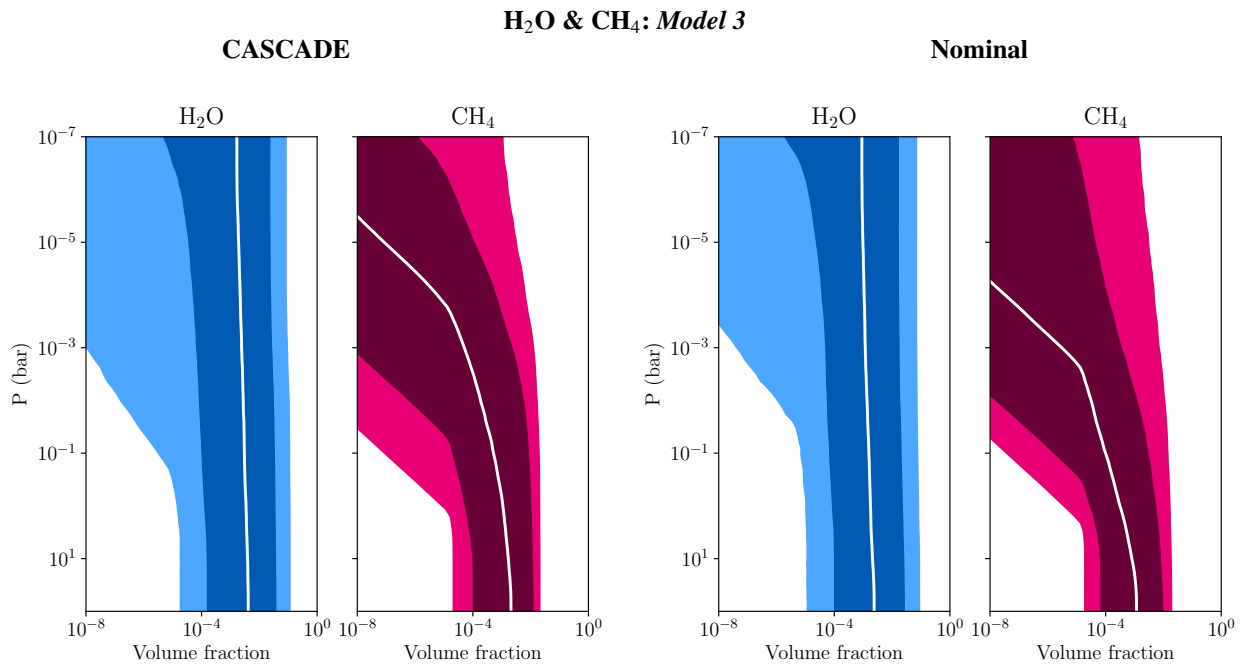


Fig. B.17. Posterior probability distributions of H₂O and CH₄ content in the atmosphere of WASP-117b based on HST observations, reduced with the CASCADE (left) and nominal pipeline (right). Here, *Model 3* was applied, with condensate clouds and $[\text{Fe}/\text{H}] < 1.75$ and haze layer with scattering slope $\gamma < 3$. Median parameter values and 99.7% (light blue and red) and 68% (dark blue and red) confidence intervals are given .

Appendix C: Effect of vertical mixing on the methane abundance

To constrain the amount of mixing needed to reproduce the retrieved methane abundance, we performed additional simulations for the cool equilibrium temperature ($T_{\text{eq}} = 700$ K) and low metallicity ($5\times$ solar) set-up, with varying eddy diffusion coefficients: $K_{zz} = 10^6, 10^8, 10^9, 10^{10}, 10^{12}$ cm²/s (see Figure C.1). Here, chemical equilibrium considerations would indicate that the atmosphere of WASP-117b is dominated by H₂O and CH₄ above ~ 100 mbar. This is still the case for eddy diffusion coefficients up to $\sim 10^6$ cm²/s. For higher values of K_{zz} , 10^8 cm²/s and above, CH₄ is getting quenched at pressures of ~ 1 bar and deeper. For these strongly mixed cases, the dominant atmospheric molecules are H₂O and CO throughout the atmosphere.

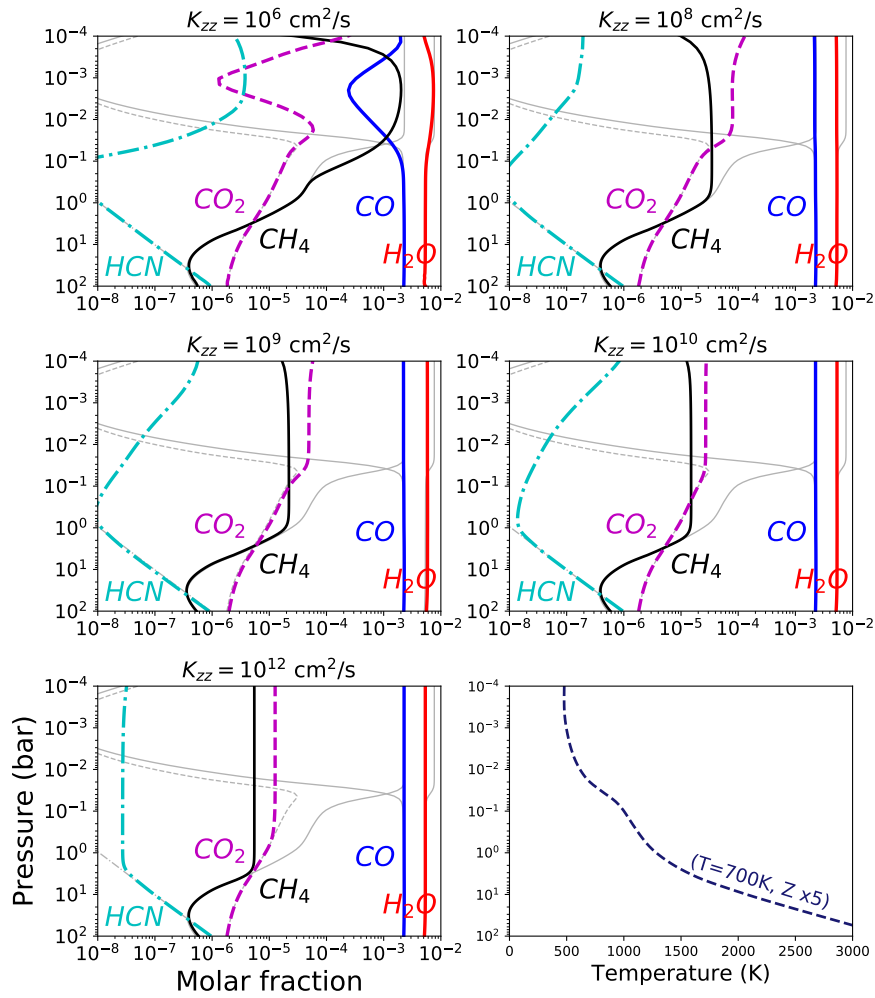


Fig. C.1. Disequilibrium abundances of the dominant molecules in the atmosphere of WASP-117b computed for different vertical eddy coefficients K_{zz} with the chemical kinetics code of Venot et al. (2012). The gray lines indicate the chemical equilibrium state. The bottom right plot shows the one-dimensional pressure-temperature profile of WASP-117b, calculated with `petitCODE` (Mollière et al. 2015, 2017). The model setup is based on the warm, slightly enriched scenario for WASP-117b ($T_{\text{eq}} = 700$ K, $Z = 5 \times$ solar, $\text{C}/\text{O} = 0.3$).